University of Alberta

Library Release Form

NAME OF AUTHOR:	Eugene Kotik
TITLE OF THESIS:	Production and Decay of Diffractive ρ^0 Mesons at HERMES
DEGREE:	Master of Science
YEAR THIS DEGREE GRANTED:	2001

Eugene Kotik

Jan 31, 2001

University of Alberta

Production and Decay of Diffractive ρ^0 Mesons at HERMES

by

Eugene Kotik

A thesis submitted to the Faculty of Graduate Studies and Research in partial fulfillment of the requirements for the degree of Master of Science

Department of Physics

Edmonton, Alberta

Spring 2001

University of Alberta

Faculty of Graduate Studies and Research

The undersigned certify that they have read, and recommend to the Faculty of Graduate Studies and Research for acceptance, a thesis entitled **Production and Decay of Diffractive ρ^0 Mesons at HERMES** submitted by **Eugene Kotik** in partial fulfillment of the requirements for the degree of Master of Science.

Prof. P. Kitching (Supervisor)

Assoc. Prof. M. de Montigny (External)

Prof. L. G. Greeniaus

Prof. H. S. Sherif

Assist. Prof. M. G. Vincter

DATE:

Abstract

The Vector Meson Dominance model describes the virtual photon γ^* at lower energies as a superposition of the lightest vector mesons. The hadronic structure of the photon allows it to interact strongly with a nuclear target N, as a result of which real vector mesons, such as the ρ^0 , may be produced. The subject of this thesis is the study of *diffractive* production of the ρ^0 meson $eN \rightarrow e'N'\rho^0$. In such a process the ρ^0 meson is regarded as the hadronic analogue of the virtual photon; therefore, spin transfer in the $\gamma^* - \rho$ system is of interest. The objective of this study is the measurement of some of Spin Density Matrix Elements (SDME) which relate the spins of the photon and the diffractively-produced ρ^0 . All the necessary information about this short-lived particle is extracted by studying angular distributions of its decay products, the π^+ and π^- mesons. The diffractive ρ^0 mesons used for this analysis were produced at the HERMES experiment in 1996 and 1997 in collisions of a 27.5 GeV positron beam with a hydrogen target. The thesis describes the theoretical tools of the study, gives an overview of the HERMES experiment, presents the analysis and compares the results for SDMEs to the those from previous experiments.

Acknowledgements

The successful completion of this thesis was only possible with the help of many people that I was fortunate to meet during the last two and a half years. I would like to express cordial gratitude to all involved.

I am immensely greatful to my supervisor, Prof. Peter Kitching, for providing me with an opportunity to complete this thesis as a part of the HERMES experiment. It has been a great pleasure to work for Prof. Kitching, who patiently guided my work through all the difficulties and stimulated my creativity and independent thinking. I owe many thanks to a former student of Prof. Kitching, Kalen Martens, who set up many pieces of the analysis software and offered advice whenever I had questions. I am very thankful to Dr. Peter Green for setting up the crucial simulation software and for sharing his vast software expertise with me, to Prof. Manuella Vincter for her advice on the data analysis and organisational matters, and to Prof. Gordon Greeniaus for his very educational guidance through the corrections to my thesis in Prof. Kitching's absence.

I thoroughly appreciate the scientific discussions with many members of the HERMES collaboration in Hamburg and with fellow graduate students at the University of Alberta, — I thank very much all of you, as much of your advice was used in writing this thesis!

Finally, I would like to thank all my relatives and friends, and especially my parents, for their stoical support and understanding.

Table of Contents

List of Tables

List of Figures

Chapter 1

Introduction

From a brief introduction into the world of elementary particles to a qualitative description of the ρ^0 production mechanism, this chapter familiarises the reader with the subject of this thesis.

The data required for this work was collected in 1996 and 1997 at the HERMES experiment, which uses collisions of a 27.5 GeV positron beam with a fixed gaseous target. The experiment is located in the East Hall of the HERA storage ring complex at DESY in Hamburg, Germany. The spectrometer is a forward angle instrument of conventional design. It has relatively large acceptance and is capable of detecting multiple particle final states. Energy and momentum of outgoing particles are determined with good precision and particle identification over positrons and hadrons is done over a large energy range.

1.1 Elementary Particles and Fundamental Interactions

In their attempts to understand the finest structure of matter, physicists are facing a challenging puzzle: though the simplest objects in the Universe, elementary particles behave according to very complicated laws that are not yet completely understood. It is now known, however, that all forces between objects arise via the four *fundamental interactions*: gravitational, electromagnetic, strong, and weak. Among these four, only the gravitational and electromagnetic forces are responsible for interactions in the everyday world, while the remaining two manifest themselves only on a scale no greater than the radius of the atomic nucleus.

On the most fundamental level, every interaction is characterised by a mediating particle. There are six such particles, altogether called the *interaction mediators*. In addition, every interaction is characterised by a certain physical quantity unique to this interaction. Accordingly, the gravitational interactions occur between all particles that possess *mass* and are mediated by the *graviton*. Similarly, the electromagnetic interactions occur between particles that have an *electric charge* via the *photon*, the strong interactions — between particles that have *colour charge* via the *gluon*, and the weak interactions — between particles that have *flavour* via the Z^0, W^+, and W^- particles. The graviton, the gluon, and the photon are massless, while the Z^0, W^+, and W^- particles are much heavier than most other elementary particles.

Every elementary particle is characterised by its *spin*, which is the magnitude of its *intrinsic* angular momentum. All interaction mediators possess a spin that is an integer multiple of $\hbar$: the graviton has spin $2\hbar$, the photon, the gluon, and the Z^0, $W^\pm$ particles have spin $1\hbar$. Particles with a value of spin equal to an integer multiple of $\hbar$ obey Bose-Einstein statistics and are therefore called *bosons*.

With the interaction mediators already introduced, the remaining particles are classified into two large groups, *leptons* and *quarks*. Unlike the interaction mediators, both leptons and quarks have spin $\frac{1}{2}\hbar$. Such particles, with spin equal to an odd half-integer multiple of $\hbar$, obey Fermi-Dirac statistics and are therefore called *fermions*.

There are six leptons grouped into three *generations* (Table 1.1). Each generation consists of one massive particle with a charge $-1e$ and one massless (or very small mass) particle with a charge 0, where $e = 1.602189 \times 10^{-19}$ Coulomb is the elementary charge, i.e. the charge of a hydrogen nucleus. It is customary to omit e in subatomic physics; the charge of the hydrogen nucleus is therefore stated as +1 and that of the familiar electron is stated as –1. Mass increases and the lifetime decreases from the electron to the tau, the electron being the only massive lepton with infinite lifetime. Every lepton possesses an *antiparticle*, which, in the case of the charged lepton, has a charge +1. The antiparticle of the electron (e^-) is known as the positron (e^+).

Similarly, quarks appear in 6 *flavours* (u, d, s, c, b, t) grouped into three generations. Each generation consists of two quarks, one with a charge $+\frac{2}{3}$ and the other one with a charge $-\frac{1}{3}$ (Table 1.1). The masses of quarks of different flavours differ.

Gener.	**Quark**	**Symbol**	**Charge**	**Lepton**	**Symbol**	**Charge**
1st	down	d	$-\frac{1}{3}$	electron	e^-	–1
	up	u	$+\frac{2}{3}$	el. neutrino	ν_e	0
2nd	strange	s	$-\frac{1}{3}$	muon	μ^-	–1
	charm	c	$+\frac{2}{3}$	muon neutrino	ν_μ	0
3rd	bottom	b	$-\frac{1}{3}$	tau	τ^-	–1
	top	t	$+\frac{2}{3}$	tau neutrino	ν_τ	0

Table 1.1: Quarks and leptons in nature. Masses of quarks and charged leptons increase with generation number.

While instrumental in determining the macroscopic structure of the Universe, the gravitational force is extremely weak and therefore does not manifest itself measurably at energies available with modern accelerators. The following will describe the remaining 3 interactions in greater detail.

The weak interaction is the weakest force among the three. It is responsible for the instability of the muon and the tau particle. The muon and tau decays are mediated by the $W^{\pm}$ particles. The weak interaction mediates all processes involving neutrinos, such as the proton-neutrino scattering, where the $W^{\pm}$ or Z^0 particles are exchanged. The weak force also mediates processes that involve flavour transitions; for example, a strange quark may convert into an up quark via the W^-. A β-decay of radioactive nuclei is another example of a weak process, where neutrons are transformed into protons, or *vice versa*. The currently accepted theory of the weak interactions is due to Glashow, Salam, and Weinberg, and is known for this reason as the *GWS theory* [1–3].

The electromagnetic interaction involves particles that possess charge: quarks and charged leptons. Charged leptons interact with most particles via the electromagnetic force, since it is significantly stronger than the weak force. The theory of electromagnetic interactions is known as *Quantum Electrodynamics* (QED). QED and the GWS theory are combined into the *electroweak theory*.

The quarks possess colour charge; the leptons do not. Therefore only the former exhibit strong interactions. A quark of any flavour can have one out of the three possible colour charges denoted as "red", "green" and "blue". Such a choice of terminology is useful, since a red, a green and a blue particle together form a "white" object, i.e. one with no net colour. Such a compound object is called *baryon* (qqq). The lightest baryons are the proton (uud) and the neutron(udd); the two form atomic nuclei. The proton is the only stable baryon.

To every quark, there corresponds its antiparticle, the antiquark, which possesses the same mass, but the opposite charge. Antiquarks are characterised by antiflavour and anticolour. For example, a red strange quark corresponds to an antired antistrange antiquark; this antiquark would have a charge of $+\frac{1}{3}$. Three antiquarks, each with a different anticolour, form a compound particle called *antibaryon* ($\bar{q}\bar{q}\bar{q}$). A quark with a certain colour and an antiquark with a corresponding anticolour also form a colourless object. Such a compound particle is called *meson* ($q\bar{q}$). All mesons are unstable, and their lifetimes vary.

At present, no free coloured objects have been observed. Absence of uncompensated colour dictates that quarks and antiquarks form bound states with no net colour. Such bound states are the baryons, the antibaryons and the mesons. Baryons possess half-integer spin, while mesons possess integer spin. Together, baryons, antibaryons, and mesons are termed *hadrons*. Depending on the charge of the constituent quarks and antiquarks, hadrons may have a net charge -2, -1, 0, $+1$ and $+2$. The requirement that the free objects be colourless is known as *colour confinement*. This implies that quarks are confined to hadrons.

A theory that describes the strong interactions is called Quantum Chromodynamics (QCD). QCD, QED, and the GWS theory together form the *Standard Model*, a theory that describes remarkably well the world of elementary particles at currently available energies.

1.2 Units

In subatomic physics, it is customary to use the Heaviside-Lorentz system of units. In this system, the value of the speed of light c, elementary positive charge e and the fundamental unit of angular momentum $\hbar$ are equal to 1.

Since the speed of light is now equal to unity, energy, momentum, and mass have the same units. These units are called *electron-Volts* (eV), where 1 eV $= 1.602 \times 10^{-19}$ J. The Heaviside-Lorentz system will be followed throughout this thesis. Hence, c, $\hbar$ and e will be omitted, unless their inclusion makes argumentation more illustrative.

1.3 The ρ^0 Meson

The main subject of this thesis is the physics of the ρ^0 meson. The ρ^0 meson is a spin-1 particle consisting of the lightest quark-antiquark pair. With other spin-1 mesons, it is classified as a *vector* meson, as opposed to the scalar mesons with spin 0. It is very short-lived, with a lifetime of 4×10^{-24} s. At HERMES, the ρ^0 meson is produced in collisions of the positron beam with the nuclear target. The lifetime of the particle is so short that it decays before leaving the target nucleus, making its direct detection impossible. The ρ^0 meson decays nearly 100% of time into a $\pi^+\pi^-$ pair. By measuring energy and momentum of the pion pairs, it is possible to identify those produced as a result of a ρ^0 decay and calculate several parameters for the parent particle, the ρ^0 meson.

Physics of the ρ^0 particle contains several aspects that are a result of the built-in lack of determinism in quantum mechanics. In classical physics, it is possible in principle to measure a physical quantity to any precision allowed by the apparatus. An increase in the measurement precision of one physical quantity does not limit the precision of other measurements on a *classical system*. However, a measurement, performed on a *quantum system*, affects its quantum state and thereby influences simultaneous measurements of other physical quantities. Thus, there exist natural limitations to the quantum mechanical measurement precision. A quantitative description of such limitations is called the *Heisenberg uncertainty principle*:

$$\Delta E \Delta t \geq \frac{\hbar}{2}, \quad \Delta p_i \Delta x_i \geq \frac{\hbar}{2} \quad \text{and} \quad \Delta L_i \Delta \phi_i \geq \frac{\hbar}{2}\ , \tag{1.1}$$

where ΔE is the uncertainty in energy, Δt — uncertainty in time, and Δp_i, Δx_i, ΔL_i, $\Delta \phi_i$ — uncertainties in i-components of momentum, position, angular momentum and angle of revolution, respectively.

The Heisenberg uncertainty relations underline the probabilistic nature of quantum systems: indeed, it is impossible to predict the exact value of a measurement of the above mentioned physical observables, even with a perfect apparatus. Therefore, rather than asserting a certain value of a measurement, it is only possible to state the probability of measuring such a value. Several consequences applicable to the ρ^0 physics arise from the uncertainty principle.

The uncertainty in energy allows violation of the conservation of energy for a very short time. This violation, in turn, allows creation of *virtual* particles that annihilate after a short period of time. At HERMES, a beam of positrons e^+ collides with a nuclear target. Because positrons do not carry colour charge, they do not interact by the strong force; therefore, the interaction of a positron with the nuclear target is dominated by the electromagnetic force mediated by a virtual photon γ^*. Allowed to do so by the uncertainty principle, the γ^* may fluctuate into a quark-antiquark pair, with the latter forming bound states in the lower energy regime. Thus it is useful to picture the photon at lower energies as a superposition of the lightest vector mesons. The existence of such structure is a basis for the Vector Meson Dominance Model (VMDM), described in detail in [4]. The hadronic composition of the photon allows a strong interaction to occur between the photon and the nuclear target N, with a composite electrically neutral object acting as a mediator (Fig. 1.1). The nature of this object is discussed in more detail in Chapter 2. As a result of such an interaction, it is possible for the photon to become a real vector meson V. This mechanism, where a vector meson is produced with the target remaining intact and no other particles produced, is called *diffractive* vector meson production. This terminology is chosen because the production cross-section $\frac{d\sigma}{dt}$ depends exponentially on

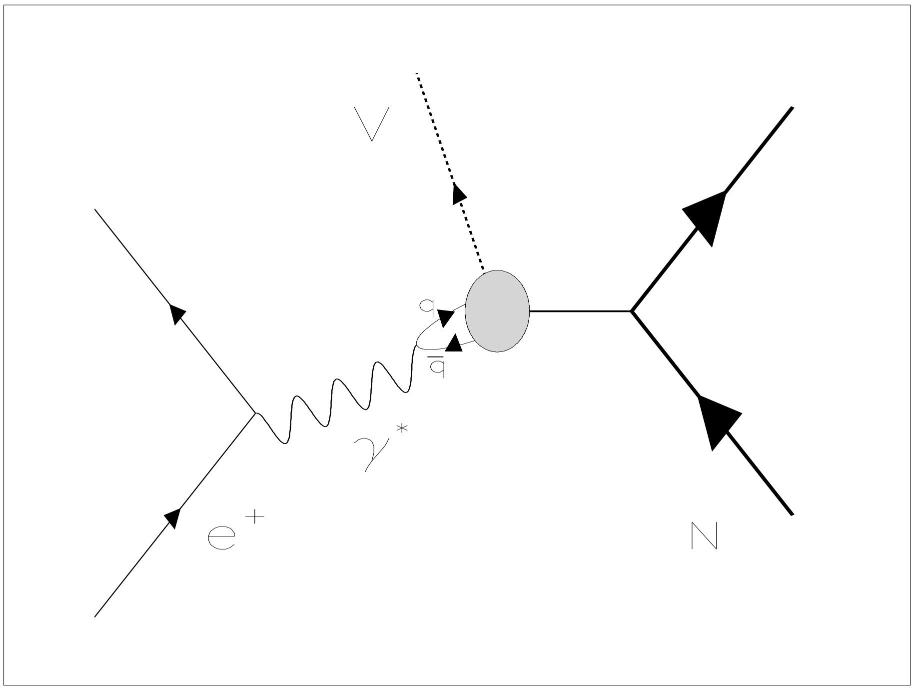

Figure 1.1: Diffractive vector meson production. Thanks to the existence of the virtual photon γ^* as a quark-antiquark pair, a strong interaction between the photon and the target nucleus N is possible, as a result of which a vector meson V may be produced.

the impact parameter b:

$$\frac{d\sigma}{dt} \sim e^{-b|t|} \ , \tag{1.2}$$

and such exponential dependence is also observed in diffractive scattering of light. b is related to the size of the target, and t denotes the momentum transfer from the beam particle (e^+) to the target.

Another consequence of the uncertainty principle arises from the very short lifetime of the ρ . With such a short lifetime, the uncertainty in measuring the rest energy of the ρ^0 becomes very large, and therefore the ρ^0 mass distribution has considerable width (Fig. 1.2).

The internal structure of the ρ^0 meson is also affected by the uncertainty

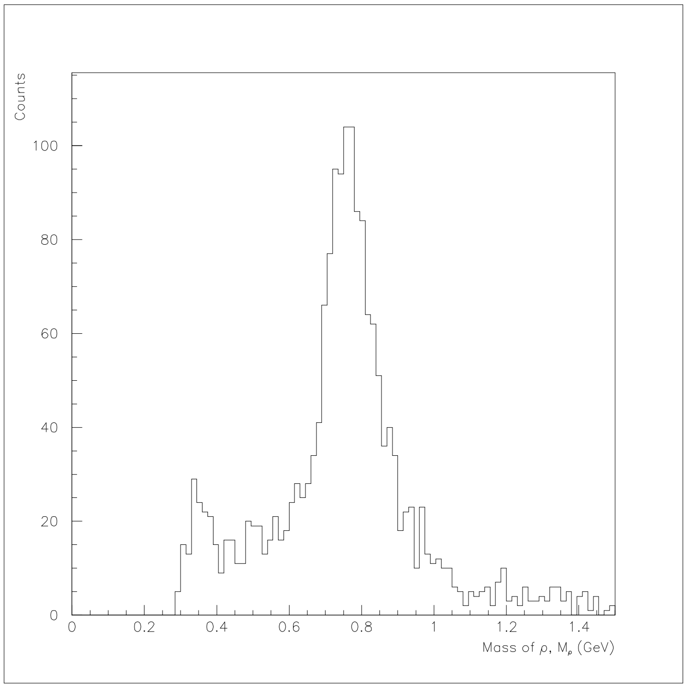

Figure 1.2: Mass measurements on a sample of selected ρ^0 events: the distribution has a considerable width. All ρ^0 selection cuts were applied.

principle. Since masses of the *up* and *down* quarks are almost equal within hadrons, it is equally probable to detect either an *up* or a *down* quark-antiquark pair as the constituent of the ρ^0 . The uncertainty principle allows a momentary annihilation of the quark-antiquark pair into a virtual photon, and a subsequent creation of another quark-antiquark pair from the photon. This mechanism explains fluctuations between the *up* and *down* pairs. Accordingly, the structure of the ρ^0 is written as

$$\frac{1}{\sqrt{2}}(|u\bar{u}\rangle - |d\bar{d}\rangle), \tag{1.3}$$

where the factor of $\frac{1}{\sqrt{2}}$ is the normalisation constant.

Since the virtual photon fluctuates into vector mesons in the lower energy regime, it is plausible to regard the diffractively-produced vector mesons as *hadronic analogues* of the virtual photon. Indeed, both the *virtual* photon γ^*

and the neutral vector meson are uncharged massive spin-1 particles. Therefore, it is also plausible to compare properties of the real vector meson and the virtual photon that mediated its production. The subject of interest of this thesis is the relationship between *helicities* of the ρ^0 meson and the virtual photon, where the helicity of a particle is defined as the component of its spin in the direction of its motion. For a massive spin-1 particle, the possible values of helicity are –1, 0, and +1. Helicity of the γ^* is determined by analysing kinematic parameters of the scattered lepton. Determination of the helicity of the ρ^0 particle is more complicated and involves a study of angular distributions of its decay products, the pions. There exists a model, known as the *S-Channel Helicity Conservation* (SCHC), in which the helicity of the ρ^0 remains the same as that of the γ^*. This model is tested in this thesis.

Chapter 2 offers a mathematical description of the diffractive ρ^0 production mechanism. Chapter 3 offers a brief overview of the HERMES experiment, with emphasis on the particle detectors responsible for tracking and measurements. Chapter 4 provides a concise description of Monte Carlo simulations used in this thesis. Methods and results of analysis performed on data produced at HERMES in 1996 and 1997 with a ^{1}H target are discussed in Chapter 5.

Chapter 2

Diffractive ρ^0 Production

This chapter introduces the kinematic parameters used in the selection of ρ^0 events and describes the coordinate systems involved. The chapter provides a description of the theoretical framework of ρ^0 decay distribution analysis. The theoretical description evolves into a detailed introduction of the specific experimental goals of this thesis: determination of the Spin Density Matrix Elements and their agreement/disagreement with S-Channel Helicity Conservation and Natural Parity Exchange.

2.1 Event Selection and Interaction Kinematics

The process of interest for this thesis is diffractive ρ^0 production. The target remains intact in the process. There exist other mechanisms of ρ^0 production that manifest themselves at HERMES. These background processes need to be taken into account in order to separate the diffractive ρ^0s from the rest of the events.

The following requires introduction of a very convenient concept for relativity and particle physics — the *four-momentum*. For a particle of energy E and momentum $\mathbf{p}$, the four-momentum is defined as a vector with four components:

$$p = (p_0, p_1, p_2, p_3) = (E, \mathbf{p}) \ . \tag{2.1}$$

The component p_0 therefore denotes energy; p_1, p_2, p_3 denote x-, y-, and z-components of the conventional three-momentum, respectively. The dot-product of four-momenta p and q is defined as

$$p \cdot q = p_0 q_0 - p_1 q_1 - p_2 q_2 - p_3 q_3 \ . \tag{2.2}$$

Mathematical expressions of laws of physics written in terms of four-momenta conveniently preserve their form in all inertial frames, i.e. such expressions are invariant under Lorentz transformations. Incidentally,

$$p \cdot p = E^2 - \mathbf{p}^2 = M_0^2 \ , \tag{2.3}$$

where M_0 is the rest mass of the particle, regardless of the reference frame.

The dominant background process is Deep Inelastic Scattering (DIS) involving target fragmentation, where the ρ^0 meson sometimes emerges as one of the target fragments. A beam of positrons with four-momentum k strikes the target with four-momentum P_T, and a photon is exchanged between the positron and the target nucleus (Fig. 2.1). As a result of such an interaction, fragmentation of the target into entities with four-momenta P_1', P_2', ... , P_n' occurs. These fragments are hadrons, with the total four-momentum of the final hadronic state P' defined as

$$P' = P_1' + P_2' + \cdots + P_n' \ . \tag{2.4}$$

As a result of the interaction the positron transfers some of its four-momentum and emerges with a final four-momentum k'. The momentum transfer occurs via the virtual photon that takes away four-momentum

$$q = k - k' \tag{2.5}$$

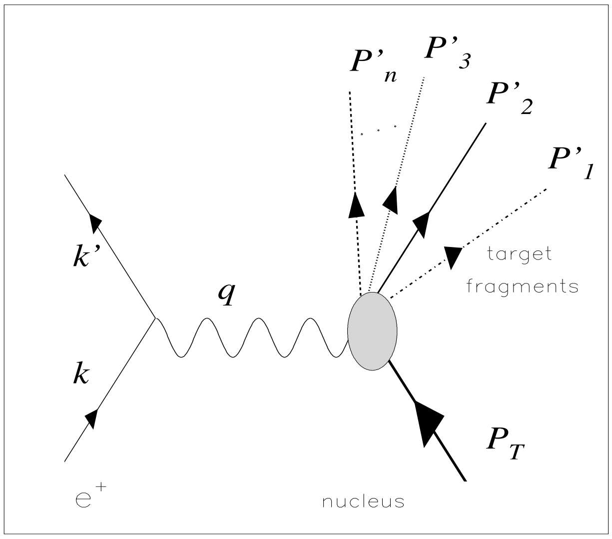

Figure 2.1: Deep Inelastic Scattering. The virtual photon with the four-momentum q causes a fragmentation of the target nucleus with the initial four-momentum P_T; n particles with the 4-momenta P'_1, ..., P'_n comprise the final hadronic state.

from the incident positron and transfers it to the target:

$$P' = P_T + q \ . \tag{2.6}$$

As all target fragments are real and massive particles, $P'^2 = W^2 > 0$, where the invariant mass of the final hadronic state W is defined as

$$W = \sqrt{P'^2} \ . \tag{2.7}$$

From definition (2.5) and using (2.3), it follows that in any frame of reference

$$q^2 = 2(M_e^2 + |\mathbf{k}||\mathbf{k}'|\cos\theta_e - E_e E'_e) \ , \tag{2.8}$$

where M_e is the rest mass of the positron, $\mathbf{k}$ and $\mathbf{k}'$ are its incident and scattered momenta, E_e and E'_e are its incident and scattered energies, and θ_e is the angle between the trajectories of incident and scattered positron. It follows from eqn.

2.3, that the value of q^2 is the same in any reference frame. Since the beam energy at HERMES ($E_e = 27.5$ GeV) in the lab frame is much greater than the rest mass of the positron ($M_e = 5.11 \times 10^{-4}$ GeV), it is plausible to apply the ultrarelativistic approximation

$$M_e \simeq 0, \;\; |\mathbf{k}| \simeq E_e, \;\text{ and } |\mathbf{k}'| \simeq E_e' \tag{2.9}$$

to the eqn. 2.8, and, after a trigonometric simplification, eqn. 2.8 yields

$$q^2 \overset{\text{lab}}{\simeq} -4E_e E_e' \sin^2(\frac{\theta_e}{2}) \; . \tag{2.10}$$

In the analysis described in this thesis, all calculations of q^2 were carried out through the ultrarelativistic approximation in the lab frame.

It is worth noting that q^2, the square of four-momentum of the photon, is always negative. A particle with four-momentum p is called *spacelike* if $p^2 < 0$, *lightlike* if $p^2 = 0$, and *timelike* if $p^2 > 0$. Whereas real massless particles are always lightlike and real massive particles are always timelike, only virtual particles can be spacelike. Hence it is customary to use a positive quantity

$$Q^2 = -q^2 \overset{\text{lab}}{\simeq} 4E_e E_e' \sin^2(\frac{\theta_e}{2}) \; , \tag{2.11}$$

which is called the *photon virtuality.*

Expansion of W^2 yields

$$W^2 = (P_T + q)^2 = M_T^2 + 2q \cdot P_T - Q^2, \tag{2.12}$$

where M_T^2 is the initial mass of the target. With expansion (2.12) in mind, it is convenient to define another Lorentz-invariant quantity

$$\nu = \frac{q \cdot P_T}{M_T} \; , \tag{2.13}$$

which is the energy carried to the target by the virtual photon in the lab frame:

$$\nu \overset{\text{lab}}{=} E_e - E_e' \; . \tag{2.14}$$

The square of the total four-momentum of the final hadronic states, which is the total energy in the centre of momentum (CM) frame of the photon-nucleus system, then becomes

$$W^2 = M_T^2 + 2M_T\nu - Q^2 \ . \tag{2.15}$$

This quantity is the same in all frames of reference and is simplest to calculate in the lab frame using eqns. 2.14 and 2.11. The ratio between ν and E_e, defined as

$$y = \frac{\nu}{E_e} \overset{\text{lab}}{=} \frac{E_e - E_e'}{E_e} \ , \tag{2.16}$$

represents the fraction of the energy transfered from the positron to the nucleus in the lab frame.

While the mechanism of the diffractive ρ^0 production (Fig. 2.2) is fundamentally different from that of Deep Inelastic Scattering, the assignment of dynamical variables is similar. Hence the definitions of k, k', q, Q^2 and P_T are the same for both processes. The four-momentum of the target after the collision is P_T', and that of the produced vector meson is P_V' ($P_V' = P_\rho'$ in this case). Therefore, the total four-momentum of the final hadronic state becomes

$$P' = P_T' + P_V' \ . \tag{2.17}$$

Since the ρ^0 meson is very short-lived, its four-momentum is measured as the sum of the four-momenta of its decay products, the $\pi^+\pi^-$ pair:

$$P_\rho' = P_{\pi^+} + P_{\pi^-} \ . \tag{2.18}$$

The four-momentum of the virtual photon q is partially carried off by the outgoing ρ^0 meson, and the four-momentum increment in the final target state is thus $q - P_\rho'$. The square of this quantity is defined as

$$t = (q - P_\rho')^2 \ . \tag{2.19}$$

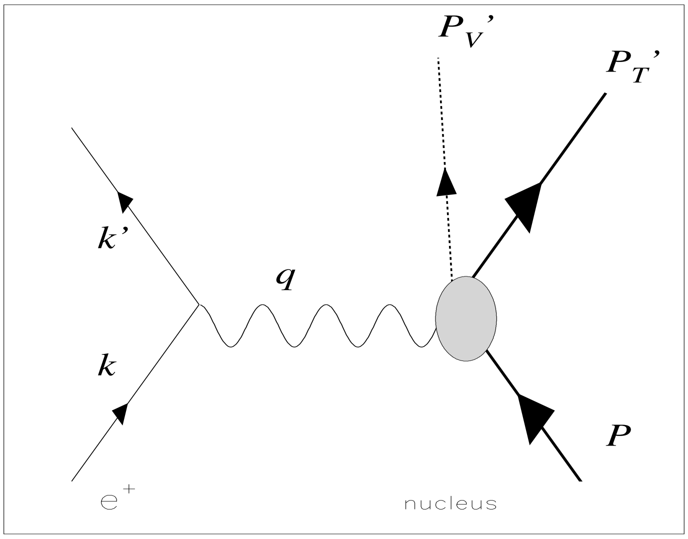

Figure 2.2: Diffractive ρ^0 Production. The virtual photon with the four-momentum q collides with the target nucleus with the initial four-momentum P_T; a vector meson with the 4-momentum P'_V is produced as a result, while the target remains intact acquiring four-momentum P'_T.

Since the lifetime of the ρ^0 is very short, the particle decays within the target and does not reach the detector, making direct ρ^0 detection impossible. It is possible, however, to select out ρ^0 events by measuring the net mass of a pair of two oppositely charged detected pions. The *invariant mass* $M_{2\pi}$, defined as

$$M_{2\pi} = \sqrt{P'^2_\rho} = \sqrt{(E_{\pi^+} + E_{\pi^-})^2 - (\mathbf{p}_{\pi^+} + \mathbf{p}_{\pi^-})^2}\ , \tag{2.20}$$

is an indicator of a ρ^0 event if its value is close to the ρ^0 mass of 768.5 MeV.

The final target state is not detected in the experiment, though it is still possible to calculate the mass of the total *undetected* hadronic final state:

$$M_X = \sqrt{(q + P_T - P'_V)^2}\ . \tag{2.21}$$

The undetected hadronic final state, depending on the type of interaction, is a single- or many-particle state. Since in the case of diffractive production, no

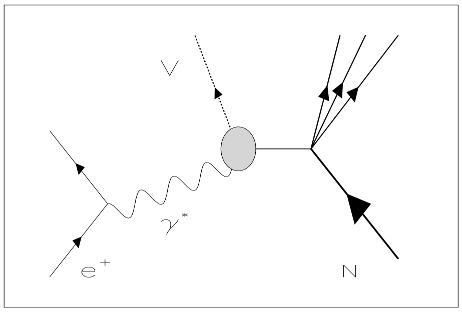

Figure 2.3: Diffractive Target Fragmentation. While the mechanism of ρ^0 production is the same as in the usual case of diffractive production (Fig. 1.1), the target breaks up.

additional particles are produced, it is useful for the selection of diffractive events to use the quantity

$$\Delta E = \frac{M_X^2 - M_T^2}{2M_T} \ . \tag{2.22}$$

For the case of a diffractive event, $\Delta E \equiv 0$, provided the target does not fragment.

Even though the ρ^0 is produced diffractively, it is still possible for the target to fragment, and therefore $M_X^2 > M_T^2$ in this case. This, along with the DIS, is an undesired background process called *diffractive target fragmentation* (Fig. 2.3); it is minimised by the requirement that ΔE be close to 0.

The momentum transfer to the nucleus in diffractive production is such that the produced ρ^0 meson is moving in nearly the same direction as the virtual photon. For the selection of diffractive events from the rest of the event spectrum, it is then useful to know the difference between the measured value of t and the value in the kinematic limit when the momentum vectors of the photon and the ρ^0 meson are collinear. In calculation of the value of t in this limiting case, denoted as t_0, the magnitudes of the momentum and energy are kept the same as those in calculation of the measured value of t. If an event is diffractive, the

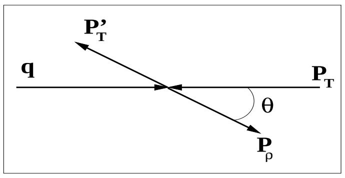

Figure 2.4: Momentum diagram of the photon-target interaction in the CM frame.

difference

$$t' = t - t_0 \tag{2.23}$$

is small, because it is expected that the photon and the diffractively-produced ρ^0 have collinear momenta.

It is important to note that while

$$t = M_{\rho^0}^2 - Q^2 + 2(\mathbf{p}_\rho \cdot \mathbf{q} - E_\rho E_{\gamma^*}) \tag{2.24}$$

is a Lorentz-invariant quantity and calculated in the lab frame for convenience, the calculation of t_0 must be performed in the CM frame of the photon-nucleus system. This restriction is due to the fact that in any other frame, energies and momenta of incoming particles, and energies and *magnitudes* of momenta of the outgoing particles *uniquely* define the angles between the directions of all momenta. That is, changing the angle between the momenta of the photon and the ρ^0 with given magnitudes of momenta of the ρ^0 and the nucleus will violate conservation of energy and momentum, and assuming an angle of $0°$ therefore renders the situation unphysical in any frame other than the CM. In the CM frame, however, where the sum of momenta of outgoing particles is zero, any rotation of the angle with given magnitudes of the outgoing momenta still preserves the zero total momentum; the conservation laws are not violated (Fig. 2.4). Following this argument, the calculation of t_0 is carried according to the relation

$$t_0 = (E_{\gamma CM} - E_{\rho CM})^2 - (\mathbf{q} - \mathbf{p}_{\rho CM})^2 \ , \tag{2.25}$$

where

$$E_{\gamma CM} = \frac{W^2 - Q^2 - M_\rho^2}{2\sqrt{W^2}} \tag{2.26}$$

and

$$E_{\rho CM} = \frac{W^2 + M_\rho^2 - M_X^2}{2\sqrt{W^2}} \ . \tag{2.27}$$

The variables mentioned in this section are summarised in Table 2.1.

2.2 Coordinate Systems

Since both the HERMES detector and the target are at rest with respect to the lab frame of reference, all data from the detector are first computed in the lab frame. In this frame, the z-axis points along the direction of the beam and coincides with the centre axis of the beam pipe (Fig. 2.5). The x-axis points radially outward, and the y-axis is defined as

$$\hat{y} = \hat{z} \times \hat{x} \ . \tag{2.28}$$

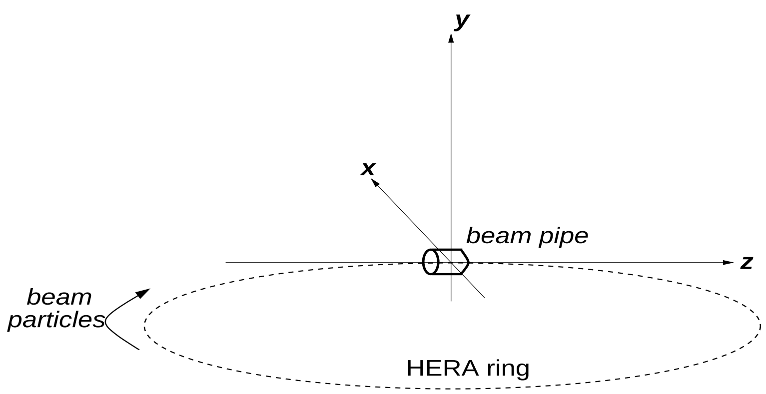

Figure 2.5: Axis definition in the rest frame.

Variable	**Description**
$k = (E_e, \mathbf{k})$	four-momentum of incident positron
$k' = (E'_e, \mathbf{k}')$	four-momentum of scattered positron
$q = k - k'$	four-momentum of virtual photon
$Q^2 = -q^2$	Photon virtuality
$P_T = (M_T, 0)$	four-momentum of target nucleus in the initial state
$P' = P'_1 + P'_2 + \cdots + P'_n$	four-momentum of final hadronic state
$W = \sqrt{P'^2} = \sqrt{P_T + q^2}$ $= \sqrt{M_T^2 + 2M_T\nu - Q^2}$	Magnitude of four-momentum of final hadronic state
$\theta_e,\ \phi_e$	Positron scattering angle ($\phi_e > 0$ for upper half of detector)
$\nu = \frac{q \cdot P_T}{M_T} \overset{\text{lab}}{=} E_e - E'_e$	In lab frame: energy of photon
$y = \frac{\nu}{E_e} \overset{\text{lab}}{=} \frac{E_e - E'_e}{E_e}$	Fraction of e^+ energy transferred to nucleus
$P'_V = (E_{\pi^+} + E_{\pi^-},\ \mathbf{p}_{\pi^+} + \mathbf{p}_{\pi^-})$	Four-momentum of candidate ρ^0
$M_{2\pi} = \sqrt{P'^2_V}$	Mass of candidate ρ^0
$M_X = \sqrt{(q + P_T - P'_V)^2}$	Invariant mass of undetected hadronic final state
$\Delta E = \frac{M_X^2 - M_T^2}{2M_T}$	Measure of mass difference between initial and final target states
$t = (q - P'_\rho)^2 < 0$	Squared four-momentum transfer to target
t_0	Minimum $\|t\|$ for fixed ν, Q^2, $M_{2\pi}$, and M_X
$t' = t - t_0$	Squared four-momentum transfer relative to case when γ^* and ρ^0 are collinear (given by t_0)

Table 2.1: Definitions of variables used.

When considering the interaction of the virtual photon with the nuclear target, it is useful to consider the photon-nucleus centre-of-momentum frame, often called in literature the *s-channel helicity frame* or the *hadronic CM frame*. In that frame (Fig. 2.6), the momenta of the incoming virtual photon ($\mathbf{q}^*$) and target nucleus ($\mathbf{P}^*{}_T$), and those of the outgoing ρ^0 meson ($\mathbf{P}'^*{}_\rho$) and target nucleus ($\mathbf{P}'^*{}_T$), all lie in one plane called the *vector meson production plane*. The momenta of the incident and scattered positron define another plane — the *lepton scattering plane*. An orthonormal coordinate set is defined for this frame.

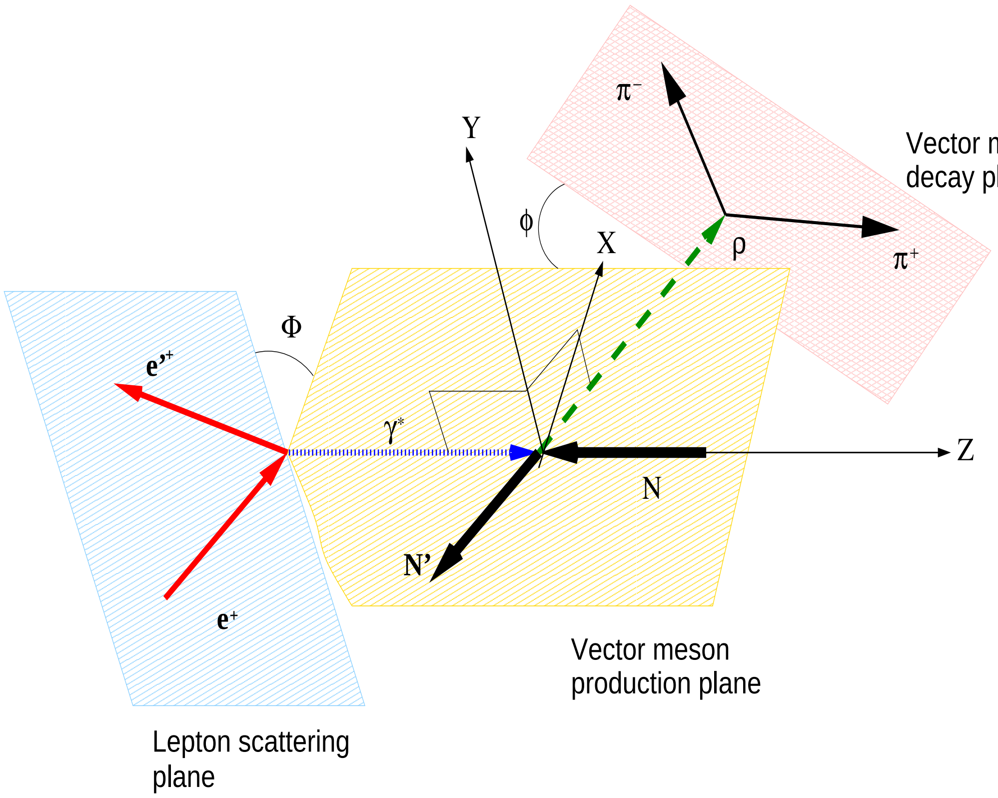

Figure 2.6: Photon-nucleus CM frame. Definition of angles Φ and ϕ. All involved particles are labelled in the figure.

The Z-axis points in the same direction as momentum of the virtual photon, the Y-axis is defined by the normal to the vector meson production plane, and the

X-axis — by the cross product between the unit vectors of the former two axes:

$$\hat{Z} = \frac{\mathbf{q}^*}{|\mathbf{q}^*|}\ ,\ \hat{Y} = \frac{\mathbf{q}^* \times \mathbf{P}'^*_\rho}{|\mathbf{q}^* \times \mathbf{P}'^*_\rho|}\ ,\ \hat{X} = \hat{Y} \times \hat{Z}\ . \tag{2.29}$$

The angle between the lepton scattering and vector meson production planes is called Φ. It is the same as the angle between the normal vectors to these planes. The normal to the vector meson production plane is the Y-axis. The normal to the lepton scattering plane is defined as a normalised cross product of incident and scattered momenta of the positron, k^* and k'^*:

$$\hat{n}_l = \frac{\mathbf{k}^* \times \mathbf{k}'^*}{|\mathbf{k}^* \times \mathbf{k}'^*|}\ . \tag{2.30}$$

In any frame of reference, conservation of momentum requires that the parent particle and its two daughter particles lie in the same plane. Hence, a third plane, called the *vector meson decay plane*, is defined in the hadronic CM frame. The normal to this plane is given by

$$\hat{n}_{vp} = \frac{\mathbf{p}^*{}_{\pi^+} \times \mathbf{p}^*{}_{\pi^-}}{|\mathbf{p}^*{}_{\pi^+} \times \mathbf{p}^*{}_{\pi^-}|}\ . \tag{2.31}$$

Angles between the Y-axis and $\hat{n}_{vp}$ define the angle between the production and decay planes, denoted as ϕ.

In the decay angular distribution analysis, it is best to use a coordinate system in which the parent particle is at rest. Then the two daughter particles (pions in this case) have collinear momenta that point in opposite directions (Fig. 2.7). In this frame, the polar angle θ is defined as the angle between the momentum of the positive pion and the negative of the momentum of the outgoing nucleus.

Angles θ, ϕ and Φ uniquely describe the decay angular distribution of the ρ^0 meson.

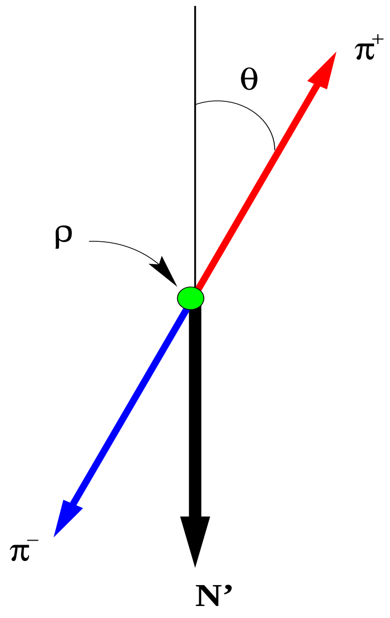

Figure 2.7: ρ^0 rest frame. All involved particles are labelled.

2.3 The Vector Meson Dominance Model

The Vector Meson Dominance Model (VMDM) allows the photon to exist as a superposition of the lightest vector mesons. Quantum-mechanically this is approximately described by decomposition of the physical photon wavefunction $|\gamma\rangle$ into the bare photon part $|\gamma_B\rangle$ and the hadron part $|h\rangle$ (see [4], p.271):

$$|\gamma\rangle \cong \sqrt{Z_3}|\gamma_B\rangle + \sqrt{\alpha}|h\rangle \ , \tag{2.32}$$

where $\sqrt{Z_3}$ and $\sqrt{\alpha}$ are normalisation constants. All states in (2.32) have the same three-momentum $\mathbf{q}$.

2.4 The Photon-Nucleon Interaction

Mediation of the interaction between the strongly interacting photon and the target nucleon has two contributions. At CM energy $W > 10$ GeV, the dominant mediation mechanism is due to the *Pomeron* (after I. Pomeranchuk) [5], which is thought to be a pair of gluons exchanged between the photon (which exists as a vector meson) and quarks of the nucleon. The Pomeron contributes to the increase in cross section with W. As a whole, the Pomeron has the quantum numbers of the vacuum [6], i.e. it is colourless, spinless *etc.* At CM energy $W < 4$ GeV, the presence of quarks increases with decreasing W; the mediation is dominated by the *Reggeon* (after T. Regge) [7], which is a term for the exchange of mesons (ρ , ω, f_2, a_2, ω_3, ρ_3, ...) (see [7], p. 144). The virtual photon is absorbed by a valence quark [8]. In this regime, the interaction cross section decreases with W.

HERMES operates at intermediate energies ($3.8 < W < 6.5$ GeV) and photon virtualities ($0.5 < Q^2 < 4$ GeV^2), therefore both exchange mechanisms contribute. The dependence of the total cross section on W is best described as follows [6]:

$$\sigma = X s^{\zeta} + Y s^{-\eta} \; , \tag{2.33}$$

where X, Y, ζ and η are positive numbers, nearly constant in s, with $s = W^2$. The first term in (2.33) is due to the Pomeron contribution, and the second one is due to the Reggeon contribution.

2.5 Natural Parity Exchange

At this point, it is desirable to discuss the exchange of parity between the photon and the nucleon. A state $|\Psi\rangle$ is said to have an $\begin{matrix} even \\ odd \end{matrix}$ parity if

$$|\Psi(x, y, z)\rangle = \pm|\Psi(-x, -y, -z)\rangle \; . \tag{2.34}$$

Odd parity is associated with parity quantum number $P = -1$, and even parity is associated with parity quantum number $P = 1$. Furthermore, the state is defined to have *natural* parity P if [7]

$$P = (-1)^{J-v} \tag{2.35}$$

and *unnatural* parity P if

$$P = (-1)^{J-v-1} \ , \tag{2.36}$$

where J is the total angular momentum quantum number, and (see [7], p.123)

$$v = \begin{cases} 0, \ J = \text{integer} \\ \frac{1}{2}, \ J = \text{half-odd-integer} \end{cases} . \tag{2.37}$$

Parity exchange between γ^* and N will be considered separately for Pomeron- and Reggeon-mediated interactions.

The requirement that the Pomeron possess the net quantum numbers of the vacuum implies that the Pomeron carries even parity, i.e. it does not alter the parity in either γ^*-ρ^0 or N-N' transitions. The same requirement implies that the total angular momentum of the Pomeron is 0, and hence, by definition 2.35, the parity of the Pomeron-mediated interaction is natural. In the case of the Reggeon, unnatural parity exchange is expected to contribute.

If the assumption of natural parity exchange is valid, there arise some simplifications in the description of the vector meson electroproduction cross section [9]. In this work, natural parity exchange is not assumed, but instead put to a test.

2.6 The $\gamma - \rho$ vertex: S-channel Helicity Conservation

The fact that the Pomeron carries zero angular momentum implies that the γ^* passes its angular momentum to the ρ^0, and, since the ρ^0 meson is expected to travel in the same direction as the "parent" γ^* in the case of diffractive production, it is expected from the above arguments that the Pomeron-mediated interactions render the helicity of the ρ^0 the same as that of the photon. This phenomenon is called the *s-channel Helicity Conservation* (SCHC). However, measurements performed at high W at ZEUS and H1, where the Reggeon is virtually non-existent, showed violations of SCHC on the order of 10%.

Unlike the Pomeron, the Reggeon is allowed to carry non-vacuum quantum numbers, and angular momentum transfer from the photon to the nucleus is generally not forbidden. Therefore the helicity of the ρ^0 may be different from the γ^*. Since the significant, if not dominant, contribution to the $\gamma^* - N$ interaction comes from the Reggeon, it remains to be seen whether SCHC is present at HERMES. SCHC offers numerous simplifications to the mathematical description of the ρ^0 electroproduction cross-section. Like natural parity exchange, it is not assumed, but tested instead.

2.7 Cross Section of ρ^0 Leptoproduction and the Spin Density Matrix

The scientific interest underlying this thesis is the comparison between the virtual photon and the ρ^0 ; specifically, the relationship between the helicity of the photon and its hadronic analogue. This section discusses the mathematical treatment of the problem.

The diffractive leptonic ρ^0 production is a process of the form

$$lN \to l'N'V \ , \tag{2.38}$$

where l is the lepton, N is the target nucleus, and V is the vector meson.

The differential cross section for such a process is given by [9]

$$\frac{d\sigma_{lN\to l'N'V'}}{dE'_e\ d\Omega\ d\Phi\ dt} = \frac{1}{(2\pi)^5}\frac{E'_e}{E_e}\frac{M_e^2}{4(P'_V+Q^2)^{\frac{1}{2}}}\frac{1}{Q^4}\frac{1}{4}\sum_{final spins}|\mathcal{M}|^2 \ , \tag{2.39}$$

where Ω is the solid angle of the scattered lepton, and $\mathcal{M}$ is the production amplitude of the leptoproduction. In the above formula, $\sum_{final spins}|\mathcal{M}|^2$ represents the summation over all possible allowed combinations of the spin states of the final particles, and the coefficient $\frac{1}{4}$ represents averaging over the four possible combinations of initial spin states of the positron and the nucleon. The square of the scattering amplitude consists of leptonic ($L_{\mu\nu}$) and hadronic ($T^{\mu\nu}$) components (Refs. [9] and [10], p.41):

$$\sum_{spins}|\mathcal{M}|^2 = \sum_{spins} L_{\mu\nu}T^{\mu\nu} \ , \tag{2.40}$$

In general, $L_{\mu\nu}$ is separated into two parts:

$$L_{\mu\nu} = \tilde{L}_{\mu\nu} + \tilde{M}_{\mu\nu} \ . \tag{2.41}$$

$\tilde{L}_{\mu\nu}$, called the *leptonic tensor*, is the spin-independent part; $\tilde{M}_{\mu\nu}$ is the spin-dependent part which does not contribute if the average polarisation of the incident beam leptons is zero. At HERMES, the average polarisation of the positron beam in 1996 and 1997 was not zero.

The leptonic tensor is expressed in terms of the electomagnetic current operator j_μ^{el} sandwiched between the final and initial positron states k' and k, respectively.

$$\tilde{L}_{\mu\nu} = \sum_{positron\ spins} M_e^2\langle k'|j_\mu^{el}|k\rangle\langle k'|j_\nu^{el}|k\rangle^* = M_e^2\mathrm{Tr}\left(\frac{\not{k}'+M_e}{2M_e}\gamma_\mu\frac{\not{k}+M_e}{2M_e}\gamma_\nu\right), \tag{2.42}$$

where the asterisk (*) denotes the complex conjugate, the γ_μ are the Dirac matrices (see Appendix A), and $\not{k}'$ and $\not{k}$ are 4×4 matrices for the scattered and incident lepton, respectively, defined as

$$\not{A} = A_\mu\gamma^\mu \tag{2.43}$$

for a general 4-vector A.

In a coordinate system where the z-axis (axis 3) is chosen parallel to the virtual photon propagation, $\tilde{L}_{\mu\nu}$ describes the photon spin states with transverse (x, y), longitudinal (z) and timelike, or scalar, (0) components [10]. The longitudinal and scalar components transform into each other, and therefore only a 3×3 tensor is necessary to fully describe the production amplitude $\mathcal{M}$. The tensor is obtained in the helicity basis using a 3×4 transformation matrix X [9]

$$\tilde{L}_{\lambda\lambda'} = \sum_{\mu,\nu} X_{\lambda\mu} \tilde{L}_{\mu\nu} X^{-1}_{\nu\lambda'} \ , \tag{2.44}$$

with λ and λ' being the helicity states of the photon (λ, $\lambda' = 1, 0, -1$). In a similar way, it is possible to obtain the polarisation-dependent component $\tilde{M}$. The *photon density matrix* is then defined as

$$\rho(\gamma)_{\lambda\lambda'} = \frac{1-\epsilon}{Q^2}(\tilde{L}_{\lambda\lambda'} + \tilde{M}_{\lambda\lambda'}) = \rho(\gamma)_{unpol} + \rho(\gamma)_{pol} \ , \tag{2.45}$$

where ϵ is the *photon polarisation parameter* defined as the ratio of fluxes of the longitudinal and transverse photons, and calculated using the approximation $M^2 \ll Q^2 \ll E^2$:

$$\epsilon \simeq \frac{1-y}{1-y+\frac{1}{2}y^2} \ , \ 0 \leq \epsilon \leq 1 \ , \tag{2.46}$$

with y given by (2.16).

Following [9], it is possible to express the cross section in (2.39) in terms of the cross section of the virtual process $\gamma^* N \to V'N'$:

$$\frac{d\sigma_{lN\to l'N'V'}}{dE'_e \ d\Omega \ d\Phi \ dt} = \frac{1}{(2\pi)^3} \frac{E'_e}{E_e} \frac{M_e^2}{Q^2} \frac{1}{1-\epsilon} \frac{d\sigma_{\gamma^* N\to V'N'}}{d\Phi \ dt} \ . \tag{2.47}$$

With the approximation $M_e^2 \ll Q^2$, the explicit form of the unpolarised and polarised contributions is given as follows:

$$\rho(\gamma)_{unpol} = \frac{1}{2}\begin{pmatrix} 1 & \sqrt{\epsilon(1+\epsilon)}e^{-i\Phi} & -\epsilon e^{-2i\Phi} \\ \sqrt{\epsilon(1+\epsilon)}e^{i\Phi} & 2\epsilon & -\sqrt{\epsilon(1+\epsilon)}e^{-i\Phi} \\ -\epsilon e^{2i\Phi} & -\sqrt{\epsilon(1+\epsilon)}e^{i\Phi} & 1 \end{pmatrix} \qquad (2.48)$$

and

$$\rho(\gamma)_{pol} = \frac{P_b\sqrt{1-\epsilon}}{2}\begin{pmatrix} \sqrt{1+\epsilon} & \sqrt{\epsilon}e^{-i\Phi} & 0 \\ \sqrt{\epsilon}e^{i\Phi} & 0 & \sqrt{\epsilon}e^{-i\Phi} \\ 0 & \sqrt{\epsilon}e^{i\Phi} & -\sqrt{1+\epsilon} \end{pmatrix} , \qquad (2.49)$$

where P_b is the longitudinal polarisation coefficient of the beam.

The photon density matrix is decomposed into an orthogonal basis of 9 independent Hermitian matrices Σ^α (a matrix A is Hermitian if $A_{mn} = A^*_{nm}$), $\alpha = 0, \ \ldots, \ 8$:

$$\rho(\gamma) = \frac{1}{2}\sum_{\alpha=0}^{8}\tilde{\Pi}^\alpha\Sigma^\alpha \ . \qquad (2.50)$$

The Σ^α matrices, equivalent to Pauli spin matrices for spin-$\frac{1}{2}$ particles, select the contribution from photons with various polarisation states, and $\tilde{\Pi}$ is a 9-component vector (see Appendix B). The indices α are such that $\alpha = 0, 1, 2, 3, 4$ represent unpolarised photons, the two directions of transverse polarisation, circular polarisation and longitudinal polarisation, respectively. The remaining matrices with $\alpha = 5, ..., 8$ represent longitudinal-transverse interference. For an unpolarised lepton beam, only $\alpha = 5, 6$ contribute. If the beam is longitudinally polarised, there are additional non-zero components with $\alpha = 7, 8$; these correspond to the circular component of the virtual photon polarisation [11]. Since the ρ^0 and γ^* are so similar, apart from the ρ^0 having the valence quark content, it is expected that the ρ^0 *spin density matrix* is related to the photon density matrix. Indeed, the ρ^0 spin density matrix $\rho(V)$ is expressed through the photon spin density matrix as follows:

$$\tilde{\rho}(V) = T\rho(\gamma)T^\dagger \ , \qquad (2.51)$$

where T is the matrix $T^{\mu\nu}$ in (2.40), and the "$\dagger$" denotes a Hermitian adjoint matrix. For practical purposes, it is best to use the normalised matrix

$$\rho(V) = \frac{\tilde{\rho}(V)}{\int \frac{d\Phi}{2\pi} \mathrm{Tr}(\tilde{\rho}(V))} \ . \tag{2.52}$$

The ρ^0 density matrix is also expressed in the basis of 9 matrices ρ^α

$$\rho(V) = \sum_{\alpha=0}^{8} \Pi^\alpha \rho^\alpha \ , \tag{2.53}$$

with components related to the Σ^α matrix components through

$$\rho^\alpha_{\lambda_V \lambda'_V} = \frac{1}{2N_\alpha} \sum_{\lambda_{N'}, \lambda_N, \lambda_\gamma, \lambda'_\gamma} T_{\lambda_V \lambda_{N'} \lambda_\gamma \lambda_N} \Sigma^\alpha_{\lambda_\gamma \lambda'_\gamma} T^*_{\lambda'_V \lambda_{N'} \lambda'_\gamma \lambda_N} \ , \tag{2.54}$$

where (*) denotes a complex conjugate, and indices λ and λ' represent helicities of the indicated particles [9]. Components $T_{\lambda_V \lambda_{N'} \lambda_\gamma \lambda_N}$ are called the *helicity amplitudes.* The vector Π is given in Appendix C.

From the fact that parity is conserved in strong interactions and from simmetry properties of Σ^α, it is shown in [9] that the ρ^α obey the following symmetry relations:

$$\begin{aligned} \rho^\alpha_{-\lambda -\lambda'} &= (-1)^{\lambda-\lambda'} \rho^\alpha_{\lambda\lambda'} \ , \qquad \alpha = 0,1,4,5,8; \\ \rho^\alpha_{-\lambda -\lambda'} &= -(-1)^{\lambda-\lambda'} \rho^\alpha_{\lambda\lambda'} \ , \qquad \alpha = 2,3,6,7. \end{aligned} \tag{2.55}$$

This section gave a brief introduction to the ρ^0 spin density matrix from the decomposition of the production cross section. The matrix $\rho(V)$ is instrumental in the description of the angular distribution of the decay products of the ρ^0 meson. The analysis of decay angular distributions of the pions makes verification of SCHC and natural parity exchange possible. The following two sections address the angular distribution analysis.

2.8 Angular Distribution Function

The analysis of ρ^0 production and decay involves measuring the number of decay particles in a solid angle. Over the whole space, the number distribution of the detected particles defines the angular distribution function:

$$\frac{dN}{d\cos\theta d\phi} = W(\theta,\phi) \ . \tag{2.56}$$

The angular distribution is defined in the ρ^0 rest frame as follows (see Refs. [12] and [9]):

$$\begin{aligned} W(\theta,\phi) &= \frac{3}{4\pi} D^1_{\lambda 0}(\phi,\theta,-\phi)^* \ \rho^{\lambda\lambda'}(V) \ D^1_{\lambda' 0}(\phi,\theta,-\phi) \\ &= \frac{3}{4\pi} D^1_{\lambda 0}(\phi,\theta,-\phi)^* \Pi_\alpha \rho^\alpha_{\lambda\lambda'}(V) D^1_{\lambda' 0}(\phi,\theta,-\phi) \ , \end{aligned} \tag{2.57}$$

where D are the Wigner rotation functions given by

$$\begin{aligned} D^1_{10}(\phi,\theta,-\phi) &= -\frac{1}{\sqrt{2}} \sin\theta \ \mathrm{e}^{-i\phi} \ , \\ D^1_{00}(\phi,\theta,-\phi) &= \cos\theta \ , \\ D^1_{-10}(\phi,\theta,-\phi) &= \frac{1}{\sqrt{2}} \sin\theta \ \mathrm{e}^{i\phi} \ . \end{aligned} \tag{2.58}$$

Symmetry properties (2.55) and the trace conditions

$$\mathrm{Tr}\rho^0 = \mathrm{Tr}\rho^4 = 1 \tag{2.59}$$

greatly simplify the angular distribution. As a result, the final shape of the angular distribution in the general case, as a function of Φ, θ, ϕ, is given by only a few surviving independent elements. Its polarisation-independent part is given by

$$
\begin{aligned}
W^{unpol}(\cos\theta,\ \phi,\ \Phi) = \tfrac{1}{1+\epsilon R}\tfrac{3}{4\pi}\Bigg[& \tfrac{1}{2}(1-\rho^0_{00}) + \tfrac{1}{2}(3\rho^0_{00}-1)\ \cos^2\theta \\
& -\sqrt{2}\ \mathrm{Re}(\rho^0_{10})\sin 2\theta\cos\phi - \rho^0_{1-1}\sin^2\theta\cos 2\phi \\
& -\epsilon\cos 2\Phi\Big\{\rho^1_{11}\sin^2\theta + \rho^1_{00}\cos^2\theta \\
& -\sqrt{2}\ \mathrm{Re}(\rho^1_{10})\sin 2\theta\cos\phi - \rho^1_{1-1}\sin^2\theta\cos 2\phi\Big\} \\
& -\epsilon\sin 2\Phi\Big\{\sqrt{2}\ \mathrm{Im}(\rho^2_{10})\sin 2\theta\sin\phi + \mathrm{Im}(\rho^2_{1-1})\sin^2\theta\sin 2\phi\Big\} \\
& +\epsilon R\Big\{\tfrac{1}{2}(1-\rho^4_{00}) + \tfrac{1}{2}(3\rho^4_{00}-1)\cos^2\theta \\
& -\sqrt{2}\ \mathrm{Re}(\rho^4_{10})\sin 2\theta\cos\phi - \rho^4_{1-1}\sin^2\theta\cos 2\phi\Big\} \\
& +\sqrt{2\epsilon R(1+\epsilon)}\cos\Phi\Big\{\rho^5_{11}\sin^2\theta + \rho^5_{00}\cos^2\theta \\
& -\sqrt{2}\ \mathrm{Re}(\rho^5_{10})\sin 2\theta\cos\phi - \rho^5_{1-1}\sin^2\theta\cos 2\phi\Big\} \\
& +\sqrt{2\epsilon R(1+\epsilon)}\sin\Phi\left\{\sqrt{2}\ \mathrm{Im}(\rho^6_{10})\sin 2\theta\sin\phi + \mathrm{Im}(\rho^6_{1-1})\sin^2\theta\sin 2\phi\right\}\Bigg].
\end{aligned}
\tag{2.60}
$$

If the lepton beam has non-zero longitudinal polarisation, an additional part contributes:

$$
\begin{aligned}
W^{pol}(\cos\theta,\ \phi,\ \Phi) = \frac{1}{1+\epsilon R}\frac{3}{4\pi}P_b\Bigg[& \sqrt{1-\epsilon^2}\Big\{\sqrt{2}\ \mathrm{Im}(\rho^3_{10})\sin 2\theta\sin\phi \\
& +\mathrm{Im}(\rho^3_{1-1})\sin^2\theta\sin 2\phi\Big\} \\
& +\sqrt{2\epsilon(1-\epsilon)R}\cos\Phi\left\{\sqrt{2}\ \mathrm{Im}(\rho^7_{10})\sin 2\theta\sin\phi + \mathrm{Im}(\rho^7_{1-1})\sin^2\theta\sin 2\phi\right\} \\
& +\sqrt{2\epsilon(1-\epsilon)R}\sin\Phi\Big\{\rho^8_{11}\sin^2\theta + \rho^8_{00}\cos^2\theta \\
& -\sqrt{2}\ \mathrm{Re}(\rho^8_{10})\sin 2\theta\cos\phi - \rho^8_{1-1}\sin^2\theta\cos 2\phi\Big\}\Bigg].
\end{aligned}
\tag{2.61}
$$

R in the above equations is the ratio of longitudinal to transverse components of the total cross section:

$$
R = \frac{\sigma_L}{\sigma_T}\ . \tag{2.62}
$$

When the separation between σ_L and σ_T is not required, matrix elements are grouped for simplicity as follows[9]:

$$r_{ik}^{04} = \frac{\rho_{ik}^0 + \epsilon R \rho_{ik}^4}{1+\epsilon R} \; ;$$
$$r_{ik}^{\alpha} = \begin{cases} \frac{\rho_{ik}^{\alpha}}{1+\epsilon R} \,, & \alpha = 1, \ldots, 3; \\ \frac{\sqrt{R}\rho_{ik}^{\alpha}}{1+\epsilon R} \,, & \alpha = 5, \ldots, 8. \end{cases} \tag{2.63}$$

This work does not require the separation of components of the cross section, and the resulting angular distributions now become

$$\begin{aligned} W^{unpol}(\cos\theta,\ \phi,\ \Phi) = \frac{3}{4\pi}\Big[& \tfrac{1}{2}(1 - r_{00}^{04}) + \tfrac{1}{2}(3r_{00}^{04} - 1)\ \cos^2\theta \\ & -\sqrt{2}\ \mathrm{Re}(r_{10}^{04}) \sin 2\theta \cos\phi - r_{1-1}^{04} \sin^2\theta \cos 2\phi \\ & -\epsilon \cos 2\Phi \Big\{ r_{11}^1 \sin^2\theta + r_{00}^1 \cos^2\theta \\ & -\sqrt{2}\ \mathrm{Re}(r_{10}^1) \sin 2\theta \cos\phi - r_{1-1}^1 \sin^2\theta \cos 2\phi \Big\} \\ & -\epsilon \sin 2\Phi \Big\{ \sqrt{2}\ \mathrm{Im}(r_{10}^2) \sin 2\theta \sin\phi + \mathrm{Im}(r_{1-1}^2) \sin^2\theta \sin 2\phi \Big\} \\ & +\sqrt{2\epsilon(1+\epsilon)} \cos\Phi \Big\{ r_{11}^5 \sin^2\theta + r_{00}^5 \cos^2\theta \\ & -\sqrt{2}\ \mathrm{Re}(r_{10}^5) \sin 2\theta \cos\phi - r_{1-1}^5 \sin^2\theta \cos 2\phi \Big\} \\ & +\sqrt{2\epsilon(1+\epsilon)} \sin\Phi \ \Big\{ \sqrt{2}\ \mathrm{Im}(r_{10}^6) \sin 2\theta \sin\phi + \mathrm{Im}(r_{1-1}^6) \sin^2\theta \sin 2\phi \Big\} \Big] \end{aligned} \tag{2.64}$$

and

$$\begin{aligned} W^{pol}(\cos\theta,\ \phi,\ \Phi) = \frac{3}{4\pi} P_b \Big[& \sqrt{1-\epsilon^2} \Big\{ \sqrt{2}\ \mathrm{Im}(r_{10}^3) \sin 2\theta \sin\phi \\ & +\mathrm{Im}(r_{1-1}^3) \sin^2\theta \sin 2\phi \Big\} \\ & +\sqrt{2\epsilon(1-\epsilon)} \cos\Phi \ \Big\{ \sqrt{2}\ \mathrm{Im}(r_{10}^7) \sin 2\theta \sin\phi + \mathrm{Im}(r_{1-1}^7) \sin^2\theta \sin 2\phi \Big\} \\ & +\sqrt{2\epsilon(1-\epsilon)} \sin\Phi \Big\{ r_{11}^8 \sin^2\theta + r_{00}^8 \cos^2\theta \\ & -\sqrt{2}\ \mathrm{Re}(r_{10}^8) \sin 2\theta \cos\phi - r_{1-1}^8 \sin^2\theta \cos 2\phi \Big\} \Big]. \end{aligned} \tag{2.65}$$

In addition to the reduction of the number of spin density matrix elements, the dependence on R is now removed.

2.9 S-Channel Helicity Conservation and Natural Parity Exchange in $W(\theta,\ \phi,\ \Phi)$

Attention is now turned to the one-dimensional distributions.

By integration of (2.65) over ϕ and averaging over Φ, the distribution $W(\cos\theta)$ is obtained:

$$W(\cos\theta) = \frac{3}{4}[1 - r^{04}_{00} + (3r^{04}_{00} - 1)\cos^2\theta] \ . \tag{2.66}$$

$W(\cos\theta)$ is not constrained by SCHC. The angular distribution in ϕ is obtained by integrating over $\cos\theta$ and averaging over Φ:

$$W(\phi) = \frac{1}{2\pi}\left[1 - 2r^{04}_{1-1}\cos 2\phi + P_b\sqrt{1-\epsilon^2}\ \mathrm{Im}(r^3_{1-1})\sin 2\phi\right] \ . \tag{2.67}$$

If SCHC holds, $W(\phi) = \frac{1}{2\pi}$. After integration over $\cos\theta$ and averaging over ϕ, only components $r^{1,\ 5,\ 8}_{ii}$ remain. Using the definition $\mathrm{Tr}(A) \equiv \sum_i A_{ii}$ and parity conservation, wherein $r^\alpha_{11} = r^\alpha_{-1-1}$ for $\alpha = 0,\ 1,\ 4,\ 5,\ 8$, the angular distribution in Φ is obtained:

$$W(\Phi) = \frac{1}{2\pi}\Big[1 - \epsilon\cos 2\Phi\ \mathrm{Tr}(r^1) + \sqrt{2\epsilon(1+\epsilon)}\cos\Phi\ \mathrm{Tr}(r^5) + P\sqrt{2\epsilon(1-\epsilon)}\sin\Phi\ \mathrm{Tr}(r^8)\Big] \ . \tag{2.68}$$

If SCHC holds, $W(\Phi) = \frac{1}{2\pi}$. In addition, if SCHC is valid, it is possible to express the angular distribution in ϕ and Φ in terms of the *polarisation angle* $\psi = \phi - \Phi$ by integration over $\cos\theta$:

$$W(\psi) = \frac{1}{2\pi}[1 + 2\epsilon r^1_{1-1}\cos 2\psi] \ . \tag{2.69}$$

From the above description, if SCHC is valid, it follows that

$$r^{04}_{1-1} = \ \mathrm{Im}(r^3_{1-1}) = \mathrm{Tr}(r^{1,5,8}) = 0 \ . \tag{2.70}$$

If, in addition to SCHC, natural parity exchange is valid, r^{04}_{00} and r^1_{1-1} are related through [9]

$$2r^1_{1-1} = 1 - r^{04}_{00} \ . \tag{2.71}$$

The experimental tests of SCHC and natural parity exchange lie therefore in direct measurement of r^{04}_{00}, r^{1}_{1-1}, r^{04}_{1-1}, $\mathrm{Im}(r^{3}_{1-1})$, $\mathrm{Tr}(r^1)$, $\mathrm{Tr}(r^5)$, $\mathrm{Tr}(r^8)$, and subsequent verification of relationships (2.70) and (2.71).

In this study, the measurement of the above-mentioned matrix elements is accomplished by fitting the angular distribution functions, described by (2.66), (2.67), (2.68) and (2.69) into the experimental angular distribution. Chapter 5 contains details of the fitting procedure and a summary of experimental results.

Chapter 3

Apparatus

The HERMES (HERa MEasurement of Spin) experiment is conducted at *Deutsches Elektronen-Synchrotron* (DESY) in Hamburg, Germany. The 27.5 GeV positron beam is accelerated by the *Hadron-Elektron Ring Anglage* (HERA). Located in the East Hall of HERA, the HERMES spectrometer is a forward angle instrument of conventional design.

The polar and azimuthal scattering angles and the initial trajectory for the determination of the particle's momentum are measured by the front tracking system. The momentum measurement is completed by two sets of drift chambers behind the magnet. Three proportional chambers are installed in the magnet to help match front and back tracks and to track low-momentum particles that do not reach the rear section of the spectrometer. Particle identification is provided by a threshold Čerenkov detector, a transition radiation detector, a preshower detector and a lead-glass calorimeter. The system has relatively large acceptance and is capable of multiple track detection.

3.1 The HERA Synchrotron

The HERA ring, 6.3 km in circumference, is capable of operating a 27.5 GeV positron beam and a 919 GeV proton beam in separate beampipes. At HERMES, located in the East Hall of HERA (Fig. 3.1), the proton beam is not used — beam positrons collide with a fixed gaseous target. Another fixed-target experiment is

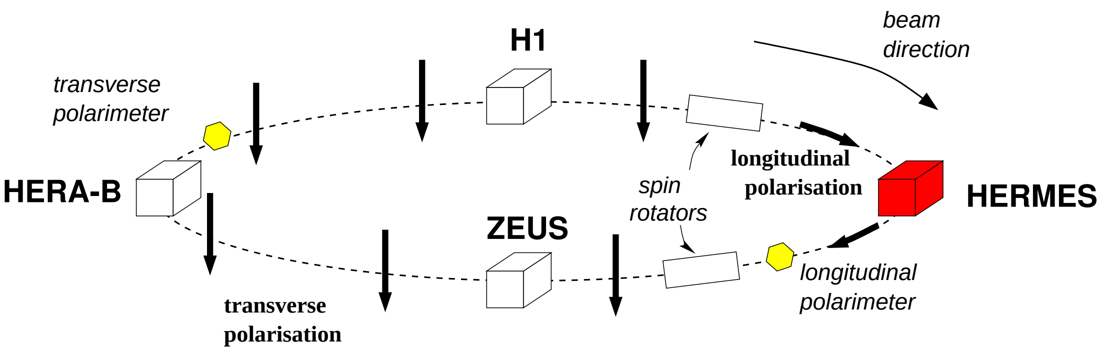

Figure 3.1: Direction of positron polarisation within the HERA ring.

HERA-B located in the West Hall, which, unlike HERMES, uses only the proton beam colliding with a thin metal wire target. Two e^+p collider experiments, H1 and ZEUS are located in the North and South Halls, respectively. Proper operation of each experiment is possible only if the other experiments operate in the way that does not affect the beam conditions very adversely.

Circular motion of electrons and positrons in a synchrotron is characterised by centripetal acceleration continuously imparted to the particles. The acceleration causes the charged leptons to continuously emit photons. This effect is called *synchrotron radiation*, which is a form of *bremmstrahlung*. The emission of sychrotron radiation sometimes causes the leptons to flip their spins. For a positive particle, presence of the magnetic field makes the parallel alignment between spin and the direction of the bending magnetic field more likely than the antiparallel alignment. As a result, a beam of initially unpolarised electrons or positrons eventually acquires transverse polarisation; the phenomenon is called the *Sokolov-Ternov effect*. The asymptotic buildup in polarisation is given by

$$P = P_{max}(1 - e^{-t/\tau}), \tag{3.1}$$

where t is the time elapsed since the injection of the beam into the accelerator and τ is the *buildup time*, the time it takes to reach $(1-\frac{1}{e}) \approx 63.21\%$ of the maximum possible polarisation P_{max}. With an ideally flat accelerator and in the absence of any depolarising effects, the maximum attainable polarisation is $P_{ST} = 92.4\%$ [13], with the buildup time of τ_{ST}. τ_{ST} is a property of the accelerator, and is equal to 37 min for HERA at 27.5 GeV. P_{max} is then given by

$$P_{max} = \frac{\tau}{\tau_{ST}} P_{ST}. \tag{3.2}$$

Hence, P_{max} is a function of τ only; τ is not a constant, but depends on many factors that affect the beam conditions.

The measurement of the DIS spin structure functions is one of the principal goals of the HERMES experiment. The measurement of a structure function g_1 (see, for example, [14]) requires longitudinal polarisation of the beam. Accordingly, spin rotators are installed on both sides of the HERMES detector area; they operate without any polarisation loss. The operational principle of the spin rotators is described as follows.

The behaviour of a charged spin-1/2 particle when placed in a uniform magnetic field $\mathbf{B}$ at a non-zero angle with respect to the direction of the spin angular momentum vector is characterised by a precession of the particle about the direction of $\mathbf{B}$. The angle of precession is the angle between $\mathbf{B}$ and initial direction of spin $\mathbf{S_0}$. The angular frequency of precession ω for positron is given by [17]

$$\omega \simeq \frac{2\mu_B B}{\hbar}\ , \tag{3.3}$$

where $\mu_B = 5.79 \times 10^{-11}$ MeV/T is the Bohr magneton. With a precise calculation of the time the particle spends in the magnet, it is possible to obtain the

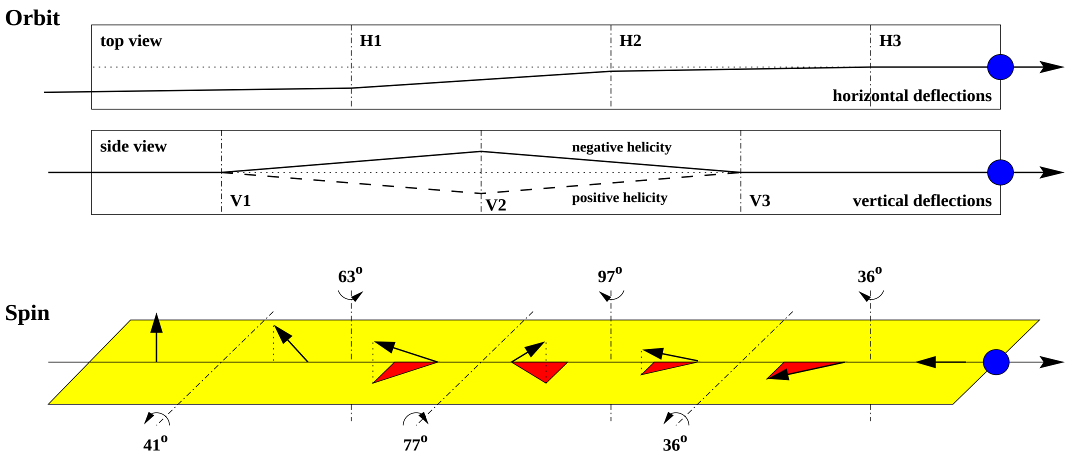

Figure 3.2: Schematic diagram of the HERA spin rotators [15]. A series of carefully tuned horizontal and vertical magnetic fields change the spin direction of the transversely polarised positrons so that they leave the spin rotator longitudinally polarised. The Lorentz force deflects the positron while it is in the magnetic field. The net result of a series of deflections is a small horizontal displacement. Figure copied from [16].

desired direction of spin within the quantum mechanical uncertainty. To reduce the uncertainty, multistage devices are used. A schematic diagram of the spin rotator operation is shown in Fig. 3.2.

Beam positrons are injected into the ring in discrete *bunches*, such that at any given time, the entire HERA ring can be subdivided into 220 bunches, with the time interval between the consecutive bunches of 96 ns. Of these, only 189 bunches are filled with positrons, forming 3 *trains* with 63 bunches in each train (Fig. 3.3). Trains are separated from one another by 7 empty bunches, with the exception of additional empty bunches between the 3rd and 1st trains. The beam current decreases with time as beam particles are depleted. The average start and stop beam currents are about 40 mA and 10 mA, respectively. Useful beam fill durations are typically 10 hr.

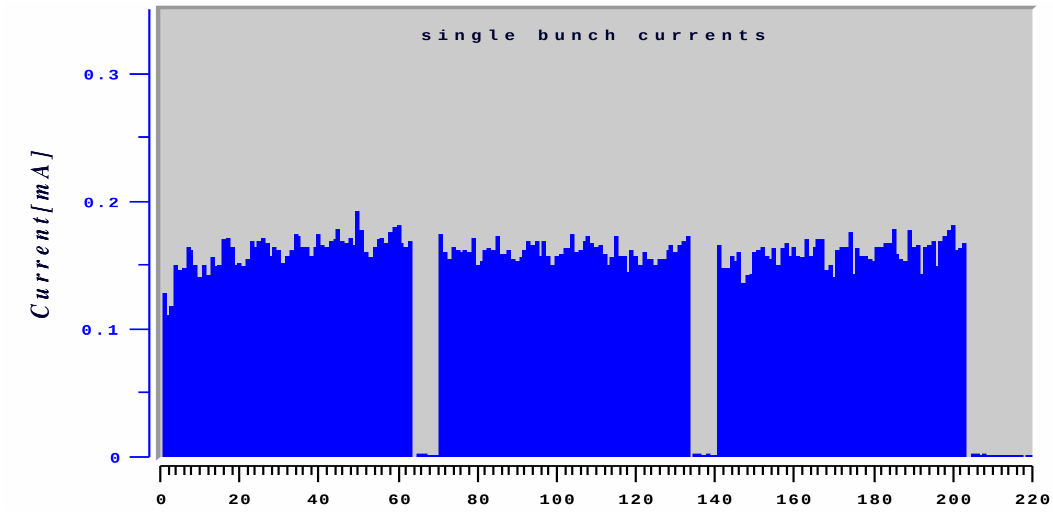

Figure 3.3: Bunch structure of the positron beam. This is a screen capture of the bunch current monitor in HERMES control room. Figure copied from [18].

3.2 Beam Polarimetry at HERA

Monitoring of the beam polarisation is vital to the operation of the experiment. Both longitudinal and transverse polarisations are measured near the East and West Halls, respectively.

The design of the longitudinal polarimeter is based on the Compton scattering of circularly polarised photons on the longitudinally polarised beam. With fixed energies, the polarised Compton cross section depends on the longitudinal polarisation of the positron [19]:

$$\frac{d\sigma}{dE_\gamma} = \frac{d\sigma_0}{dE_\gamma}[1 - P_\lambda P_e A_z(E_\gamma)] \ , \tag{3.4}$$

where $d\sigma_0/dE_\gamma$ is the unpolarised cross section, E_γ is the energy of the backscattered Compton photon, P_λ is the circular polarisation for the two helicity states $\lambda = \pm 1$, P_e is the longitudinal positron polarisation, and $A_z(E_\gamma)$ is the longitudinal asymmetry function. With the values of $d\sigma_0/dE_\gamma$ and $A_z(E_\gamma)$ well-known, and with P_λ and E_γ fixed, $d\sigma/dE_\gamma$ is a function of longitudinal polarisation only.

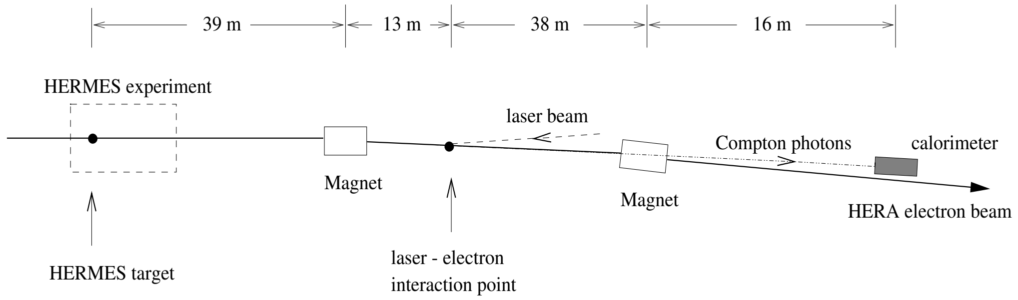

Figure 3.4: Schematic drawing of HERA longitudinal polarimeter. Figure copied from [19].

The principle is implemented in the HERA longitudinal polarimeter (Fig. 3.4) which uses a pulsed Nd:YAG laser [20]. The laser produces linearly polarised 532 nm light, which corresponds to $E_\gamma = 2.33$ eV. The linear polarisation of the light is converted into circular polarisation by a device known as a Pockels cell. The laser produces very powerful 3 nm long pulses with pulse energies between 1 and 250 mJ. Backscattered Compton photons are collected by a $\mathrm{NaBi(WO_4)_2}$ calorimeter. The polarisation is determined from the spin-dependence of the energy spectrum of the Compton photons.

A similar principle is incorporated into the design of the transverse polarimeter: circularly polarised laser light is irradiated into the positron beam and the backscattered Compton photons are detected in a pair of calorimeters located above and below the beam plane. Unlike the longitudinal polarimeter, the transverse polarimeter uses continuous laser beam from a 25 W argon ion laser which radiates a 514.5 mm (2.41 eV) beam [21]. The calorimeter is built from 12 layers of tungsten sheets and scintillators. The polarisation is determined from the spacial dependence of the backscattered photons.

3.3 The Hydrogen Target

The gaseous hydrogen target is capable of operation in unpolarised and polarised regimes. The former is characterised by much higher density. The target is characterised by continuous flow of ^{1}H gas into the target storage cell centered about the beam axis (Fig. 3.5). All events of interest occur within the storage cell. In order to reduce mobility of the gas particles and therefore to increase the time they spend within the cell, the gas is cooled to $\sim 100\ K$. The excess gas is pumped out on both open ends of the cell, which results in the target density being highest at the centre of the storage cell, near the injection point. The delicate target structure is protected against synchrotron radiation by movable collimators.

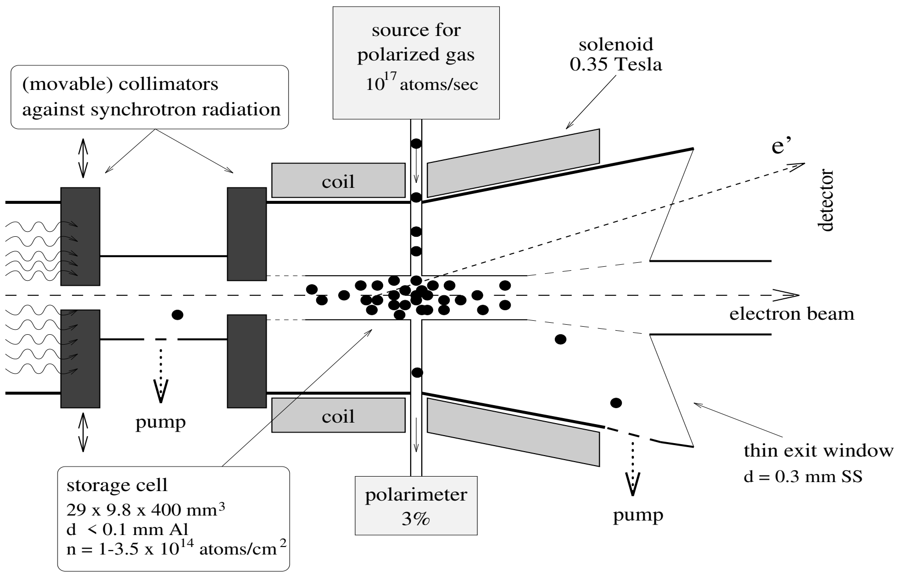

Figure 3.5: Diagram of HERMES target.

In the case of a polarised target run, the chemical bonds of the H_2 molecule are first dissociated by means of the *Atomic Beam Source* (ABS), which breaks up the molecules by means of a weak radiofrequency electric discharge. Of the dissociated hydrogen atoms, those in spin state $+\frac{1}{2}$ are selected and those in

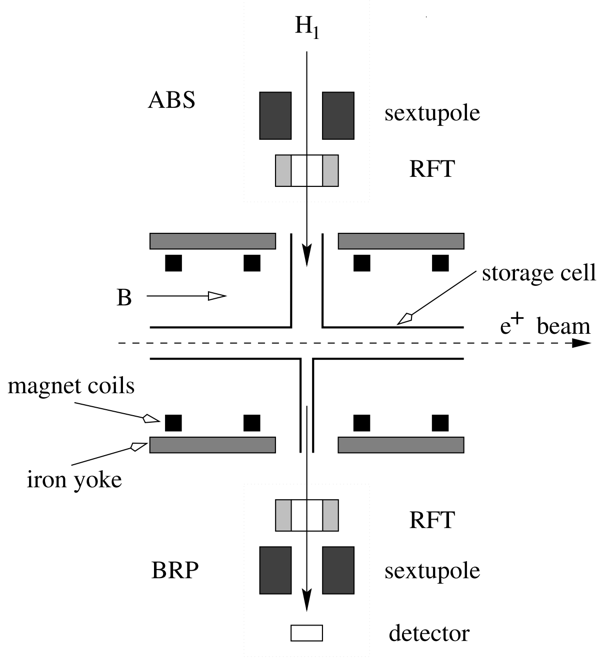

Figure 3.6: Schematic diagram of hydrogen target with ABS and BRP. Figure copied from [22].

spin state $-\frac{1}{2}$ are rejected by means of Stern-Gerlach separation [23] performed by a sextupole magnet. The *Radio Frequency Transition* (RFT) (Fig. 3.6) units transfer the polarisation from the electron spin to the nuclear spin and the polarised atoms are ballistically injected into the storage cell so that their spins are aligned/antialigned with the beam's helicity. The polarisation within the cell is sustained by the superconducting magnet and measured with the *Breit-Rabi Polarimeter* (BRP). The target polarisation is periodically flipped by a laser beam, so that parallel and antiparallel configurations of target and beam polarisation are alternately obtained. Target density is highest at the centre of the storage cell, near the injection point.

In the case of an unpolarised target run, the H_2 molecules are injected directly into the target chamber by means of the *Unpolarised Gas Feed System* (UGFS).

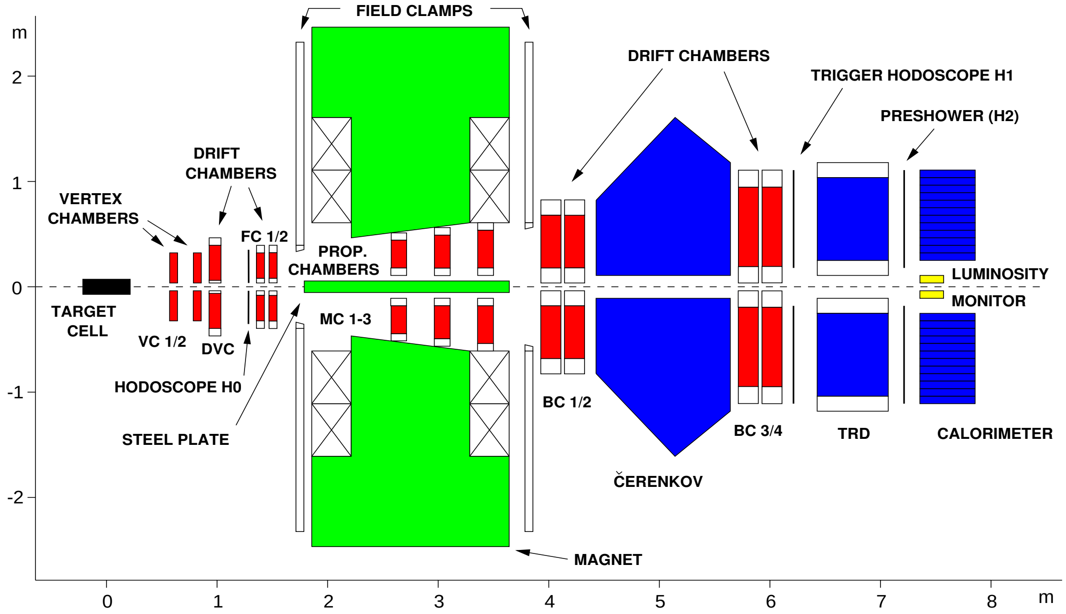

Figure 3.7: The HERMES spectrometer.

Because of higher target density, unpolarised operation is characterised by higher event rate.

3.4 Overview of the HERMES Spectrometer

3.4.1 Overview

The HERMES spectrometer is shown in Fig. 3.7. The positrons are incident on the target from the left. The angular acceptance of the detector, limited by the aperture of the magnet and the beam pipe, is $40 - 140$ mr vertically and $0 - 170$ mr horizontally. After the beam positrons collide with the target nucleons, the produced particles pass through detectors, which are used to track the particles and determine their types and four-momenta. All detectors within the HERMES spectrometer consist of physically separate top and bottom halves, with the beam pipe passing through the middle (Fig. 3.7). The momenta of the tracks are determined from the extent of deflection from their original trajectories as the particles traverse the 1.5 T·m magnet: the greater the momentum, the smaller the deflection.

Selection of a ρ^0 event involves detection of three tracks: the scattered positron e^+ and a pair of the daughter pions $\pi^+\pi^-$ in all tracking detectors. e^+, π^+ and π^- are clearly identified in the PID detectors. The precise vertex and track reconstruction involves all the tracking chambers.

3.4.2 Tracking Detectors

The tracking of particles is performed by wire chambers, each of which reacts to the passage of particles through one of its channels with an electrical signal.

The wire chambers are high voltage devices with an array of wires strung within each chamber. An electric field is formed within the chamber as a result of the potential difference between the anode wires and cathode planes. Passage of particles through the gaseous medium between the wires ionises the gas; the ionised particles create electric signals within the neighboring wires. The wire chambers contain many wires, usually with at least two wire planes, where wires in one plane are strung at an angle to the other, forming a grid. The location of the particle within the chamber is then established by the presence of an electric signal from two (or more) wires in different planes. Based on the mechanism of the electric field distortion, several types of wire chambers exist. At HERMES, *proportional* and the *drift* chambers are used. Detailed description is available in reference [24].

In proportional chambers, a particle that enters the chamber ionises the gas mixture within the chamber. The resulting free charges drift to the oppositely charged electrodes: the electrons to the anodes, the positive ions to the cathodes. When very near the destination wires, the drifting electrons are accelerated by the intense electric field. The accelerated electrons ionise the medium around them, the ionisation yields even more drifting electrons that also ionise the surrounding gas; the passage of a charged particle through the chamber causes an avalanche of ionisation. In a proportional chamber, the rate of multiplication, and therefore the net current, is proportional to the energy deposited by the charged particle. At HERMES, the proportional chambers are the Magnet Chambers (MC) located inside the magnet.

In drift chambers, a particle that enters the chamber also ionises the gas mixture. Unlike in the proportional chambers, the total electron drift time within the chamber is used to locate the particle track. Measurement of the drift time within the chamber allows to determine the distance to the wire, provided the speed is constant. Most wire chambers at HERMES are of the drift type: the Drift Vertex Chamber (DVC) and a pair of Front Chambers (FC) in front of the magnet, and four Back Chambers (BC) behind the magnet.

For some time in 1997, the Vertex Chambers (VC) were also installed. These chambers are of the recently developed Microstrip Gas Counter type. In this analysis, the VCs were not used in the event reconstruction. More information on the VCs is available in [25].

3.4.3 The Trigger Hodoscopes

The trigger is an electric signal supplied to the Data Acquisition System when an event of interest occurs in the detector. Arrays of scintillators, called *hodoscopes* are used for triggering. An array of relatively narrow scintillators provides a fast-responding detector. Scintillation is a process of light emission in a medium caused by the passage of a particle. At HERMES energies, the intensity of light depends linearly on the energy deposited.

The optical response in each scintillator within a hodoscope is transformed into electric signal by a PhotoMultiplier Tube (PMT) (see [24] for description). The anode current of the PMTs depends linearly on the light intensity at the photocathode.

Three hodoscopes, H0, H1 and H2 (the *preshower* detector), were used in 1996 and 1997. H2 is used as a Particle Identification (PID) detector (see the next section).

3.4.4 Particle Identification Detectors

Positron-hadron differentiation is the main goal of particle identification at HERMES. The four PID components of the apparatus, the Čerenkov detector, the Transition Radiation Detector (TRD), the Preshower detector (H2) and the electromagnetic Calorimeter, are able to differentiate between positrons and hadrons with varying effectiveness. The quality of the differentiation is greatly enhanced by the combination of all four detectors (see Section 3.4.5).

The Threshold Čerenkov Detector

Čerenkov radiation is emitted in a medium by particles whose velocities exceed the speed of light in the medium. For optical density (index of refraction) n, the *threshold function* is given by [26]

$$N_0 = C_0 \left(1 - \frac{1}{(n\beta)^2} \right) \ , \tag{3.5}$$

where C_0 is a constant. β is defined for a particle i with rest mass M_i as

$$\beta_i = \frac{v_i}{c} = \frac{p_i}{E_i} = \frac{p_i}{\sqrt{M_i^2 + p_i^2}}. \tag{3.6}$$

With background noise subtracted, N_0 is equal to the number of Čerenkov photoelectrons. Because the mass of the positron is much smaller than that of the pion, the lightest hadron, $(1 - 1/\beta^2)$ is much larger for positrons. For n very close

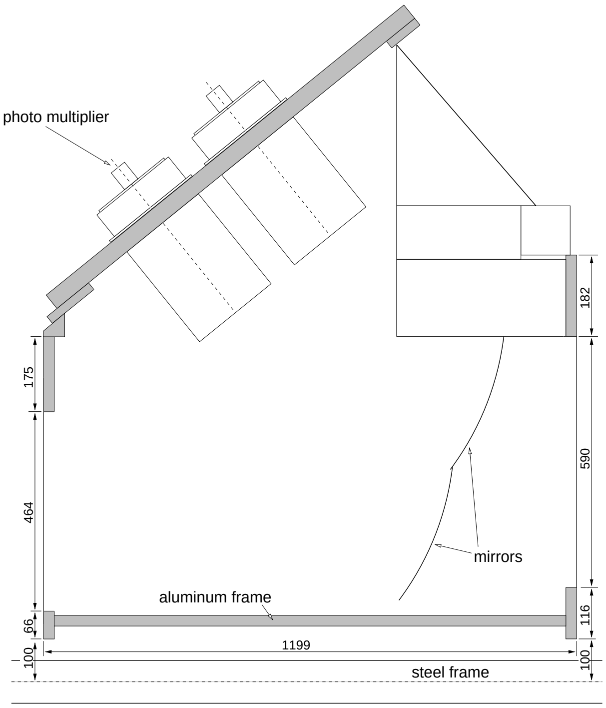

Figure 3.8: Side cross-section of the top half of the Čerenkov detector. The lower half is identical to the upper half. Figure copied from [26].

to 1, this implies that the yield depends appreciably on mass. For a given n, it is possible to compute the threshold momentum above which the particle emits Čerenkov radiation. The values of threshold momentum for the positron and the pion define the lower and upper bounds of operational momentum range, respectively. Within the operational range, such that separation between positrons and hadrons is possible, only positrons emit Čerenkov radiation.

The Čerenkov detector, used at HERMES in 1996 and 1997 (Fig. 3.8), contained a mixture of 30% C_4F_{10} and 70% N_2 gases at atmospheric pressure. The index of refraction for the mixture was $n = 1.0066181$. The resulting operational momentum range is $0.014 - 3.9$ GeV. In addition, pion-kaon separation and kaon-proton separation is also possible, for momentum ranges of $3.9 - 13.6$ GeV and $13.6 - 25.8$ GeV, respectively. Separation between positrons and hadrons in the

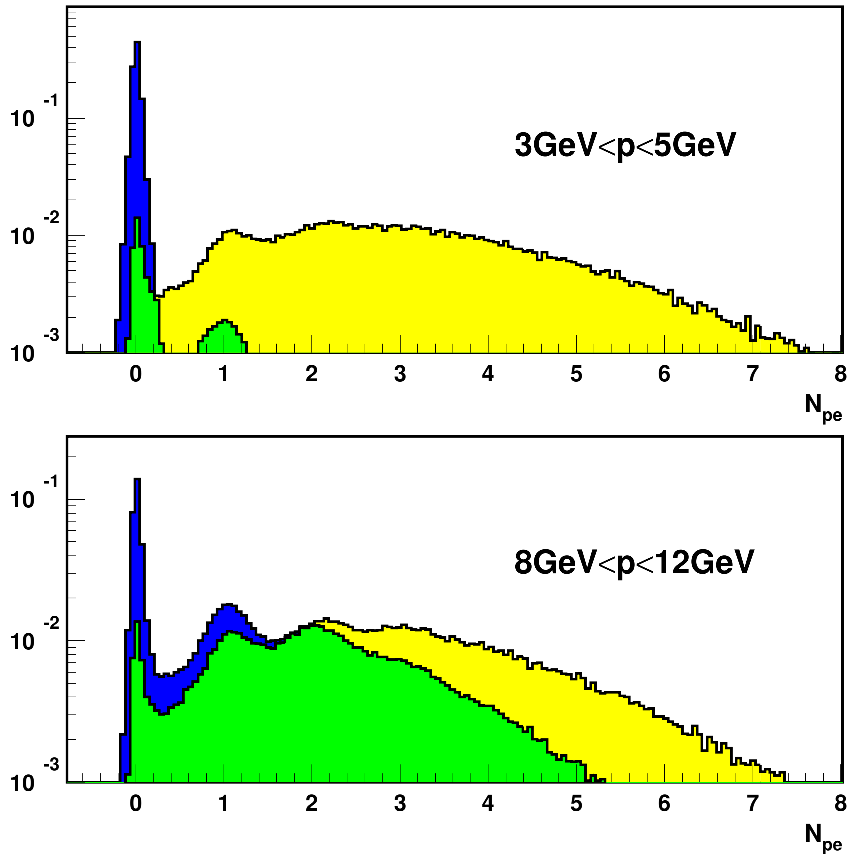

Figure 3.9: Photoelectron response of the Čerenkov detector below and above the pion threshold. Light and dark shadings represent positron and hadron distributions, respectively; the intermediate shading represents the region where the two distributions overlap. Good positron-hadron separation exists only below the threshold. Figure copied from [27].

Čerenkov detector is illustrated in Fig. 3.9.

The Transition Radiation Detector

Transition radiation (TR) is emitted by charged particles that cross a boundary between two media with different dielectric constants. Usually TR belongs to the X-ray region of the electromagnetic spectrum. The probability for a particle to emit a photon per interface is approximately $\frac{2}{3}\alpha$, where $\alpha = 1/137$ is the fine structure constant. In the ultrarelativistic regime, the mean energy W of the emitted TR caused by passage of a particle i from vacuum into a medium with plasma frequency ω_p depends linearly on $\gamma = E_i/M_i$ [28]

$$W = \frac{2}{3}\alpha\omega_p\gamma \ . \tag{3.7}$$

The plasma frequency in a material is a function of its electron density n_e:

$$\omega_p = 4\pi\alpha\frac{n_e}{M_e} \ , \tag{3.8}$$

where M_e is the rest mass of the electron. Since γ is much higher for positrons than for hadrons, the dependence of the TR energy yield on γ is a useful property for differentiating between positrons and hadrons.

From (3.7) and (3.8), it follows that the optimal radiator material should have high electron density. In order to increase the probability of TR emission in the HERMES TR Detector (TRD), multiple boundaries are necessary. The material should also be highly transparent to the X-rays. The three requirements are accomplished by use of a polypropylene fibre radiator. The choices of fibre thickness (17-20 μm) and packing density (0.10 g/cm^3) of this porous material are optimised for the electron energy range of the experiment [25]. The bulk thickness of the radiator is limited by the X-ray absorption, and is chosen to be 6.5 cm.

Apart from the radiator, the HERMES TRD contains an X-ray detector, which is a planar proportional wire chamber. For best X-ray absorption, a high-Z gas is required. Accordingly, the wire chamber is filled with a mixture of 90% Xe and 10% CH_4. CH_4 is used as a quenching agent to control the electron multiplication in the chamber. The gas mixture is recirculated in a closed loop system.

A radiator and a wire chamber constitute one module of the TRD (Fig. 3.10). Each half of the detector consists of 6 such modules used in succession

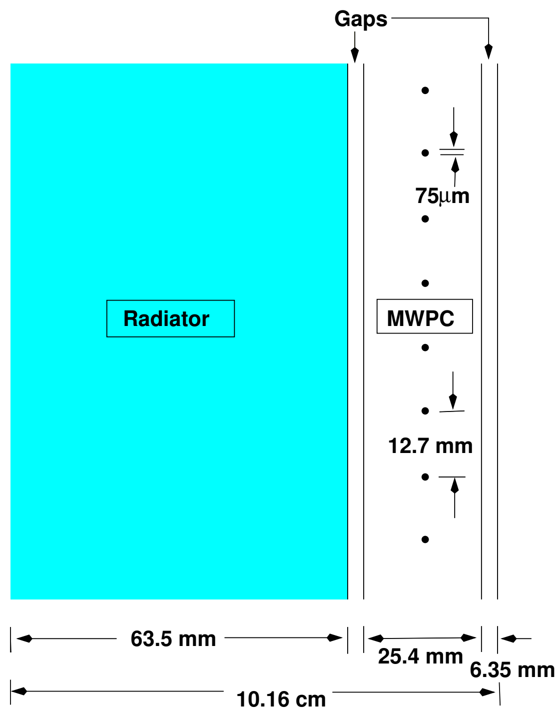

Figure 3.10: Schematic sideview diagram of one TRD module. Figure copied from [27].

(Fig. 3.11). When particles ionise the medium, secondary high-energy electrons are frequently produced. The latter, called the δ-rays, constitute the background to the TRD signal. Use of several modules in succession permits a module-by-module comparison of energy deposition, which allows elimination of the majority of δ-rays. A truncated mean method may be used for illustration may be used for illustration: since δ-rays are characterised by high energy deposition, the module with the highest energy deposition is excluded from the calculation of the mean value of energy deposition for each hit. As illustrated in Fig. 3.12, use of the 6 modules and the truncated mean method improves the positron-hadron separation. An even better method of the separation is discussed in Section 3.4.5.

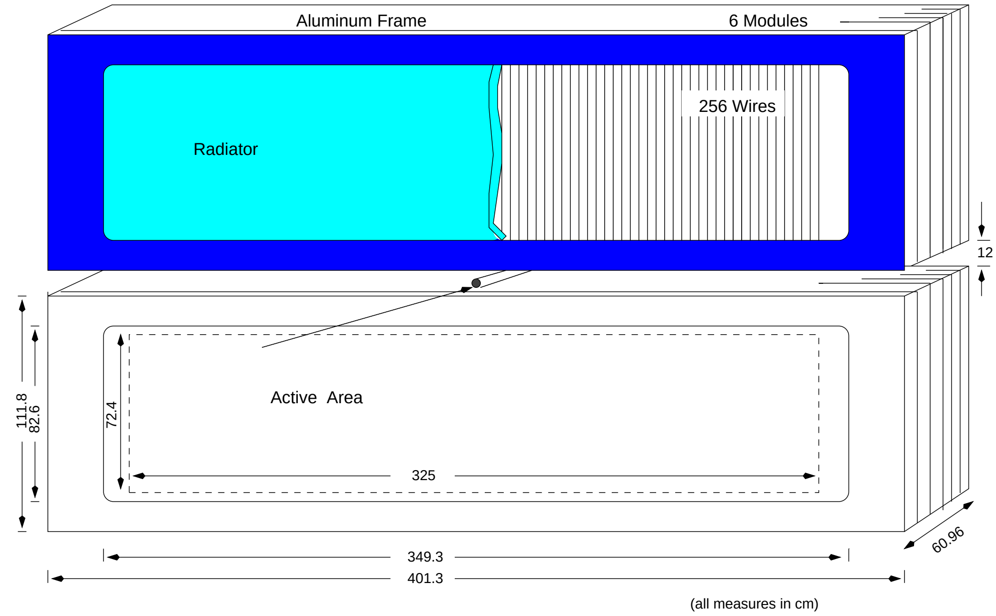

Figure 3.11: Schematic view of the TRD. Figure copied from [27].

The Preshower Detector

Energy loss per unit thickness dE/dz is significantly higher for positrons than for hadrons: in addition to collisions with electrons of the materials, a significant portion of energy is lost through radiation [24]. At HERMES energies, where the radiative energy loss dominates, the radiated photons are sufficiently energetic to produce e^+e^- pairs. These also radiate, with subsequent pair production. Rapid multiplication of the number of electrons and positrons occurs, and an electromagnetic shower is produced. With a sufficiently thick material of high Z, it is possible to use the high dE/dz for positrons to initiate an electromagnetic shower. This principle is used in the preshower detector (Fig. 3.13), which is made up of 42 plastic scintillators.

A 11 mm-thick plate of lead, placed immediately before the hodoscope H2, is 2 radiation lengths thick, i.e. the original positron would retain, on average, only $1/e^2$ of its initial energy as it leaves the plate. The remaining energy is

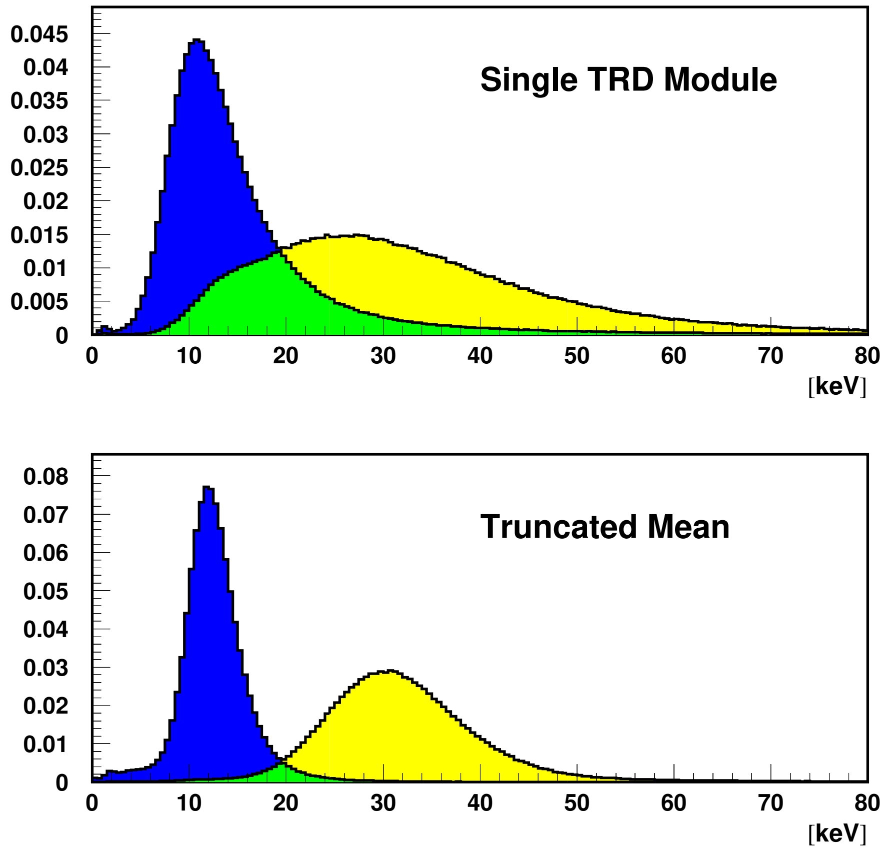

Figure 3.12: Response of the TRD detector for a single module and with the truncated mean. Light and dark shadings represent positron and hadron distributions, respectively; the intermediate shading represents the region where the two distributions overlap. Figure copied from [27].

contained in the electromagnetic shower, which propagates to the scintillators of the hodoscope. With such design, a parent positron registers a large net multiparticle signal from the shower in the hodoscope, whereas a hadron leaves the lead plate without producing a shower and registers a single particle signal of smaller magnitude. The response of the preshower detector is illustrated in Fig. 3.14.

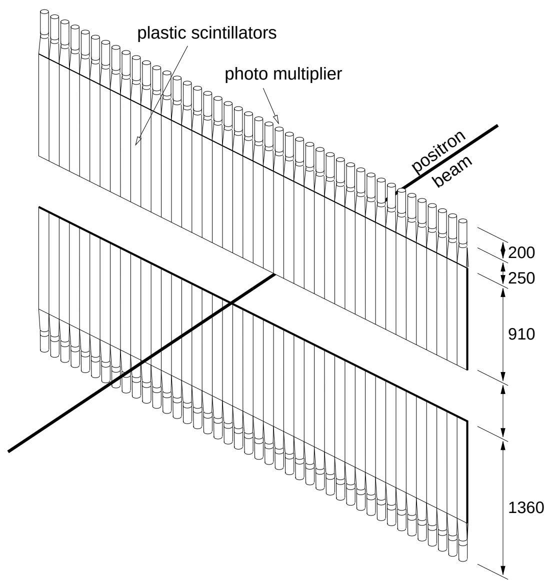

Figure 3.13: Schematic diagram of the preshower detector.

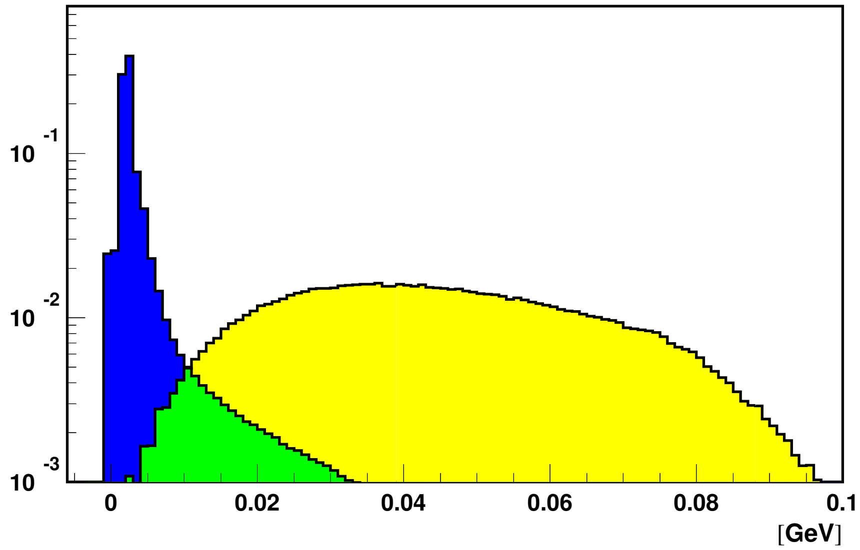

Figure 3.14: Normalised response of the preshower detector. Light and dark shadings represent positron and hadron distributions, respectively; the intermediate shading represents the region where the two distributions overlap. Figure copied from [27].

The Electromagnetic Calorimeter

The HERMES electromagnetic calorimeter, constructed of lead glass blocks, is able to fully contain an electromagnetic shower: with a sufficiently thick calorimeter, the shower is able to progress until all electrons and positrons are of such low energy that they do not radiate, but interact through ionisation of atoms which eventually causes them to stop. Therefore, for positrons at HERMES energies, $E_{calo}/p \simeq 1$, where E_{calo} is the energy deposition in the calorimeter, and p is the momentum of the positron measured by analysing the degree of track deflection by the magnet.

The behaviour of hadrons within the calorimeter is different, since they lose energy through ionising atomic collisions and through nuclear interactions only. The hadrons may still produce other particles as a result of collisions within the material, which may result in further hadron production and emission of photons. The photons and neutral pions create e^+e^- pairs, and electromagnetic cascades result. The entire process of multiple particle creation as a result of interaction of hadrons with matter, known as the hadronic shower, does not start immediately in the calorimeter and is most often not fully contained within the calorimeter. Due to loss of neutrons and nuclear binding energy $E_{calo}/p < 1$ for hadrons.

The different behaviour of positrons and hadrons in E_{calo}/p in the calorimeter allows a good degree of separation between the two types of particles (Fig. 3.15). The HERMES calorimeter (Fig. 3.16) contains 420 cells in each half of the detector. The cells, square in cross section, are constructed from a glass made of 51.23% Pb_3O_4, 41.53% SiO_2, 7.0% K_2O, and 0.2% Ce in weight proportions, with a radiation length of 2.78 cm and index of refraction of 1.65 [29]. With cell dimensions of $9 \times 9 \times 50$ cm, each cell is 18 radiation lengths thick. As the shower is quenched in the cells, particles emit Čerenkov radiation, which is detected by the photomultiplier tubes. Each cell is coupled to a photomultiplier tube, thus

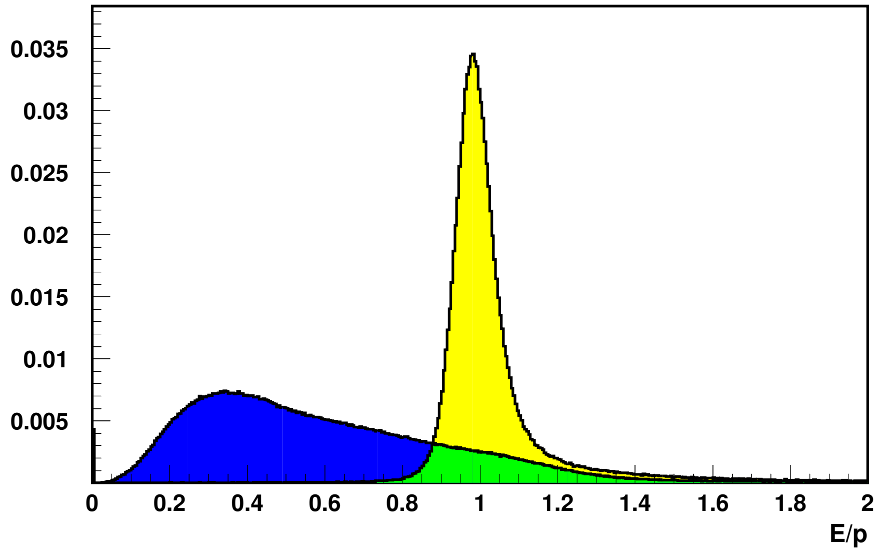

Figure 3.15: Normalised response of the calorimeter. Light and dark shadings represent positron and hadron distributions, respectively; the intermediate shading represents the region where the two distributions overlap. Figure copied from [27].

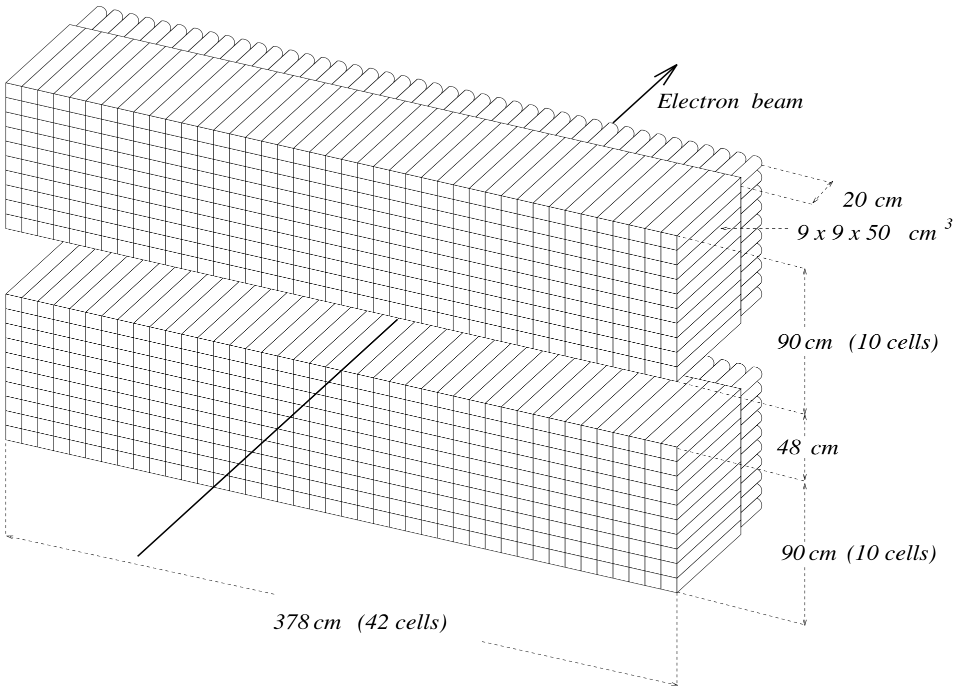

Figure 3.16: Schematic drawing of HERMES electromagnetic calorimeter.

forming a total of 840 channels. Since showers may extend over adjacent cells, measurements are summed over a 3×3 block array with the centre of the shower in the middle.

3.4.5 Particle Identification Procedure at HERMES

The presence of a particle in a detector induces a signal within it. Depending on the nature of the particle, the detector response varies. In order to identify a particle as a positron, a pion, or any other particle, the Particle IDentification (PID) procedure, based on the difference in response for leptons and hadrons by the four PID detectors, has been devised.

The response of the four PID detectors is shown in Fig. 3.17. When a particle is detected by a certain detector, a probability of the particle being either a lepton or a hadron is assessed. The value of the probability depends on energy and other kinematic parameters of the particle. Mathematically, this is described in terms of the quantity $PID^{detector}$:

$$PID^{\mathsf{detector}} = \mathbf{log_{10}} \frac{\mathcal{L}_e^{\mathsf{detector}}}{\mathcal{L}_h^{\mathsf{detector}}} \ . \tag{3.9}$$

The quantities $\mathcal{L}_{\mathsf{particle}}^{\mathsf{detector}}$ in (3.9) represent the *conditional probabilities* that a particle registered by a certain detector was a positron (e) or a hadron (h). The term "conditional probability" refers to the fact that it is normalised so that $\mathcal{L}_{\mathsf{e}}^{\mathsf{detector}} + \mathcal{L}_{\mathsf{h}}^{\mathsf{detector}} = 1$. Any PID below 0 is an indication of a hadron, while any PID above 0 is an indication of a positron. Detailed information on the probability calculations is available in [30] and [10].

The reliability of PID assessment increases if several independent calculations are combined. Accordingly, the following quantities are defined:

$$PID3 = \mathbf{log_{10}} \left(\frac{\mathcal{L}_e^{Pre} \mathcal{L}_e^{Cal} \mathcal{L}_e^{\check{C}er}}{\mathcal{L}_h^{Pre} \mathcal{L}_h^{Cal} \mathcal{L}_h^{\check{C}er}} \right) \tag{3.10}$$

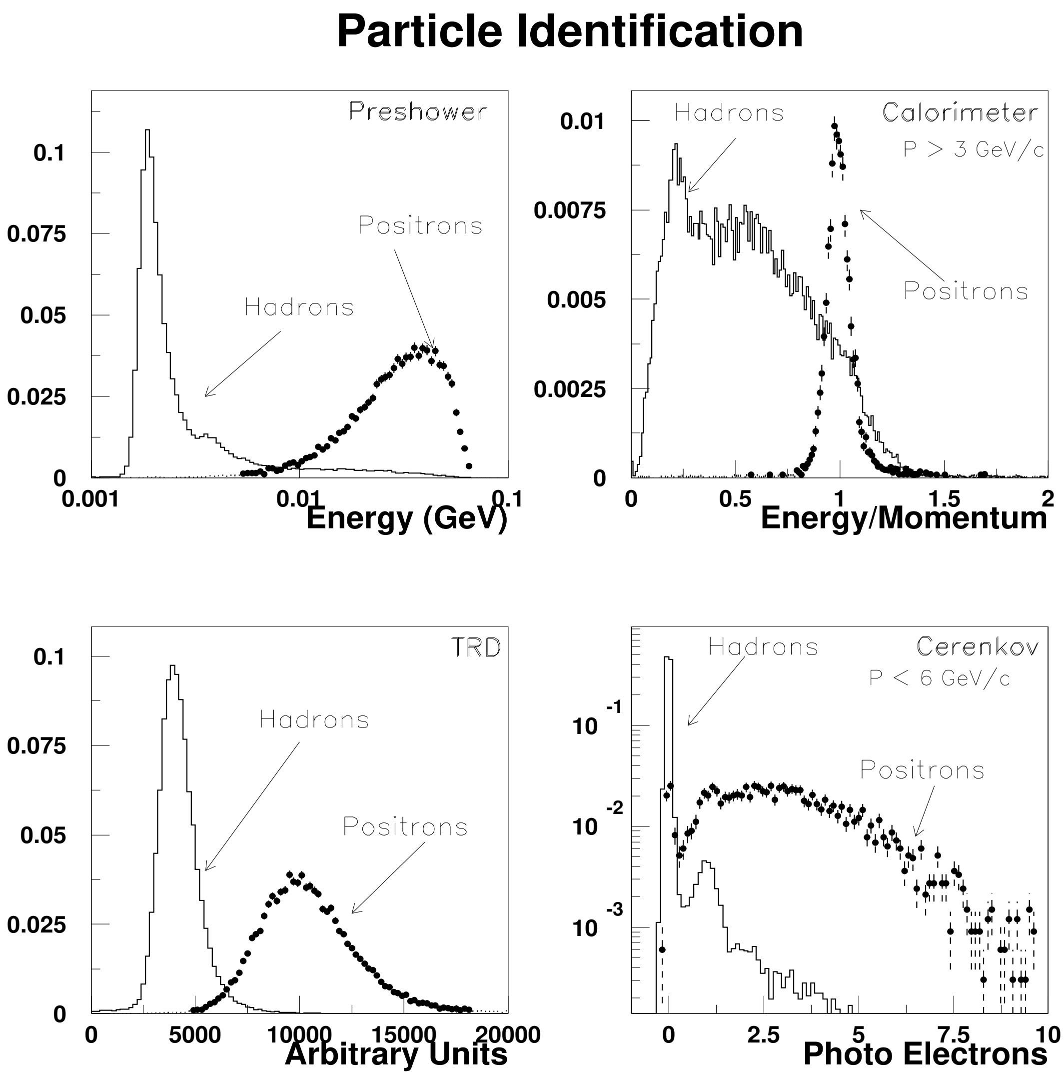

Figure 3.17: Responses of the PID Detectors. The vertical axes represent the normalised numbers of counts in a detector such that the sum of the numbers of counts in all bins for positrons and hadrons is 1.

and

$$PID5 = \mathbf{log_{10}} \left(\prod_{i=1}^{6} \frac{\mathcal{L}_{e_i}^{TRD}}{\mathcal{L}_{h_i}^{TRD}} \right) = \sum_{i=1}^{6} (PID5)_i \ . \tag{3.11}$$

In the case of *PID5*, the PID is calculated in each of the 6 TRD modules i, and then combined. $PID5$, also called PID_{TRD}, provides a better positron-hadron

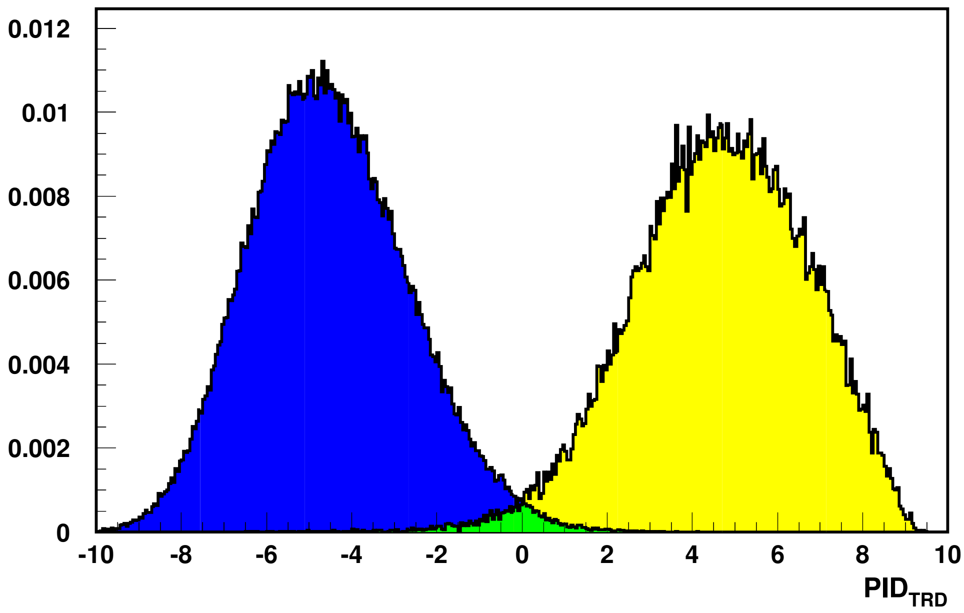

Figure 3.18: PID_{TRD} spectrum. The figure illustrates an improved positron-hadron separation. Light and dark shadings represent positron and hadron distributions, respectively; the intermediate shading represents the region where the two distributions overlap. Figure copied from [27].

differentiation than the truncated mean method, and therefore is used in the analysis (Table 3.18). The final assessment of the particle type is performed as follows: the particle is considered a positron if

$$PID3 + PID5 > 0 \; ; \tag{3.12}$$

or a hadron if

$$PID3 + PID5 < 0 \; . \tag{3.13}$$

3.4.6 The Luminosity Monitor

The luminosity is a characteristic quantity which represents the product of the beam flux and the surface target density. At HERMES, the luminosity is mea-

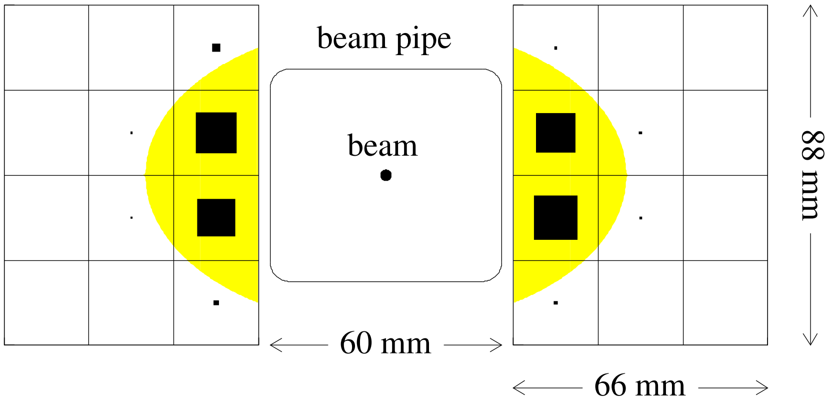

Figure 3.19: Front view of the luminosity monitor with the shaded region showing the detector acceptance.

sured by means of the luminosity monitor [31] (Fig. 3.19), a calorimeter made of 24 radiation-hard $NaBi(WO_4)_2$ crystal blocks, with each block coupled to a photomultiplier tube. Since it is impossible to place a detector directly into the beam, the luminosity is measured indirectly by assessing the rates of Bhabha scattering $e^+e^- \rightarrow e^+e^-$ from the atomic electrons in the target gas, which is related to the beam luminosity through

$$R = L\sigma \ , \tag{3.14}$$

where L, R and σ denote the luminosity, the process rate and the Bhabha cross section, respectively. The luminosity is related to the beam current I and the surface density of the target ρ through

$$L = \frac{I\rho}{e} \ , \tag{3.15}$$

where e is the elementary charge.

The acceptance of the detector is limited by the beam pipe, which is widened

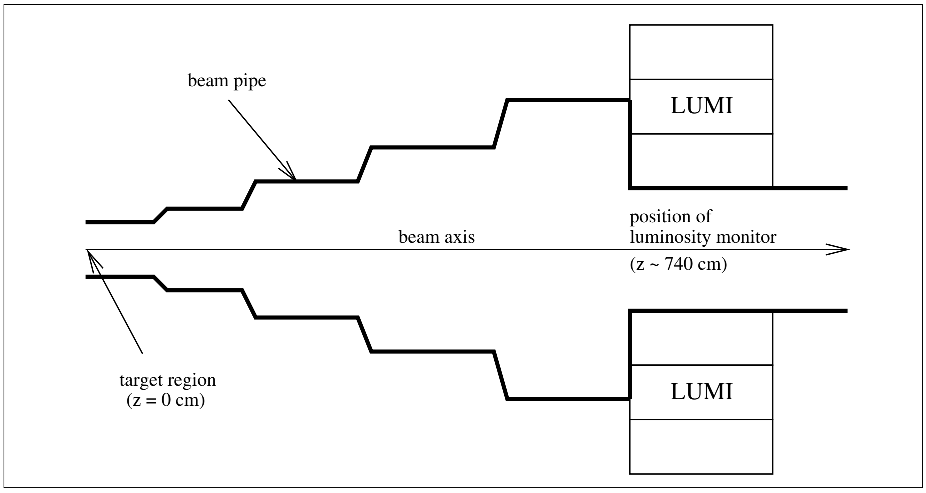

Figure 3.20: Schematic side view of the luminosity monitor and the beam pipe configuration. Figure copied from [32].

in 4 stages from the target to the luminosity monitor) and then narrowed so that it passes through the detector (Fig. 3.20).

3.5 The Trigger

Since it is necessary to establish that the event originates in the target and to ensure that particles in the final state traverse the magnet gap, detectors are used in various combinations with each other. A coincidence of signals, corrected for time of travel between the detectors and time of the detector response, is used to generate a *gate*: a logical pulse of a certain duration during which the DAQ records the detector responses.

The main trigger at HERMES is the DIS trigger which is activated when a positron is scattered into either the top or the bottom half of the detector and is detected in the hodoscopes H0, H1, H2 and the calorimeter (Fig. 3.21). For data analysis and equipment monitoring, a variety of other triggers is generated.

For the purposes of noise discrimination and correct measurements, signal

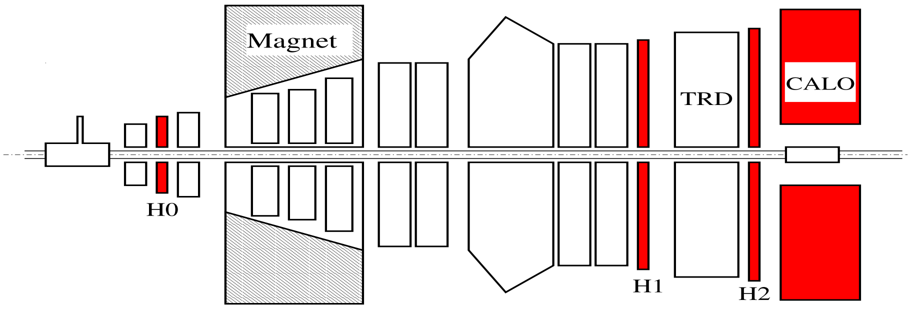

Figure 3.21: DIS trigger in 1996 and 1997. Detectors required in the coincidence are shaded.

thresholds are established for each involved detector. For the DIS trigger, one of such threshold requirements is the energy deposition in the calorimeter of > 3.5 GeVor > 1.5 GeV the unpolarised and polarised target operation, respectively.

Chapter 4

The Monte Carlo Programs

The principle of the Monte Carlo method of simulation "lies in the random sampling of the most probable outcomes" [33] of a particular physical process. A distribution of some physical quantity is probed at different locations in a random order; as a result, the Monte Carlo creates simulated replicas of physical events that follow the given distribution. Because of the randomness of the sampling, the Monte Carlo simulation method correctly creates a sample of events that follow a well-known model. Naturally, the greater the number of events, the better the simulated event distribution follows the model.

In this analysis, the Monte Carlo simulation is used in the assessment of the DIS background contribution and in the creation of a diffractive ρ^0 spectrum. This chapter briefly describes the Monte Carlo programs used.

4.1 The Structure of the HERMES Monte Carlo (HMC) Program

The HMC simulation process consists of a *physics generator* which generates the final states of the particles as they leave the target nucleus, and a *tracking* *procedure* which simulates the detector response as the particles pass through the apparatus. The end result of an HMC simulation of an event is a set of kinematic variables that the detectors would register if real particles from that event passed through them. In order to obtain a complete kinematic picture of an event, the detector response is analysed with the HERMES ReConstruction (HRC) program, which reconstructs the tracks that cause such a response in the detectors. In this way, the simulation procedure fully mimics the real data acquisition process.

Regardless of the type of physics generator, the tracking process is the same. The tracking of particles through the detectors is simulated with the GEANT software [34]. GEANT contains databases that contain full information about the detectors' geometry, materials, triggers, and sensitivities to various particles. The kinematic restrictions of the detector acceptance, such as the threshold values of the signal, are also incorporated. In addition, GEANT is able to determine how the detector material affects the four-momentum of the particles that pass through it. This makes it possible to simulate the detector response completely.

4.2 The DIS Monte Carlo Generator

The fact that both the target nucleus and the beam positron may be polarised is incorporated into the Polarized Electron-Proton Scattering Interactions (PEPSI) software [35], which is the DIS physics generator used in HMC. PEPSI is based on the unpolarised DIS generator called LEPTO [36]. It incorporates the polarisation corrections to the unpolarised DIS cross section.

The interaction of the virtual photon γ^* with the target in the DIS process (Fig. 2.1) is considered to have contributions from the three primary subprocesses: the expulsion of quark from the nucleon $\gamma^* + q \to q$, the production of a gluon from the nucleon $\gamma^* + q \to q + g$, and the photon-gluon fusion into a $q\bar{q}$ pair

$\gamma^* + g \rightarrow q + \bar{q}$. In the first two cases, the photons may strike either a valence or a sea quark. In the case of photon-gluon fusion, the ratio of probabilities of creation of the 3 lightest quarks is [37]

$$d : u : s = 1 : 1 : \tfrac{1}{3} \ .$$

An example of a simulated DIS event is shown in Fig. 4.1

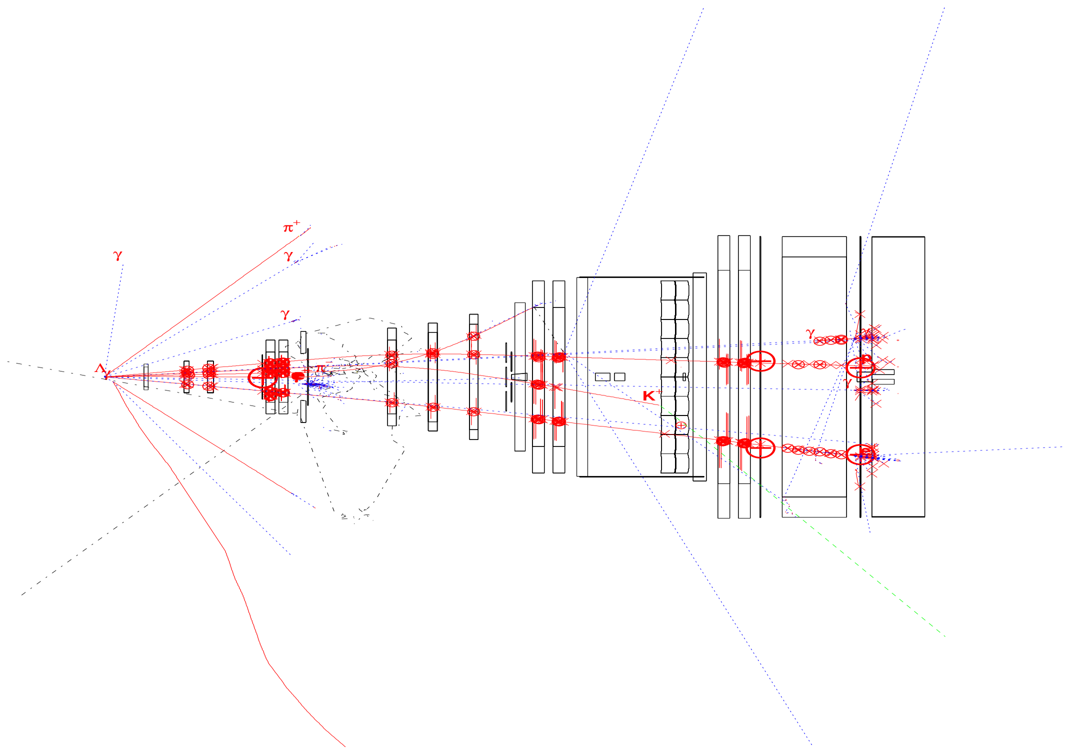

Figure 4.1: An example of a simulated DIS event in the HERMES detector (top view). The beam enters from the left and collides inelastically with the target, resulting in production of several primary particles, not all of which enter the detector. The secondary particles are produced through decay and interaction with the apparatus.

4.3 The Diffractive ρ^0 Monte Carlo

Simulation of the diffractive ρ^0 spectrum is also required in this analysis. The diffractive ρ^0 generator is a Monte Carlo program, often referred to as the Baby Monte Carlo (BMC). The output of the BMC, written to a computer file, is a set of momenta of scattered e^+ and of the $\pi^+\pi^-$pair, in the lab frame. These momenta are subsequently fed into the slightly modified HMC to simulate the detector response. The only difference with the standard version of HMC is that the modified HMC accepts events from the external generator (BMC) instead of from the internal DIS generator. The events processed by the HMC are reconstructed with the HRC to obtain the full information about the trajectories of particles that would result in such detector response. An example of a simulated diffractive ρ^0 event in HERMES detector is shown in Fig. 4.2.

In the BMC, the photoproduction cross section is simulated according to [10]

$$\sigma_0(Q^2) = \frac{1}{(1+Q^2/M_\rho^2)^2}\ \sigma(Q^2=0)\ , \tag{4.1}$$

where

$$\sigma(Q^2=0) = \frac{A_\gamma 2M_p}{W^2-M_p^2} + B_\gamma\ , \tag{4.2}$$

with $A = 29.4\ \mu\mathrm{b}\cdot\mathrm{GeV}$ and $B_\gamma = 9.5\ \mu$b. $M_p^2 = 0.938$ GeV and $M_\rho = 0.7699$ GeV^2. The events are produced according to

$$\frac{d\sigma}{dQ^2\ dE'\ d\phi} = \frac{1}{2EE'}\Gamma_T(Q^2,E')\sigma_0(Q^2) \tag{4.3}$$

with the photon flux factor

$$\Gamma_T(\cos\theta,\phi,E') = \frac{\alpha}{2\pi^2}\frac{W^2-M_p^2}{2M_p}\frac{1}{Q^2}\frac{E'}{E}\frac{1}{1-\epsilon}\ , \tag{4.4}$$

where $\alpha = 1/137$.

As a part of the BMC simulation, the invariant mass $M_{2\pi}$ distribution is produced according to the mass-skewed relativistic Breit-Wigner distribution

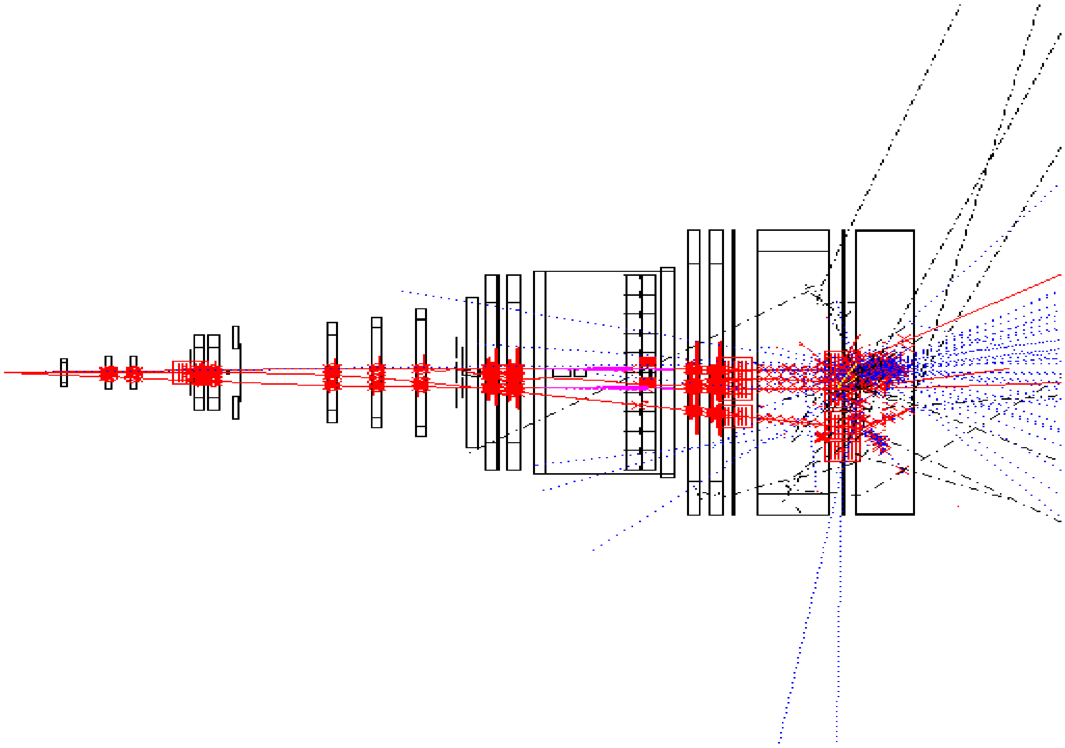

Figure 4.2: An example of a simulated diffractive ρ^0 event in the HERMES detector (top view). Three tracks emerge from the target.

function [38, 39]

$$F = \frac{2}{\pi} \frac{M_{2\pi} M_\rho \Gamma}{(M_{2\pi}^2 - M_\rho^2)^2 + M_\rho^2 \Gamma^2} \left(\frac{M_\rho}{M_{2\pi}} \right)^n , \tag{4.5}$$

where n denotes the *mass skewing factor* and

$$\Gamma = \Gamma_0 \left(\frac{q}{q_0} \right)^3 \frac{M_\rho}{M_{2\pi}} . \tag{4.6}$$

In the above equation, $\Gamma_0 = 0.1512$ GeV denotes the natural width of the ρ^0 peak, q and q_0 are given by

$$q = \frac{\sqrt{M_{2\pi}^2 - 4M_\pi^2}}{2} \tag{4.7}$$

and

$$q_0 = \frac{\sqrt{M_\rho^2 - 4M_\pi^2}}{2} . \tag{4.8}$$

The mass skewing factor n exhibits a Q^2 dependence, which, according to Ref. [39], is

$$n = (3.65 \pm 0.22) - (0.37 \pm 0.33)Q^2 \ , \tag{4.9}$$

for a range of 0.3 GeV $< Q^2 <$ 3 GeV. However, from the world data for n (Fig.

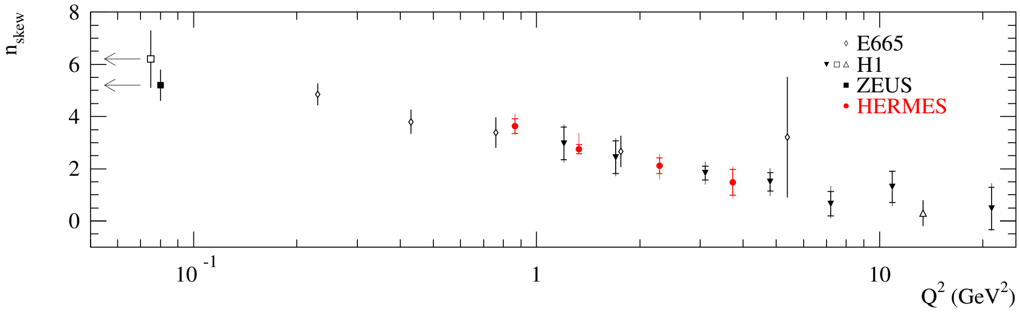

Figure 4.3: World data on the mass skewing factor n. Figure copied from [40].

4.3) over a much wider Q^2 range, n seems to decrease logarithmically with Q^2. In this analysis, the above mentioned world data plot, which has a logarithmic Q^2 axis, was used to plot a straight line through the world data by hand, whereupon an expression

$$n = (3.5 \pm 0.3) - (3.3 \pm 1.2) \log_{10} Q^2 \tag{4.10}$$

was obtained.

In this analysis, the Q^2 range is divided into four Q^2 bins (see the next chapter). The values of n calculated from (4.9) and (4.10) for the four $\langle Q^2 \rangle$ values are compared in Table 4.1. The above values agree with each other within the error. The values calculated with (4.10) were used, except as noted. The Q^2 ranges used in the experiment and their average values are given.

Q^2 Range	$\langle Q^2 \rangle$	from Eqn. (4.10)	from Eqn. (4.9)
$0.50 - 0.95$	0.8	3.82[1] $\pm$ 0.18	3.36 ± 0.34
$0.95 - 1.30$	1.1	3.4 ± 0.4	3.2 ± 0.4
$1.30 - 1.96$	1.6	2.8 ± 0.5	3.1 ± 0.5
$1.96 - 4.00$	2.6	2.1 ± 0.8	2.7 ± 0.9

Table 4.1: Comparison of the values of n with the two methods of calculation.

[1] For proper operation of the BMC software, n in bin Q1 was lowered to 3.70

Chapter 5

Analysis and Results

With the theoretical base of Chapter 2 and the description of the HERMES apparatus of Chapter 3 in mind, this chapter provides detailed description of the extraction of the Spin Density Matrix Elements (SDME) and presents the final results.

5.1 Overview of Analysis Procedure

In this age, data analysis in any particle experiment is largely computer-based, and HERMES is not an exception. From analysing the detector responses and reconstructing the actual physical events to obtaining final results of a specific analysis, computers are involved extensively. Primary analysis of detector responses and conversion of electromagnetic signals into physical quantities is performed on a common basis through the Data Acquisition system (DAQ). The events are then reconstructed by means of the HERMES ReConstruction program (HRC), which, by analysing the position and coincidences of events in the tracking chambers, reconstructs the full trajectories of the events. At the end, the events are written into compact files called Data Summary Tapes (DST). Because of their relatively small size, they are also referred to as the "microDST"s (uDST). uDSTs are available to all collaboration members who use them to process the data according to the nature of their analyses.

For convenience, the data-taking is divided into short *runs* which last a few minutes. In turn, the runs are subdivided, into *bursts* where each burst lasts about 10 s. Each run corresponds to one uDST file. The burst structure is preserved in the uDST file.

The process of extraction and analysis of the diffractive ρ^0 events is summarised in Fig. 5.1. The event files are analysed with the appropriate software.

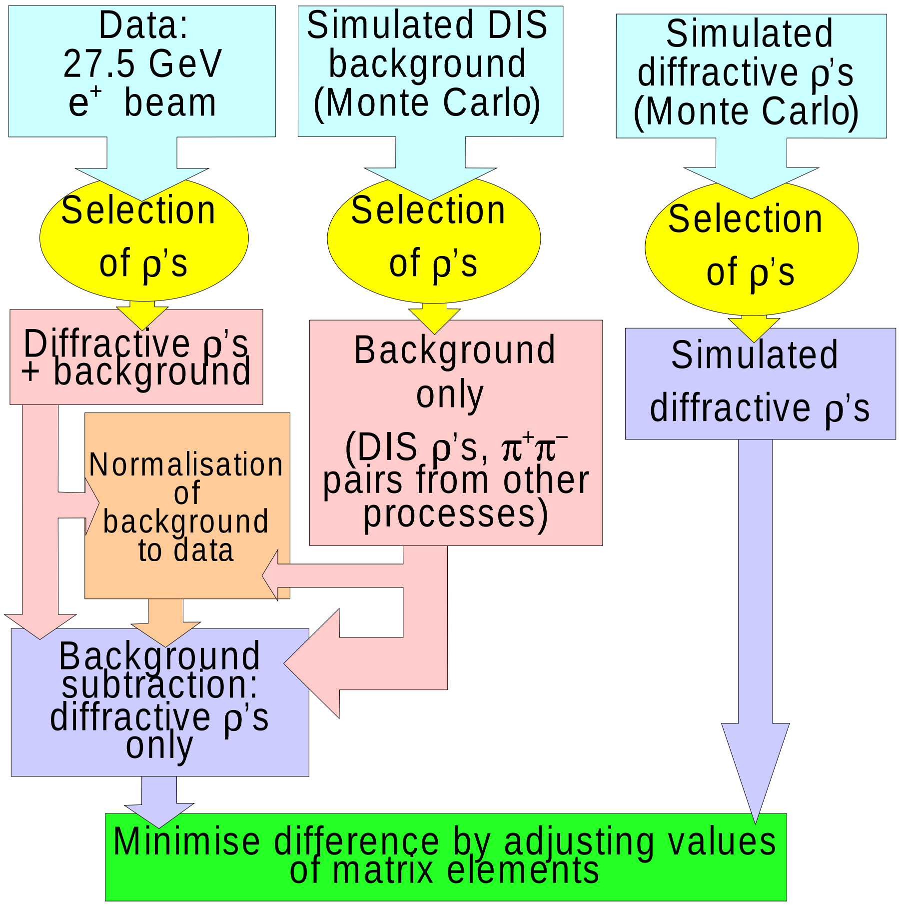

Figure 5.1: Diagram of ρ^0 selection and SDME extraction.

Data quality selection is performed on the run or burst level; this ensures the correctness of the performed measurements. The software then selects out the events of interest through a set of kinematic cuts.

Even though there is a set of cuts that selects out mostly diffractive ρ^0 events, some background events still pass the cuts. The background spectrum is simulated by the Monte Carlo method. The fraction of events in the data sample that belong to the background is thus found and subtracted from the distribution. Only diffractive ρ^0 events are thereby left in the data sample. Normalisation of background to data is necessary to ensure correct background subtraction. All these steps are computerised.

The Spin Density Matrix Elements (SDME) are obtained by fitting the distribution $W(\theta,\ \phi, \Phi)$ given by the sum of Eqns. (2.64) and (2.65) against the real angular distribution from the data. Eqns. (2.64) and (2.65) are simplified with some assumptions to reduce the number of free parameters. In order to give statistical validity to the angular distribution expressions (2.64) and (2.65), a large number of diffractive ρ^0 events was produced with a specially designed Monte Carlo simulation. The fit, performed by the MINUIT minimisation software [41], yields the SDMEs.

Both DIS and diffractive ρ^0 Monte Carlo events are subjected to the same kinematic cuts as the real data events. This ensures the consistency of the procedure. Like the real data, the simulated events are reconstructed with the HRC.

Since the SDMEs depend on Q^2, the events are separated into four Q^2 bins. In this analysis, the same Q^2 bins are used as in the published HERMES results on ^{3}He [42].

5.2 Data Quality

The presence of events in a raw data file does not guarantee their quality: sometimes the detectors operate in a regime that makes a particular type of analysis impossible, the beam may be of poor quality, the software operation and data storage also impose some restrictions on data selection. Events of dubious quality are rejected.

In this analysis, only the runs taken with the ^{1}H target were selected. The target cell was required to be full, and the PID detectors and the crucial tracking chambers were required to be at operational voltage. In addition, requirements on the operation voltage of the detectors, on their proper positioning and on the overall integrity of the equipment were imposed. Runs that did not satisfy any of these conditions were rejected. Additional quality cuts were performed on the burst level. Specifically, events were rejected if:

- Target Atomic Beam Source (ABS) system was off. The target was then molecular rather than atomic, which made target polarisation impossible. This requirement was imposed only on the polarised target data.
- Poor Čerenkov or TRD performance.
- Gains in preshower, calorimeter or luminosity monitor differed from the nominal values.
- Front or back chamber efficiencies were below 80%.
- HV trip detection system was not operational.
- Beam polarisation was outside the 30–80 % range, as reported by polarimeters.
- Beam current was outside the 8–50 mA range.

- DAQ correction factor was below 0.8 or above 1.0. The first case indicates that there was a high deadtime within the DAQ, while the second indicates unphysical deadtime correction corresponding to negative deadtime.
- Burst length was longer than 11 seconds.
- The burst was one of the first three or the last burst in a run. The first 3 bursts of a run were usually characterised by the high DAQ deadtime.

Some additional data quality cuts, that reflect specific details of HERMES soft- and hardware operation, were also imposed.

5.3 The Geometry and Energy Acceptance Cuts

All events must be in a well-defined geometric and kinematic ranges. The experimental constraints may affect the values of measurements and thus distort the true physical picture. Events near the edge of the physical acceptance must be rejected.

The geometry of the magnet defines an allowed acceptance region. Hence only events that satisfied

$$|\arctan(p_y/p_z)| > 0.04 \text{ rad} \tag{5.1}$$

were selected.

In order to ensure that the events originated in the target and did not scatter from the target collimator, cuts were applied on the z vertex position. With $z = 0$ defined in the centre of the target cell, which was coaxial with the z-axis, only tracks satisfying

$$|z \text{ vertex position}| < 18 \text{ cm}, \tag{5.2}$$

were selected. The xy position of the vertex was restricted by the requirement that it should be close to the beam in order to ensure that the interaction was caused by the beam particles. Only tracks that satisfied

$$|\text{transverse distance from vertex to beam}| < 0.75 \text{ cm}, \tag{5.3}$$

were accepted.

Finally, in order to fully contain an electromagnetic shower and, therefore, to measure the energy and momentum of the parent positron properly, the positron must enter the calorimeter sufficiently far away from its edge. This was enforced by requiring that

$$\begin{aligned} &|x \text{ position in calorimeter}| < 175 \text{ cm}, \quad \text{positron only} , \\ &|y \text{ position in calorimeter}| > 30 \text{ cm}, \quad \text{positron only} . \end{aligned} \tag{5.4}$$

Despite the different minimum energy threshold values in the calorimeter for the polarised and unpolarised target operations (refer to Section 3.5), the minimumum energy deposition requirement in this study was maintained at

$$E_{calo} > 3.5 \text{ GeV}, \text{ positron only}, \tag{5.5}$$

regardless of the mode of operation.

5.4 The ρ^0 Event Selection

The analysis performed in this thesis spans a kinematic region of

$$0.5 \text{ GeV}^2 < Q^2 < 4.0 \text{ GeV}^2 , \tag{5.6}$$

and

$$3.8 \text{ GeV} < W < 6.5 \text{ GeV} . \tag{5.7}$$

Diffractive ρ^0 production was characterised by the presence of 3 tracks in the HERMES apparatus: the positron and the two daughter pions (the nucleus is not detected). At this point, it is important to note that the background events were not selected out on the basis of the number of tracks, but instead subtracted via Monte Carlo simulations, after all the cuts were applied. This means that DIS events were not excluded from the sample, as long as they passed the cuts mentioned in the preceding section. Such DIS events were simulated with Monte Carlo.

Once the presence of the scattered positron and the two pions was established for a particular event, it was necessary to determine whether the pions came from a ρ^0 decay. The ρ^0 event selection was made by applying a cut in the invariant mass $M_{2\pi}$. To select the diffractive events, the t' and ΔE cuts were applied. The physical principles behind the above 3 variables were explained in Chapter 2, from which it is apparent that events with $M_{2\pi} \approx 770$ MeV, $t' \approx 0$, and $\Delta E \approx 0$ should be selected.

As mentioned in Chapter 1, ρ^0 events are characterised by a wide $M_{2\pi}$ peak (Fig. 5.2) explained by their short lifetime and the Heisenberg Uncertainty Principle. The t' and ΔE distributions (see Fig. 5.2), also have appreciable widths because of the experimental uncertainty. Hence, in order to include as many diffractive ρ^0 events as possible, the cuts had to be sufficiently wide. Inclusion of as many events as possible reduced the uncertainty due to statistical fluctuations at the cost of larger DIS background.

However, the cuts had to be chosen to discard as many background events as possible. This constrained the width of the cuts from the other side, as the fraction of background events increases with distance from the centre of the peak.

The compromise values of the cuts lie where the overall relative uncertainty of the number of diffractive ρ^0 events is minimal. The cut optimisation is explained in detail in [32]. The final values of the cuts, however, were slightly different from those in [32], and were the same as in [42] to be consistent with the published

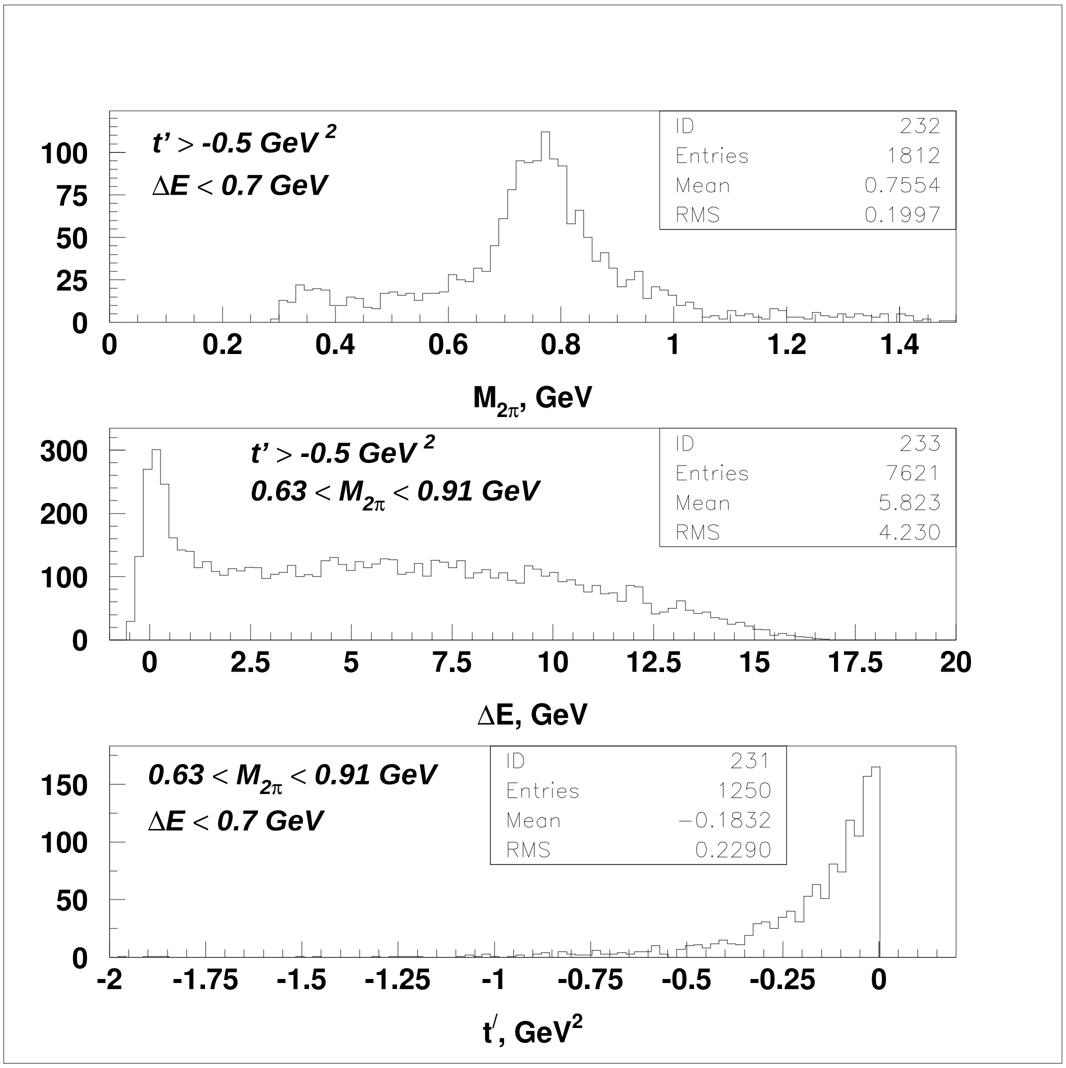

Figure 5.2: $M_{2\pi}$, ΔE and t' distributions with appropriate background elimination cuts applied. The applied cuts are indicated in the figure. The long ΔE tail is due to the DIS background a portion of which survives the $M_{2\pi}$ and t' cuts.

analysis. Only events that satisfy

$$0.63 \text{ GeV} < M_{2\pi} < 0.91 \text{ GeV} \ , \tag{5.8}$$

$$t' > -0.5 \text{ GeV}^2 \ , \tag{5.9}$$

$$\Delta E < 0.7 \text{ GeV} \tag{5.10}$$

were selected.

In addition, in order to minimise the radiative corrections, the requirement

$$y < 0.85 \tag{5.11}$$

is imposed.

The $M_{2\pi}$, t' and y cuts were applied to samples of data and background Monte Carlo separately, before the background was subtracted and before the normalisation procedure was performed. However, the ΔE cut was applied after the background subtraction has been made, since the uncut ΔE spectrum was used for fitting the background Monte Carlo events against the data events above $\Delta E > 3.9$ GeV (see the next section). The choice of applying cuts in $M_{2\pi}$ and t' *before* rather than *after* the background subtraction was dictated by the fact that the ratio of χ^2 to the number of degrees of freedom (NDF) in the normalisation procedure was generally smaller in the first case, which indicates a better quality of fit of the background Monte Carlo to the data. This conclusion is based on the study of the effect of the cut placement on the 1996 data (Table 5.1). In the case when the $M_{2\pi}$ and t' cuts were not applied before the normalisation, they were only applied after the background subtraction, simultaneously with the cut in ΔE. As the right hand side of Table 5.1 demonstrates, the absence of the cuts before the normalisation adversely affects the quality of normalisation in most cases with the exception of bin Q1 in the unpolarised target case and bin Q3 in the polarised target case.

5.5 Background normalisation

In order to subtract the background contribution from the data, the DIS Monte Carlo events needed to be normalised in some way to the data. Only then was it possible to perform an assessment of the background contribution to the

UNPOLARISED 1996:

Bin	$\mathbf{Q^2}$, $\mathrm{GeV}^{\mathbf{2}}$	With $M_{2\pi}$, t' cuts made:			Without $M_{2\pi}$, t' cuts:		
		χ^2	**NDF**	$\frac{\chi^2}{\mathrm{NDF}}$	χ^2	**NDF**	$\frac{\chi^2}{\mathrm{NDF}}$
Q1	$0.50-0.95$	32.15	27	1.19	70.39	29	2.42
Q2	$0.95-1.30$	33.35	26	1.28	40.70	29	1.40
Q3	$1.30-1.96$	30.53	27	1.13	54.24	29	1.87
Q4	$1.96-4.00$	44.56	28	1.59	39.72	29	1.37
Overall	$0.50-4.00$	46.57	28	1.73	84.44	29	2.91

POLARISED 1996:

Bin	$\mathbf{Q^2}$, $\mathrm{GeV}^{\mathbf{2}}$	With $M_{2\pi}$, t' cuts made:			Without $M_{2\pi}$, t' cuts:		
		χ^2	**NDF**	$\frac{\chi^2}{\mathrm{NDF}}$	χ^2	**NDF**	$\frac{\chi^2}{\mathrm{NDF}}$
Q1	$0.50-0.95$	24.96	27	0.92	43.66	29	1.51
Q2	$0.95-1.30$	25.25	26	0.97	37.64	29	1.30
Q3	$1.30-1.96$	58.40	27	2.16	38.84	29	1.34
Q4	$1.96-4.00$	38.40	28	1.37	59.60	29	2.06
Overall	$0.50-4.00$	28.32	28	1.01	98.78	29	3.41

Table 5.1: Comparison of the normalisation fit quality for the two cut placement methods.

data distribution and to carry out the subtraction. The normalisation of the distribution of the DIS Monte Carlo events to the data was based on the marked similarity in the distribution in the region where $\Delta E \gg 0$ (Fig. 5.3). High ΔE corresponds purely to the DIS events.

Accordingly, the Monte Carlo distribution above $\Delta E > 3.9$ GeV was normalised and the normalisation factor N was obtained. The full original Monte Carlo distribution is then multiplied by N. The simulated background events represented an estimate of the true background contribution to the data under

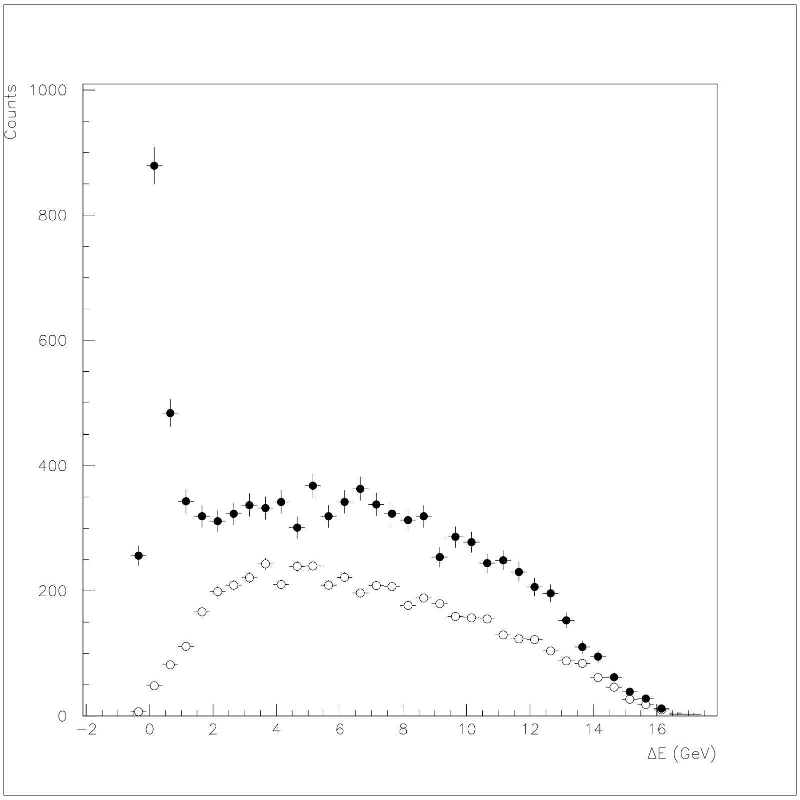

Figure 5.3: Unnormalised background Monte Carlo Distribution (*polarised 1997 data are shown*). The behaviour above ≈ 3 GeV is similar for data and background.

the ρ^0 peak at $\Delta E \approx 0$ (Fig. 5.4). The simulated distributions and the DIS portions of the data distribution in Q^2, W^2, $M_{2\pi}$, t', ν and ϵ are compared in Fig. 5.5.

Following the background subtraction, the ΔE cut was applied as in Eqn. (5.10). The number of data events that passed *all* the cuts and the percentage of background events among them are summarised in Table 5.2.

Because of some differences in the apparatus, separate Monte Carlo simulations were conducted for the 1996 and 1997 data. Each DIS Monte Carlo event was associated with a statistical *weight*, which was a measure of relative prob-

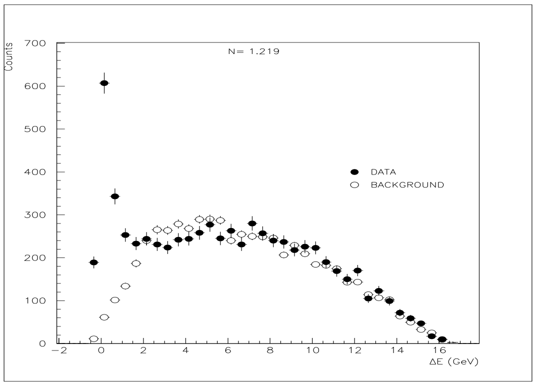

(a) Unpolarised 1996

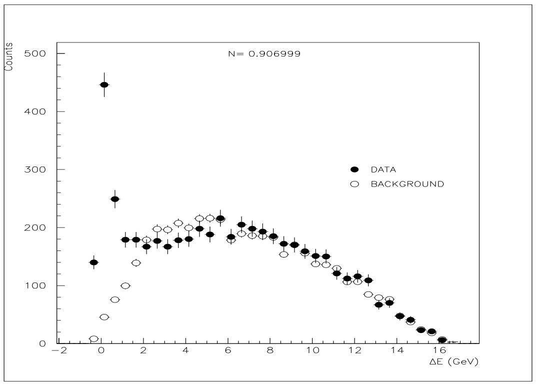

(b) Polarised 1996

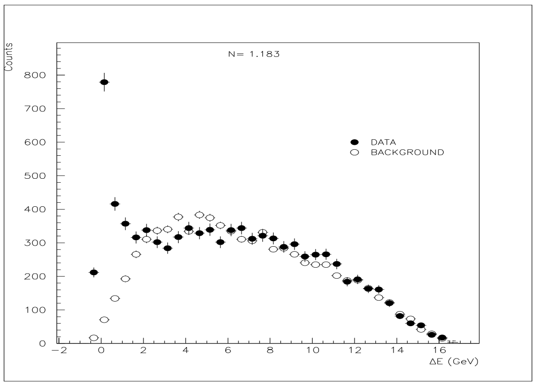

(c) Unpolarised 1997

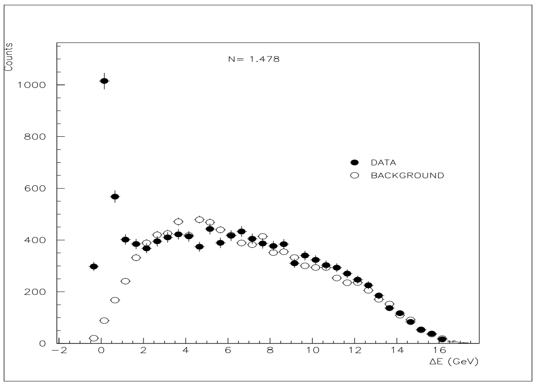

(d) Polarised 1997

Figure 5.4: Data and Normalised HMC Monte Carlo Distributions.

ability of encountering such an event in reality with respect to the entire DIS spectrum. All Monte Carlo events were produced at the University of Alberta. The summary of Monte Carlo production is given in Table 5.3.

5.6 Matrix Elements Determination Method

The data analysed here were collected in 1996 and 1997 on ^1H target nuclei, both polarised and unpolarised. The unpolarised and polarised target data were

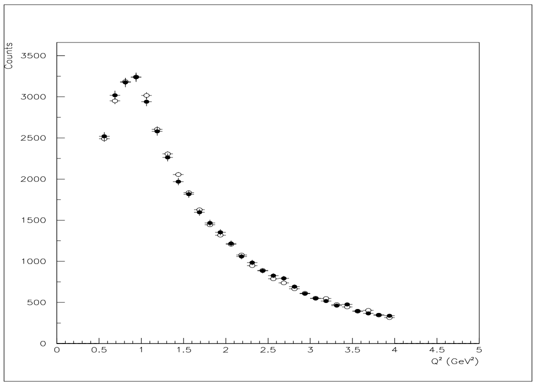

(a) Q^2

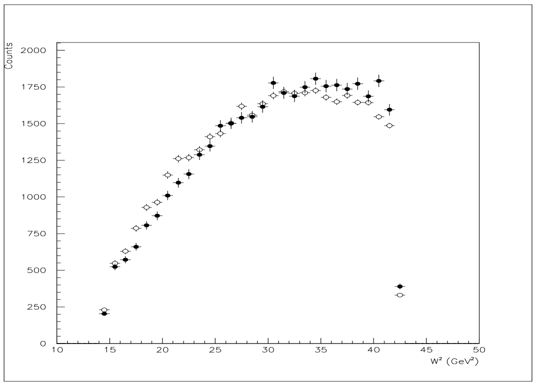

(b) W^2

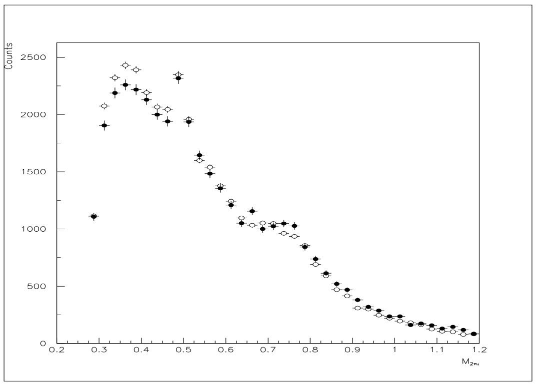

(c) $M_{2\pi}$

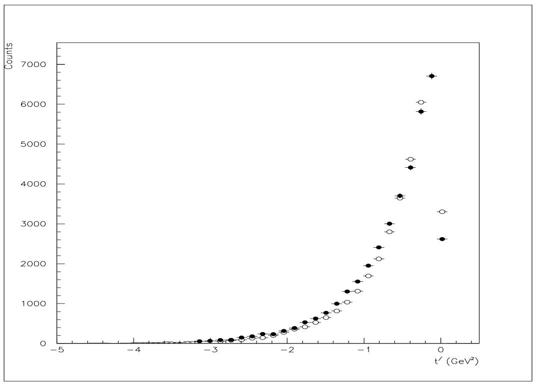

(d) t'

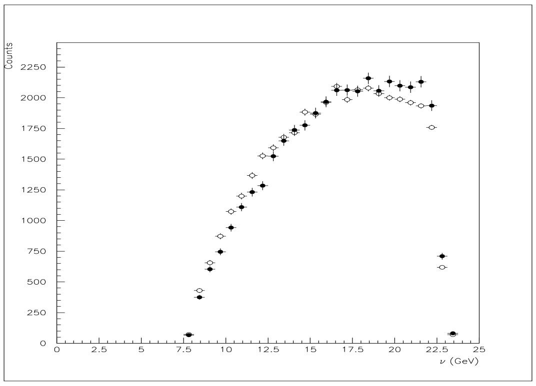

(e) ν

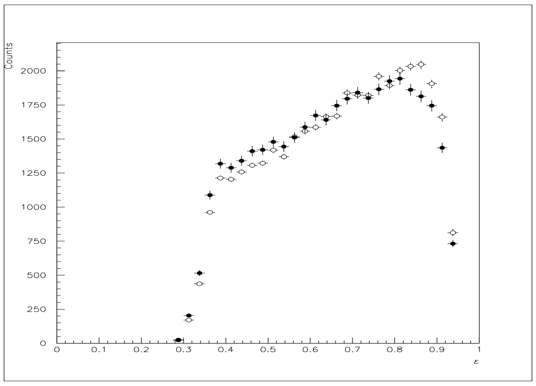

(f) ϵ

Figure 5.5: Comparison of DIS Monte Carlo to data in Q^2, W^2, $M_{2\pi}$, t', ν and ϵ. A cut $\Delta E > 2.1$ is imposed to eliminate the diffractive ρ^0 portion from the data. Unpolarised 1996 data are shown as an example.

Bin	Unpol. 1996	% DIS backgr.	Pol. 1996	% DIS backgr.	Unpol. 1997	% DIS backgr.	Pol. 1997	% DIS backgr.
Q1	200	6±7	135	7±9	245	8±7	319	8±6
Q2	224	13±7	175	11±8	306	8±6	420	8±5
Q3	231	13±7	191	11±7	273	14±6	415	12±5
Q4	222	18±7	127	23±9	254	16±6	315	16±6
Tot.	877	13±3	628	12±4	1078	11±3	1469	11±3

Table 5.2: Summary of candidate ρ^0 events selected and percentage of background events among them. The uncertainty includes statistical contributions from both background and data.

Bin	DIS Monte Carlo 1996	DIS Monte Carlo 1997	Diffractive ρ^0 Monte Carlo 1996	Diffractive ρ^0 Monte Carlo 1997
Q1	17	24	51345	49631
Q2	45	40	64910	63201
Q3	69	89	67079	66085
Q4	164	188	72125	71917
Tot.	295	341	255459	250834

Table 5.3: Summary of Monte Carlo events produced. Event weights and normalisation factors are not included for the DIS events, so that the actual numbers of events that pass all cuts are displayed.

analysed separately. 1996 and 1997 data were also analysed separately from each other. This results in 4 separate sets of data: one for each year with each target polarisation mode. This analysis is similar to the one performed for earlier

HERMES results [42].

The one-dimensional angular distributions given by Eqns. (2.66), (2.67), (2.68), and (2.69) depend on only seven parameters: r^{04}_{00}, r^{1}_{1-1}, r^{04}_{1-1}, $\mathrm{Im}(r^{3}_{1-1})$, $\mathrm{Tr}(r^1)$, $\mathrm{Tr}(r^5)$, and $\mathrm{Tr}(r^8)$. These were taken as free parameters. The eighth free parameter was the phase angle δ that constrains the following elements present in (2.64) and (2.65):

$$-\mathrm{Im}(r^{6}_{10}) = \mathrm{Re}(r^{5}_{10}) \equiv \frac{1}{2}\sqrt{\frac{R}{2}}\frac{\cos\delta}{1+\epsilon R} \ , \tag{5.12}$$

and

$$\mathrm{Im}(r^{7}_{10}) = \mathrm{Re}(r^{8}_{10}) \equiv \frac{1}{2}\sqrt{\frac{R}{2}}\frac{\sin\delta}{1+\epsilon R} \tag{5.13}$$

where the expression for R, assuming S-Channel Helicity Conservation (SCHC), simplifies to

$$R \equiv \frac{\sigma_L}{\sigma_T} = \frac{1}{\epsilon}\frac{r^{04}_{00}}{1-r^{04}_{00}} \ . \tag{5.14}$$

With SCHC, R is beam energy-independent.

The remaining elements were subject to the following assumptions [42]:

$$r^{1,5,8}_{00} = \mathrm{Tr}(r^{1,5,8})r^{04}_{00} \ , \tag{5.15}$$

$$r^{1,5,8}_{11} = \mathrm{Tr}(r^{1,5,8})\ \frac{1}{2}\left(1-r^{04}_{00}\right) \ , \tag{5.16}$$

and, assuming SCHC,

$$\mathrm{Im}(r^{2}_{1-1}) = -r^{1}_{1-1} \ , \tag{5.17}$$

$$r^{5,6,7,8}_{1-1} = r^{1,2,3,04}_{10} = 0 \ . \tag{5.18}$$

The angular distribution now becomes

$$
\begin{aligned}
W(\cos\theta,\ \phi,\ \Phi) = \frac{3}{4\pi}\Bigg\{ & \tfrac{1}{2}(1-r^{04}_{00}) + \tfrac{1}{2}(3r^{04}_{00}-1)\cos^2\theta - r^{04}_{1-1}\sin^2\theta\cos 2\phi \\
& -\epsilon\cos 2\Phi\Big(\mathrm{Tr}(r^1)\left\{\tfrac{1}{2}(1-r^{04}_{00})\sin^2\theta + r^{04}_{00}\cos^2\theta\right\} - r^1_{1-1}\sin^2\theta\cos 2\phi\Big) \\
& +\epsilon\sin 2\Phi\ r^1_{1-1}\sin^2\theta\sin 2\phi \\
& +\sqrt{2\epsilon(1+\epsilon)}\cos\Phi\Big(\mathrm{Tr}(r^5)\left\{\tfrac{1}{2}(1-r^{04}_{00})\sin^2\theta + r^{04}_{00}\cos^2\theta\right\} \\
& -\tfrac{1}{2}\sqrt{\tfrac{r^{04}_{00}(1-r^{04}_{00})}{\epsilon}}\cos\delta\sin 2\theta\cos\phi\Big) \\
& -\sqrt{\epsilon(1+\epsilon)}\sin\Phi\sqrt{\tfrac{r^{04}_{00}(1-r^{04}_{00})}{2\epsilon}}\cos\delta\sin 2\theta\sin\phi \\
& +P_b\Big[\sqrt{1-\epsilon^2}\ \mathrm{Im}(r^3_{1-1})\sin^2\theta\sin 2\phi \\
& +\sqrt{\epsilon(1-\epsilon)}\cos\Phi\sqrt{\tfrac{r^{04}_{00}(1-r^{04}_{00})}{2\epsilon}}\sin\delta\sin 2\theta\sin\phi \\
& +\sqrt{2\epsilon(1-\epsilon)}\sin\Phi\Big(\mathrm{Tr}(r^8)\left\{\tfrac{1}{2}(1-r^{04}_{00})\sin^2\theta + r^{04}_{00}\cos^2\theta\right\} \\
& -\tfrac{1}{2}\sqrt{\tfrac{r^{04}_{00}(1-r^{04}_{00})}{\epsilon}}\sin\delta\sin 2\theta\cos\phi\Big)\Big]\Bigg\}\ ,
\end{aligned}
\tag{5.19}
$$

where the constant P_b represents the average beam polarisation over an entire set of data. The above angular distribution function was folded into an *isotropic* angular distribution of diffractive ρ^0 events, in each Q^2 bin. To assess the number of events that belong to a certain region (bin) $\Delta(\cos\theta)$, $\Delta\phi$, $\Delta\Phi$ and $\Delta\psi$ ($\psi = \phi - \Phi$), the diffractive ρ^0 spectrum was simulated via a diffractive vector meson Monte Carlo simulation (BMC, refer to Section 4.3), which produces isotropic angular distributions. The result of the simulation was a large set of 3-track events that correspond to the diffractive ρ^0 mesons, with momenta of the outgoing e^+, π^+, and π^- written to a computer file. In order to account for the acceptance effects, these 3-track events were fed into the standard HERMES Monte Carlo, which in turn simulated the detector response of HERMES apparatus to these simulated events. Each event was then reconstructed with HRC to obtain full information about the trajectories of particles that would result in such detector response. As a result, the detector acceptance effects were taken

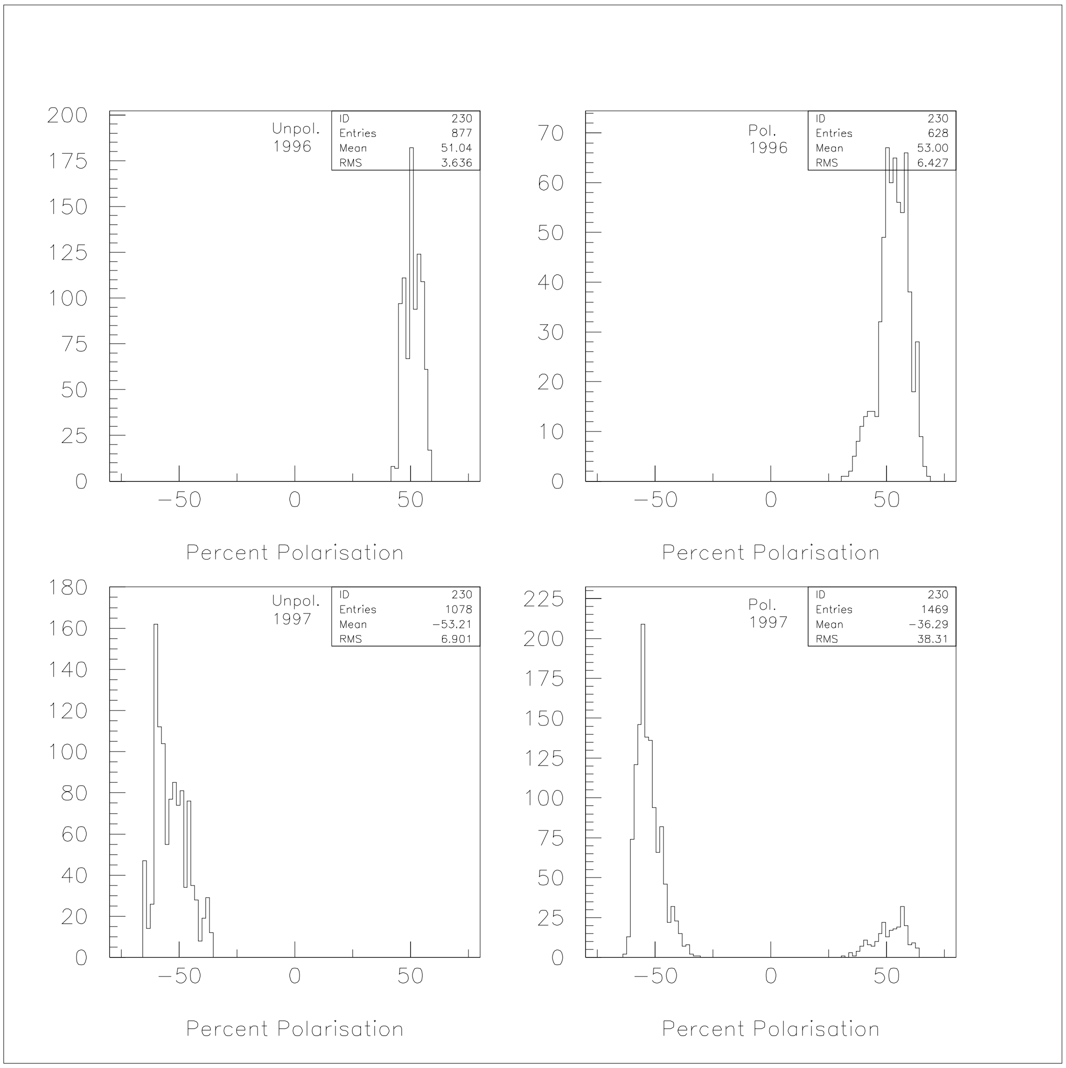

Figure 5.6: Average beam polarisation for the four sets of data.

into account, and the events were fully reconstructed. The following bin widths were used:

$$\Delta(\cos\theta) = 1/10,\ -1 \leq \cos\theta \leq 1\ , \tag{5.20}$$

$$\Delta\phi = 18^\circ,\ -180^\circ \leq \phi \leq 180^\circ\ , \tag{5.21}$$

$$\Delta\Phi = 18^\circ,\ -180^\circ \leq \Phi \leq 180^\circ\ . \tag{5.22}$$

$$\Delta\psi = 18^\circ,\ -180^\circ \leq \psi \leq 180^\circ\ . \tag{5.23}$$

With such binning, distributions in each angle were divided into 20 bins. Since the four sets of data were analysed separately, different polarisation values were used for each set (Fig. 5.6). Negative values of polarisation correspond to antiparallel alignment of positron spins with respect to their momenta.

Once all the necessary cuts were applied to the background-subtracted diffractive ρ^0 data and to the simulated diffractive ρ^0 events, the difference between the real and simulated distributions was minimised with the MINUIT software package by adjusting the values of the eight parameters. As explained earlier in this chapter, the quality of the fit was characterised by the ratio of χ^2 to the number of degrees of freedom (NDF) in the fit. The minimisation procedure is summarised by the following algorithm.

1. Arbitrary starting values of the eight parameters are assumed.

2. The simulated ρ^0 event distribution was normalised to the data.

3. With the guess values of the parameters, $W(\cos\theta,\ \phi,\ \Phi)$ was calculated. In calculation of $W(\cos\theta,\ \phi,\ \Phi)$, the *raw* rather than reconstructed values were used. This was dictated by the fact that the simulated events followed the assumed isotropic model precisely, without any detector effects. The resulting distribution $W(\cos\theta,\ \phi,\ \Phi)$ yielded one-dimensional distributions $W(\cos\theta)$, $W(\phi)$, $W(\Phi)$ and $W(\psi)$.

4. Since it was impossible to perform a three-dimensional fit with so few ρ^0 events, the one-dimensional distributions were used to compare the data to the Monte Carlo model in each of the 20 bins of the four distributions. As a measure of the difference between the data and the optimised MC model, χ^2 was calculated.

5. After the χ^2 was calculated, the software modifies the free parameters to attempt to reduce the χ^2 in the next cycle.

6. The program returned to Step 2 and the cycle was repeated until the minimum χ^2 was found.

χ^2 in Step 4 was calculated according to

$$\begin{aligned}\chi^2 &= \sum_{i=1}^{2} 0 \left(\frac{\{D_i(\cos\theta) - M_i(\cos\theta)\}^2}{\{\delta D_i(\cos\theta)\}^2 + \{\delta M_i(\cos\theta)\}^2} + \frac{\{D_i(\phi) - M_i(\phi)\}^2}{\{\delta D_i(\phi)\}^2 + \{\delta M_i(\phi)\}^2} \right. \\ &+ \left. \frac{\{D_i(\Phi) - M_i(\Phi)\}^2}{\{\delta D_i(\Phi)\}^2 + \{\delta M_i(\Phi)\}^2} + \frac{\{D_i(\psi) - M_i(\psi)\}^2}{\{\delta D_i(\psi)\}^2 + \{\delta M_i(\psi)\}^2} \right) , \end{aligned} \tag{5.24}$$

where D_i, M_i, δD_i and δM_i denote the number of data events, the number of Monte Carlo events, the uncertainty in the number of the data events and the uncertainty in the number of Monte Carlo events in bin i, respectively. The Monte Carlo distributions were built up from the weights $W_{ik}(\cos\theta,\ \phi,\ \Phi)$ given by (5.19) and calculated for each event k belonging to a bin i. The number of data events in bin i is the difference between the number of the data events before the background subtraction B_i and the number of the weighted (See Section 5.5) normalised DIS background events simulated with the HMC H_i:

$$D_i = B_i - NH_i \ , \tag{5.25}$$

where N is the normalisation factor. The number of Monte Carlo events in bin i was computed as follows:

$$M_i = \sum_k W_{ik}(\cos\theta,\ \phi,\ \Phi) \ . \tag{5.26}$$

The uncertainties were calculated according to

$$\delta D_i = \sqrt{B_i + N^2 H_i} \tag{5.27}$$

and

$$\delta M_i = \sqrt{\sum_k \{W_{ik}(\cos\theta,\ \phi,\ \Phi)\}^2} \ . \tag{5.28}$$

Since the fits in were performed in the one-dimensional distributions $W(\theta)$, $W(\phi)$ and $W(\Phi)$, rather than in $W(\cos\theta,\ \phi,\ \Phi)$, it was essential to prevent MINUIT from finding false minima which did not correspond to the global minimum in $W(\cos\theta,\ \phi,\ \Phi)$. The connection between these was reinforced by fitting in $W(\psi)$, since finding false minima in the $W(\theta)$, $W(\phi)$ and $W(\Phi)$ distributions would result in a large χ^2 contribution from the $W(\psi)$ distribution.

The fit quality information and the mean values of the polarisation parameter ϵ for each case are summarised in Table 5.4. Since each of the 4 single-variable angular distributions was subdivided into 20 bins, with 8 free parameters in the fit, $\mathrm{NDF} = 4 \times 20 - 8 = 72$.

5.7 Results and Their Interpretation

This section presents a summary of all final results and their interpretation in light of SCHC and Natural Parity Exchange (NPE).

The the 1996 data with a polarised target have a lower number of ρ^0 events than the other three sets. As seen in Table 5.4, for bin Q4, $\frac{\chi^2}{\mathrm{NDF}} = 3.9$, which is markedly larger than in any other case. This suggests that the final minimisation results in that bin may be unreliable. Additional evidence for a problem with results for 1996 polarised target data in bin Q4 emerges from some of the final values in that case, and a treatment for this problem is described. All uncertainties displayed below include only the statistical fit uncertainties provided by MINUIT.

Examination of the final r_{00}^{04} values (Table 5.5) reveals that the four results in every bin agree with one another within error in all possible combinations, with the only exception of unpolarised target value for 1996 in Q2. The value in bin Q4 in the case of 1996 polarised target data is not very different from the other 3 cases in the same bin, although its uncertainty is the highest of all 16 values

Q^2 Bin	**Unpolarised** 1996				**Polarised** 1996			
	$\langle Q^2 \rangle$, GeV^2	$\langle \epsilon \rangle$	χ^2	$\frac{\chi^2}{\text{NDF}}$	$\langle Q^2 \rangle$, GeV^2	$\langle \epsilon \rangle$	χ^2	$\frac{\chi^2}{\text{NDF}}$
Q1	0.79	0.769	74	1.0	0.79	0.761	76	1.1
Q2	1.12	0.820	67	0.9	1.12	0.830	86	1.2
Q3	1.59	0.828	70	1.0	1.58	0.825	133	1.8
Q4	2.66	0.812	127	1.8	2.61	0.792	283	3.9

Q^2 Bin	**Unpolarised** 1997				**Polarised** 1997			
	$\langle Q^2 \rangle$, GeV^2	$\langle \epsilon \rangle$	χ^2	$\frac{\chi^2}{\text{NDF}}$	$\langle Q^2 \rangle$, GeV^2	$\langle \epsilon \rangle$	χ^2	$\frac{\chi^2}{\text{NDF}}$
Q1	0.79	0.770	90	1.3	0.79	0.769	74	1.0
Q2	1.13	0.836	101	1.4	1.12	0.840	116	1.6
Q3	1.58	0.804	85	1.2	1.56	0.840	72	1.0
Q4	2.66	0.804	119	1.7	2.62	0.796	64	0.9

Table 5.4: Case-by-case summary of the MINUIT χ^2 fit quality. The total χ^2 for all four angular distributions is included. NDF = 72 for all cases. ϵ is the mean virtual photon polarisation.

shown.

The results from the fitting for r^1_{1-1} (Table 5.6) also demonstrate general agreement within error among values within one Q^2 bin. However, more cases of disagreement are found relative to those in r^{04}_{00}. The marked oddity is the large negative value in bin Q4 for polarised 1996 data.

Q^2 **Bin**	**Unpolarised** 1996	**Polarised** 1996	**Unpolarised** 1997	**Polarised** 1997
Q1	0.32 ± 0.07	0.27 ± 0.10	0.35 ± 0.09	0.34 ± 0.07
Q2	0.31 ± 0.07	0.48 ± 0.09	0.50 ± 0.08	0.44 ± 0.06
Q3	0.58 ± 0.06	0.52 ± 0.06	0.56 ± 0.08	0.50 ± 0.07
Q4	0.62 ± 0.08	0.54 ± 0.12	0.63 ± 0.06	0.67 ± 0.04

Table 5.5: Results for r^{04}_{00}.

Q^2 **Bin**	**Unpolarised** 1996	**Polarised** 1996	**Unpolarised** 1997	**Polarised** 1997
Q1	0.42 ± 0.07	0.45 ± 0.09	0.43 ± 0.10	0.40 ± 0.07
Q2	0.38 ± 0.06	0.35 ± 0.07	0.21 ± 0.07	0.27 ± 0.05
Q3	0.30 ± 0.04	0.35 ± 0.04	0.19 ± 0.06	0.25 ± 0.05
Q4	0.09 ± 0.07	−0.29 ± 0.09	0.20 ± 0.06	0.23 ± 0.04

Table 5.6: Results for r^{1}_{1-1}.

With experimental results for r^{04}_{00} and r^{1}_{1-1} known, it is possible to perform the first test of the hypotheses of SCHC and NPE by checking whether the experimental results agree with

$$2r^{1}_{1-1} + r^{04}_{00} = 1 \ . \tag{5.29}$$

Uncertainty is calculated according to [43]

$$\delta(2r^{1}_{1-1} + r^{04}_{00}) = \sqrt{4[\delta(r^{1}_{1-1})]^2 + [\delta(r^{04}_{00})]^2 + 4r\delta(r^{1}_{1-1})\delta(r^{04}_{00})} \ , \tag{5.30}$$

where r is the *correlation coefficient* between the r^{04}_{00} and r^{1}_{1-1}. Correlation coefficients for all variables in all cases are listed in Appendix E.

Q^2 Bin	**Unpolarised** 1996	**Polarised** 1996	**Unpolarised** 1997	**Polarised** 1997
Q1	1.17 ± 0.10	1.18 ± 0.14	1.21 ± 0.15	1.13 ± 0.10
Q2	1.07 ± 0.09	1.18 ± 0.09	0.92 ± 0.11	0.97 ± 0.06
Q3	1.18 ± 0.07	1.21 ± 0.06	0.94 ± 0.09	1.00 ± 0.10
Q4	0.79 ± 0.12	-0.03 ± 0.19	1.02 ± 0.11	1.13 ± 0.06

Table 5.7: Results for $2r^1_{1-1} + r^{04}_{00}$.

Examination of the calculated values of $2r^1_{1-1} + r^1_{1-1}$ (Table 5.7) reveals that they disagree with (5.29) in more than one half of the cases. The disagreement is very large, though not surprising, for the high χ^2 case of polarised 1996 data in bin Q4. The other tests of SCHC, but not NPE, arise from checking whether $r^{04}_{1-1} = \ \mathrm{Im}(r^3_{1-1}) = \mathrm{Tr}(r^{1,5,8}) = 0$.

Values of r^{04}_{1-1}, with the exception of those in the polarised 1996 data set, are mostly consistent with zero within their errors (Table 5.8). Values of Im r^3_{1-1} are characterised by higher uncertainties, and fewer cases of agreement within error (Table 5.9). However, the results fluctuate around zero without any systematic

Q^2 Bin	**Unpolarised** 1996	**Polarised** 1996	**Unpolarised** 1997	**Polarised** 1997
Q1	-0.05 ± 0.05	0.15 ± 0.07	0.03 ± 0.07	-0.03 ± 0.05
Q2	0.06 ± 0.06	0.25 ± 0.06	-0.02 ± 0.05	-0.06 ± 0.04
Q3	0.04 ± 0.04	0.15 ± 0.04	-0.07 ± 0.06	0.02 ± 0.04
Q4	-0.13 ± 0.06	0.16 ± 0.12	-0.04 ± 0.04	-0.03 ± 0.03

Table 5.8: Results for r^{04}_{1-1}.

Q^2 Bin	**Unpolarised** 1996	**Polarised** 1996	**Unpolarised** 1997	**Polarised** 1997
Q1	-0.14 ± 0.16	-0.27 ± 0.21	0.53 ± 0.23	0.39 ± 0.21
Q2	-0.07 ± 0.19	-0.06 ± 0.20	-0.52 ± 0.17	-0.15 ± 0.21
Q3	-0.07 ± 0.11	0.32 ± 0.12	-0.16 ± 0.16	0.04 ± 0.17
Q4	0.32 ± 0.18	-0.35 ± 0.28	0.10 ± 0.11	-0.18 ± 0.14

Table 5.9: Results for $\mathrm{Im}(r^3_{1-1})$.

pattern.

Values of $\mathrm{Tr}(r^1)$ generally agree with each other (Table 5.10). As in the previous case, the results fluctuate around zero in a random pattern. Unlike previous cases, 14 out of 16 values of $\mathrm{Tr}(r^5)$ (Table 5.11) are positive and generally do not agree with zero within errors. The statistical uncertainties in $\mathrm{Tr}(r^5)$, as the table demonstrates, are generally small. Hence, the results for $\mathrm{Tr}(r^5)$ are not consistent with zero, and therefore disagree with SCHC.

Values of $\mathrm{Tr}(r^8)$ (Table 5.12) are characterised by large uncertainties. The majority of them agree with zero within their errors; there is approximately an equal number of positive and negative values. The value in the high χ^2 case of

Q^2 Bin	**Unpolarised** 1996	**Polarised** 1996	**Unpolarised** 1997	**Polarised** 1997
Q1	-0.14 ± 0.15	-0.10 ± 0.21	0.19 ± 0.18	0.01 ± 0.12
Q2	0.18 ± 0.16	0.34 ± 0.17	-0.18 ± 0.15	-0.30 ± 0.12
Q3	-0.03 ± 0.11	0.09 ± 0.10	-0.28 ± 0.17	-0.04 ± 0.10
Q4	-0.42 ± 0.20	0.38 ± 0.36	-0.07 ± 0.14	0.11 ± 0.11

Table 5.10: Results for $\mathrm{Tr}(r^1)$.

Q^2 **Bin**	**Unpolarised** 1996	**Polarised** 1996	**Unpolarised** 1997	**Polarised** 1997
Q1	0.13 ± 0.11	0.17 ± 0.14	-0.08 ± 0.15	0.09 ± 0.10
Q2	0.04 ± 0.07	0.00 ± 0.08	0.07 ± 0.09	0.11 ± 0.06
Q3	0.25 ± 0.05	0.20 ± 0.05	0.06 ± 0.07	0.22 ± 0.05
Q4	0.06 ± 0.08	-0.22 ± 0.14	0.24 ± 0.06	0.23 ± 0.04

Table 5.11: Results for $\mathrm{Tr}(r^5)$.

polarised 1996 data in bin Q4 is significantly higher than the other 15 values. The values of δ (Table 5.13) fluctuate without any consistent pattern.

Since there are four results for each quantity, it is desirable to take a *weighted average* [43] of the four cases. The input results X_i (Tables 5.5, 5.6, 5.8–5.13) in each of the four cases i are weighted with respect to their uncertainties δX_i, with the weights w_i given by

$$w_i = \frac{1}{(\delta X_i)^2} \; . \tag{5.31}$$

Q^2 **Bin**	**Unpolarised** 1996	**Polarised** 1996	**Unpolarised** 1997	**Polarised** 1997
Q1	-0.0 ± 0.4	0.3 ± 0.5	-0.7 ± 0.5	-0.5 ± 0.5
Q2	-0.3 ± 0.5	0.4 ± 0.5	0.7 ± 0.4	0.9 ± 0.4
Q3	-0.1 ± 0.3	0.1 ± 0.2	0.5 ± 0.4	-0.3 ± 0.4
Q4	0.0 ± 0.4	2.5 ± 0.7	0.0 ± 0.3	-0.2 ± 0.4

Table 5.12: Results for $\mathrm{Tr}(r^8)$.

Q^2 Bin	**Unpolarised** 1996	**Polarised** 1996	**Unpolarised** 1997	**Polarised** 1997
Q1	1.8 ± 0.4	0.6 ± 1.0	0.4 ± 1.2	1.2 ± 0.3
Q2	-0.1 ± 0.7	-0.1 ± 0.5	0.5 ± 1.0	0.0 ± 0.5
Q3	2.1 ± 0.4	2.1 ± 0.4	0.2 ± 0.7	-1.2 ± 0.6
Q4	0.1 ± 0.6	0.6 ± 0.7	-2.3 ± 0.8	3.1 ± 0.8

Table 5.13: Results for δ in radians.

With this definition, the weighted average $\overline{X}$ is computed according to

$$\overline{X} = \frac{\sum_i w_i X_i}{\sum_i w_i} , \tag{5.32}$$

with uncertainty given by

$$\delta\overline{X} = \frac{1}{\sqrt{\sum_i w_i}} . \tag{5.33}$$

However, high χ^2 and obviously anomalous values of r^1_{1-1} and $\mathrm{Tr}(r^8)$ in Q4 in the case of 1996 polarised target data cast doubts over the validity of results in that case. Therefore, all values for polarised 1996 data in Q4 were rejected, and the averaging in bin Q4 was performed over the remaining 3 cases.

Table 5.14 displays the weighted average values of all results, where the polarised 1996 case in Q4 was excluded. Even though the values displayed in all tables were rounded off according to the magnitude of their uncertainties, *all* available significant figures were used in calculations of the average. Only then were the displayed values rounded off.

The average values of $\mathrm{Tr}(r^1)$ agree within error with zero in all four bins and, therefore, with SCHC. The average values of $\mathrm{Im}(r^3_{1-1})$ and $\mathrm{Tr}(r^8)$ also agree with zero in 3 bins, although the values of $\mathrm{Tr}(r^8)$ have comparatively large uncertainty. In the instances where zero does not fall into the value range allowed by the statistical uncertainty, the disagreement is only marginal, and will likely

$\overline{\langle Q^2 \rangle}$, GeV^2	$\overline{\langle \epsilon \rangle}$	$\overline{r^{04}_{00}}$	$\overline{r^{1}_{1-1}}$	$\overline{r^{04}_{1-1}}$	$\overline{\mathrm{Im}(r^{3}_{1-1})}$
0.79	0.768	0.33 ± 0.04	0.42 ± 0.04	0.005 ± 0.029	0.07 ± 0.10
1.12	0.833	0.43 ± 0.04	0.30 ± 0.03	0.034 ± 0.027	−0.23 ± 0.10
1.57	0.826	0.54 ± 0.03	0.29 ± 0.02	0.048 ± 0.021	0.06 ± 0.07
2.64	0.803	0.65 ± 0.03	0.20 ± 0.03	−0.045 ± 0.024	0.05 ± 0.08

$\overline{\langle Q^2 \rangle}$, GeV^2	$\overline{\langle \epsilon \rangle}$	$\overline{\mathrm{Tr}(r^1)}$	$\overline{\mathrm{Tr}(r^5)}$	$\overline{\mathrm{Tr}(r^8)}$	$\overline{\delta}$
0.79	0.768	−0.01 ± 0.08	0.09 ± 0.06	−0.20 ± 0.22	1.4 ± 0.2
1.12	0.833	−0.06 ± 0.07	0.06 ± 0.04	0.46 ± 0.22	0.0 ± 0.3
1.57	0.826	−0.02 ± 0.06	0.20 ± 0.03	0.03 ± 0.15	1.3 ± 0.3
2.64	0.803	−0.03 ± 0.08	0.21 ± 0.03	−0.08 ± 0.19	0.2 ± 0.4

Table 5.14: Weighted average values of the results. The polarised 1996 case was excluded from calculation of the average in bin Q4.

be accounted for by the systematic uncertainty not included into the table. By contrast, the values of $\mathrm{Tr}(r^5)$ are consistently positive and disagree with zero in all four bins. Hence, the values of $\mathrm{Tr}(r^5)$ are not consistent with SCHC.

If the values of r^1_{1-1} and r^{04}_{00} agree with SCHC and NPE, they must agree with (5.29). The average values of $2r^1_{1-1}+r^{04}_{00}$ (Table 5.15) agree with this relationship only in bins Q2 and Q4. The systematic disagreement of $2r^1_{1-1}+r^{04}_{00}$ from 1, such that all four values are > 1, suggests a degree of violation of NPE and/or SCHC.

Thus the results demonstrate that SCHC is generally obeyed, albeit with a small degree of violation. Since the confirmation of NPE requires that SCHC be

$\overline{\langle Q^2 \rangle}$, GeV^2	$\overline{\langle \epsilon \rangle}$	$\overline{2r^1_{1-1} + r^{04}_{00}}$
0.79	0.768	1.16 $\pm$ 0.06
1.12	0.833	1.03 $\pm$ 0.04
1.57	0.826	1.12 $\pm$ 0.04
2.64	0.803	1.05 $\pm$ 0.05

Table 5.15: Weighted average values of $2r^1_{1-1} + r^{04}_{00}$. The polarised 1996 case was excluded from calculation of the average in bin Q4.

obeyed, it is impossible to assess the extent of NPE violation with the presented method. Disagreement with (5.29) was found in half of all cases; it is impossible to conclude whether it is caused by violation of SCHC, or by violation of NPE, or both.

Comparison of the newly-determined values of r^{04}_{00} with the world data (see refs. [44–51]) (Fig. 5.7a) reveals that the values fit into the trend set by results from other experiments with ^{1}H target in the neighboring regions. However, the 1995 ^{3}He HERMES results lie below this trend.

Examination of the world data on r^1_{1-1} (Fig. 5.7) shows that the results match the 1995 ^{3}He results very closely in the lower 3 bins and, at the same time, lie above the values from the other ^{1}H target experiments. It was not expected that the ^{3}He and ^{1}H results would agree with each other closely, because of the presence of coherent nuclear effects in the ^{3}He nucleus [52]. Furthermore, the ^{1}H results were expected to reside within the general trend. The disagreement suggests a large systematic uncertainty, which is subject to further study. See the next section for an overview of possible sources of systematic uncertainty.

The results for Imr^3_{1-1} (Fig. 5.8) and Tr(r^1) (Fig. 5.9) agree reasonably well with the world data; their closeness to zero is in line with the expectations

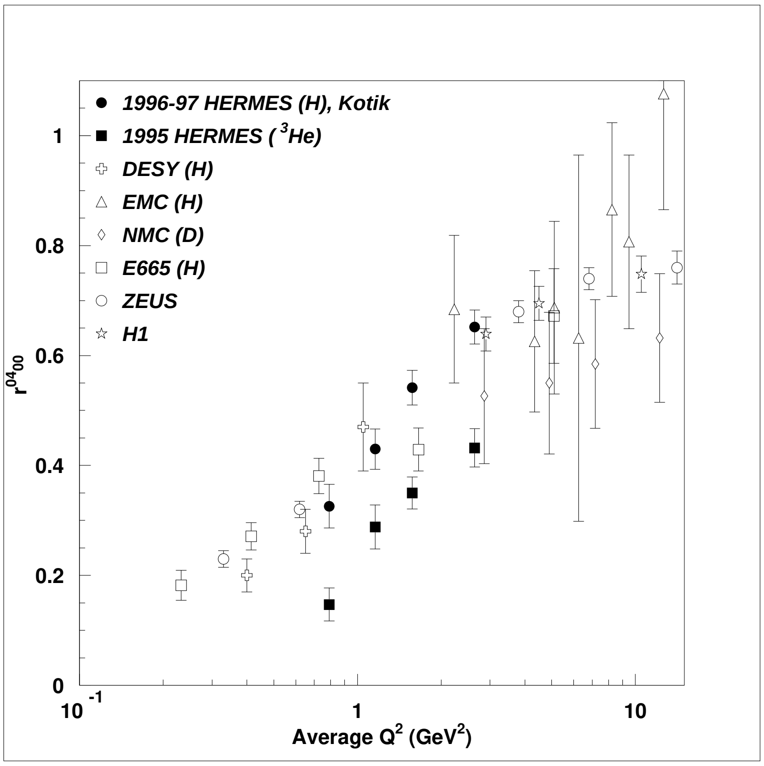

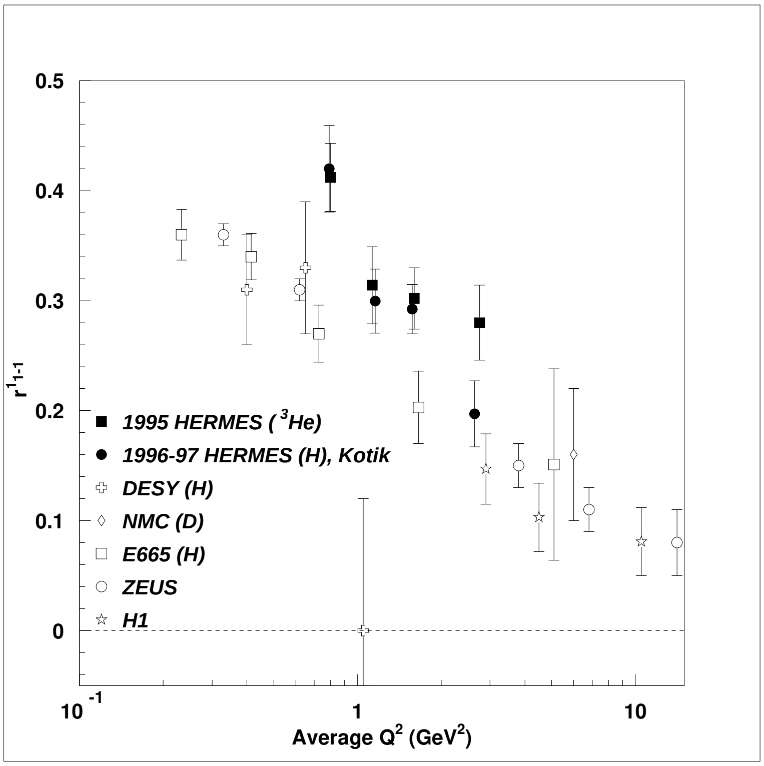

Figure 5.7: Experimental values of r^{04}_{00} (top) and r^1_{1-1} compared to the world data. Only statistical uncertainties are included.

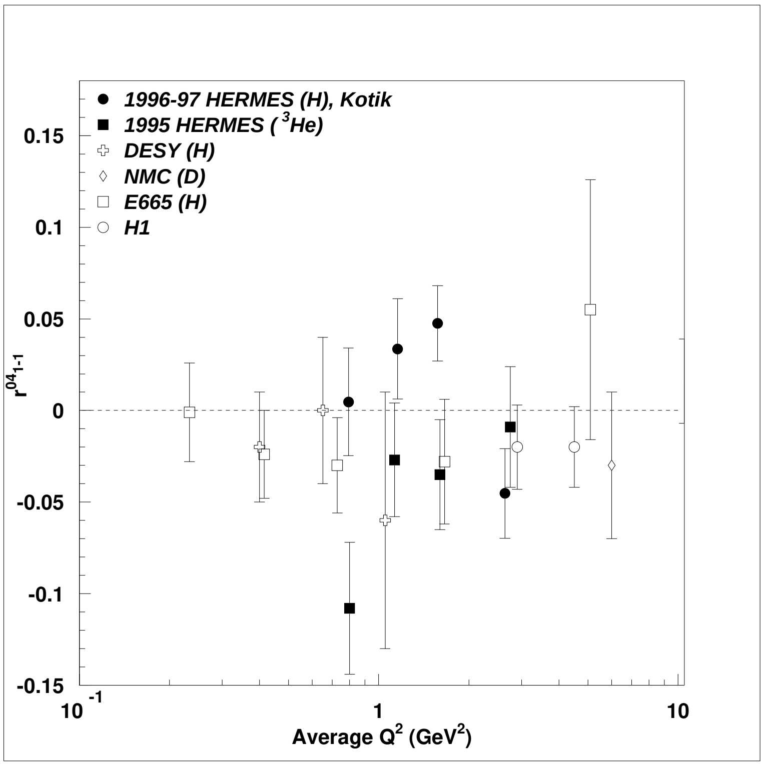

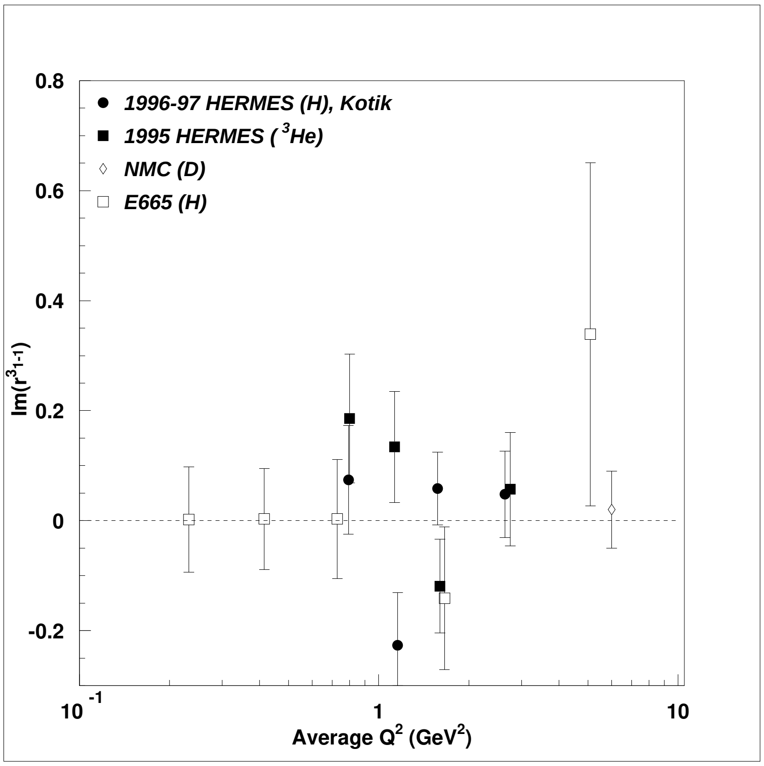

Figure 5.8: Experimental values of r^{04}_{1-1} (top) and Im r^3_{1-1} compared to the world data. Only statistical uncertainties are included.

predicted by SCHC. Results for $\mathrm{Tr}(r^8)$ (Fig. **??**) also agree with SCHC. World results of $\mathrm{Tr}(r^5)$ (Fig. 5.9) are characterised by their generally positive values. HERMES results are also generally positive and disagree with zero. This is an indication of a possible small SCHC violation. Very high uncertainty in δ (Fig. **??**) and lack of data from other experiments prevent any definitive conclusions about this parameter from being made.

Assuming SCHC, it is possible to calculate R from (5.14). The results of these calculations are displayed in Table 5.16. As Fig. 5.11 illustrates, the values of R agree with the world data.

$\overline{\langle Q^2 \rangle}$, GeV^2	$\overline{\langle \epsilon \rangle}$	R
0.79	0.768	0.63 ± 0.11
1.12	0.833	0.90 ± 0.14
1.57	0.826	1.43 ± 0.18
2.64	0.803	2.33 ± 0.32

Table 5.16: Calculated values of R.

Once the matrix elements have been determined, it is possible to compare the experimental angular distributions to the theoretically predicted distributions given by (2.66–2.69). Since not all diffractive ρ^0 events fall within the acceptance of the detector, it is necessary to correct for the acceptance by multiplying the number of data events D_i in each of the 20 bins i in each angular distribution by the *acceptance correction* factor c_i to obtain the corrected number of events D'_i

$$D'_i = c_i D_i \ . \tag{5.34}$$

For a given bin, c_i is calculated as the ratio between the numbers of appropriately normalised generated G_i and reconstructed R_i BMC events in the appropriate

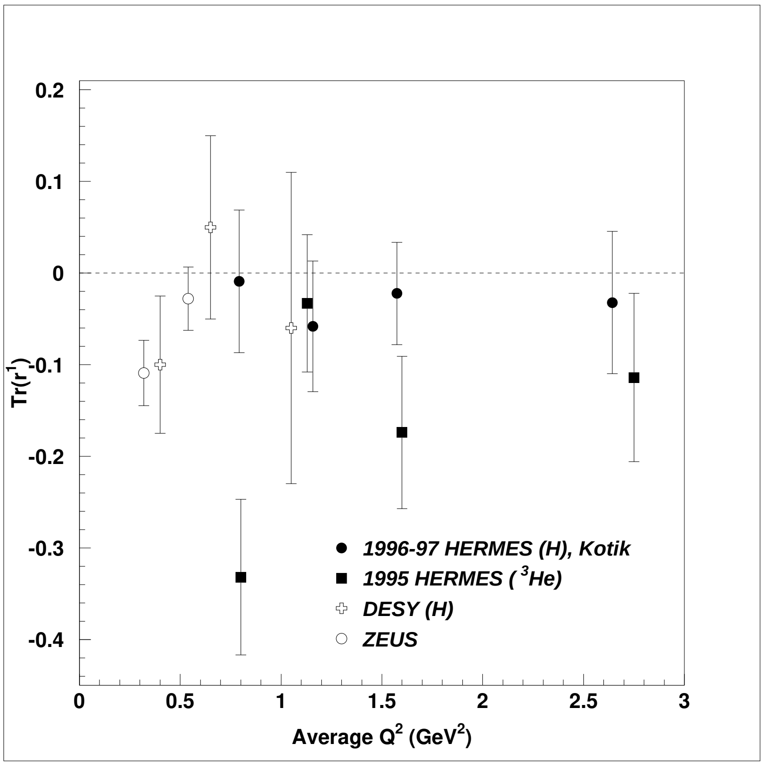

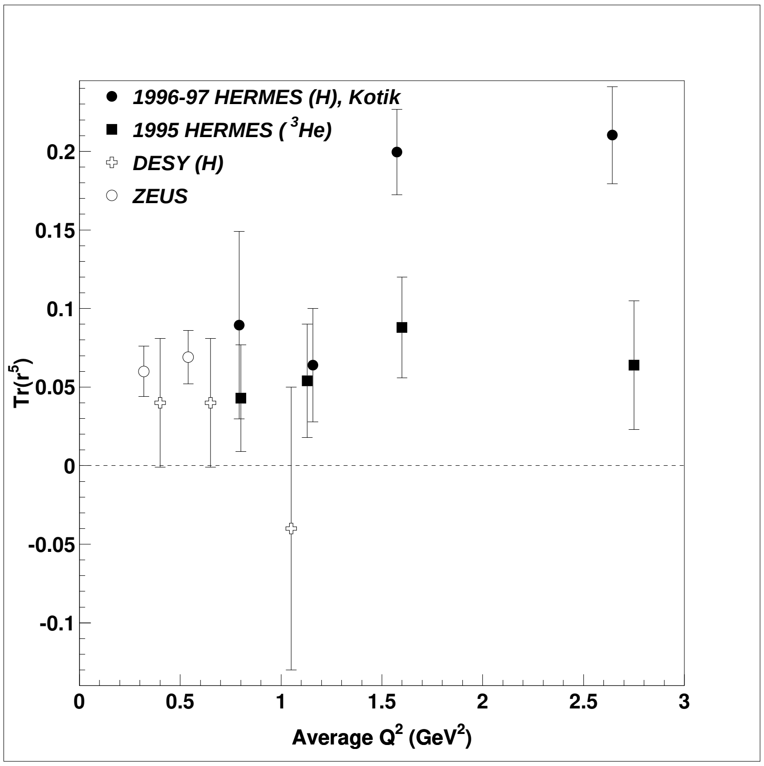

Figure 5.9: Experimental values of $\mathrm{Tr}(r^1)$ (top) and $\mathrm{Tr}(r^5)$ compared to the world data. Only statistical uncertainties are included.

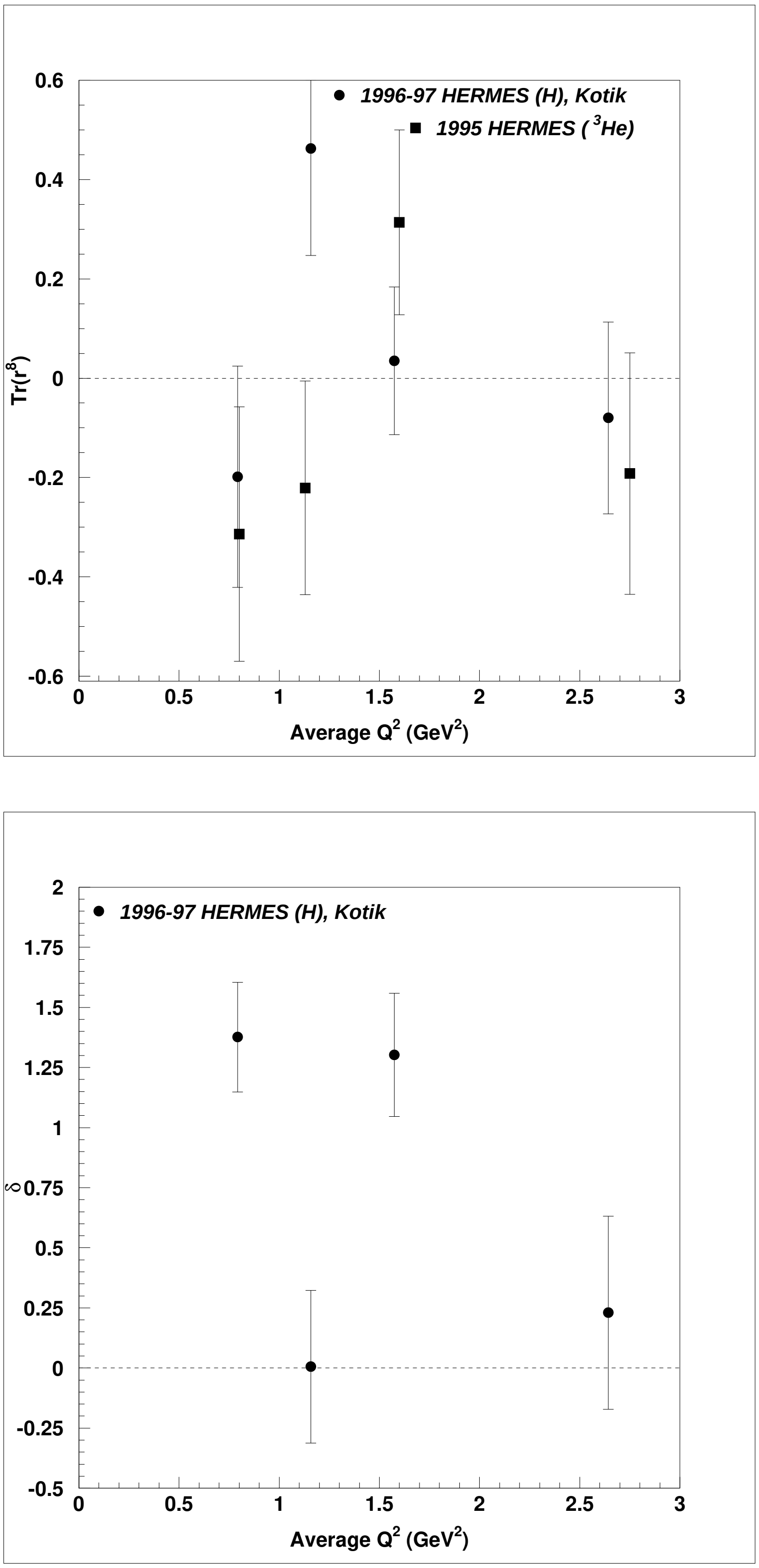

Figure 5.10: Experimental values of $\mathrm{Tr}(r^8)$ (top) and δ compared to the world data. Only statistical uncertainties are included.

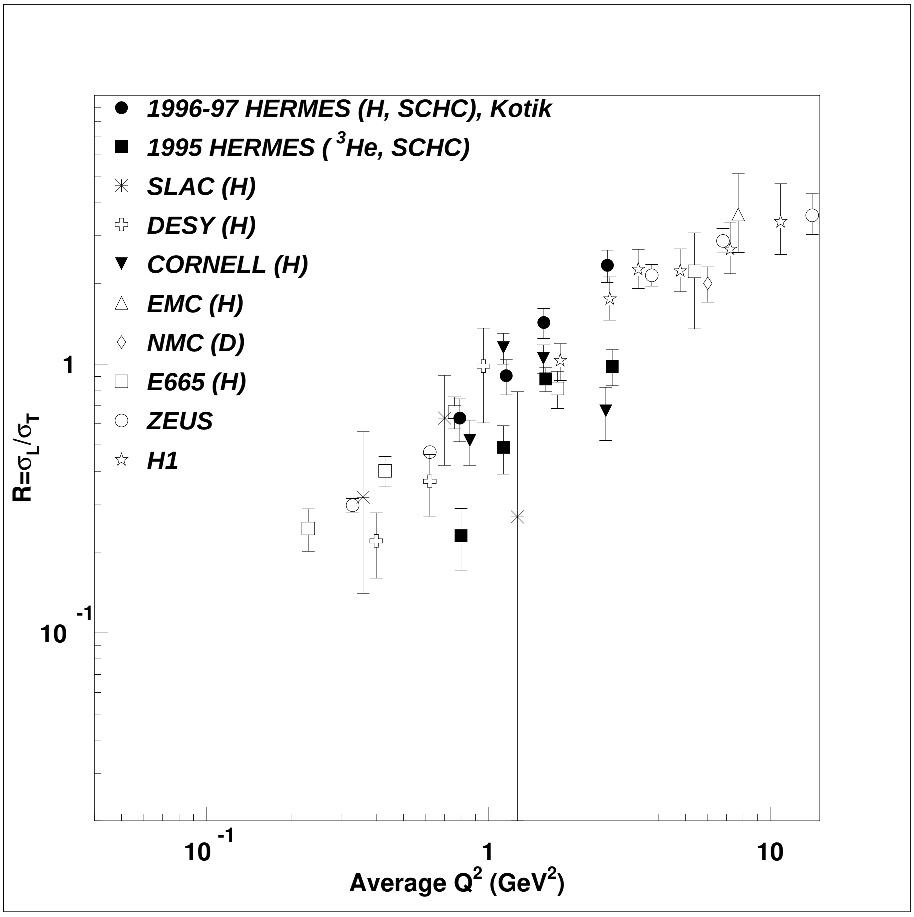

Figure 5.11: Experimental values of R. Values from the Cornell group are available in [53]. Eqn. (5.14), based on SCHC, was used in calculations of R where indicated.

bin. To obtain angular distributions of the generated BMC events, the sample of raw BMC events is subjected to the Q^2 cut only to restrict events to the Q^2 bin of interest. However, the recontstructed events are subjected to all kinematic cuts normally imposed. With the determined spin density matrix elements, both raw and reconstructed events are assigned weights according to Eqn. (5.19). With such weighting, the reconstructed BMC distributions closely resemble the experimental data distributions, whereas the raw BMC events simulate the shape of the distributions undisturbed by the detector. Accordingly, the correction factors are

$$c_i = \frac{G_i}{R_i} \ . \tag{5.35}$$

As a typical example, the acceptance-corrected angular distributions are plotted for the polarised 1997 set of data in Figs. 5.12 – 5.15. The experimental $\cos\theta$, ϕ and Φ distributions are in good agreement with the theoretically-predicted distributions. Moreover, the ϕ distributions in all four Q^2 bins are quite flat, and agree with the SCHC prediction of $W(\phi) = \frac{1}{2\pi} = 0.1592$. By contrast, the Φ distributions agree with the SCHC prediction of $W(\Phi) = \frac{1}{2\pi}$ only in bin Q1. The fact that the acceptance-corrected experimental Φ distributions agree well with the theoretically-predicted general shape, but disagree with SCHC, is a strong evidence for violation of SCHC. The experimental $\cos\psi$ distributions closely agree with the shapes given by Eqn. (2.69) in bins Q1, Q2 and Q3, and not so closely in Q4. Since (2.69) is based on the assumption of SCHC, the disagreement is attributed to the violation of SCHC.

5.8 Systematic Uncertainty

In the course of the SDME study of the ρ^0 mesons produced at HERMES with the ^{3}He target in 1995 [42], systematic uncertainty sources were investigated. Although the numerical values of some contributions to the systematic uncertainty for the ^{1}H results are expected to be different, the sources of the systematic uncertainty are expected to be the same. The following are the possible sources of the systematic error:

- Geometric acceptance. Found to be the dominant source of the systematic uncertainty at small Q^2.

- Background normalisation cut. The effects of lowering the ΔE normalisation cut of 3.9 GeV need to be studied. As plots in Fig. 5.4 demonstrate, the number of normalised DIS HMC events exceeds the number of data events in the region immediately to the left of 3.9 GeV. This is contrary to the expectation that the number of data events should slightly exceed (due to the presence of diffractive events) or at least be the same as the number of DIS HMC events in that region.

- Background subtraction. This contribution refers to the choice of background subtraction cuts in ΔE and t'

- Radiative effects due to interactions of the scattered positrons with the detector material.

- The assumptions (5.15 – 5.18). These may also not be strictly correct.

Further work on systematic errors is needed to finalise the preliminary results presented in this thesis.

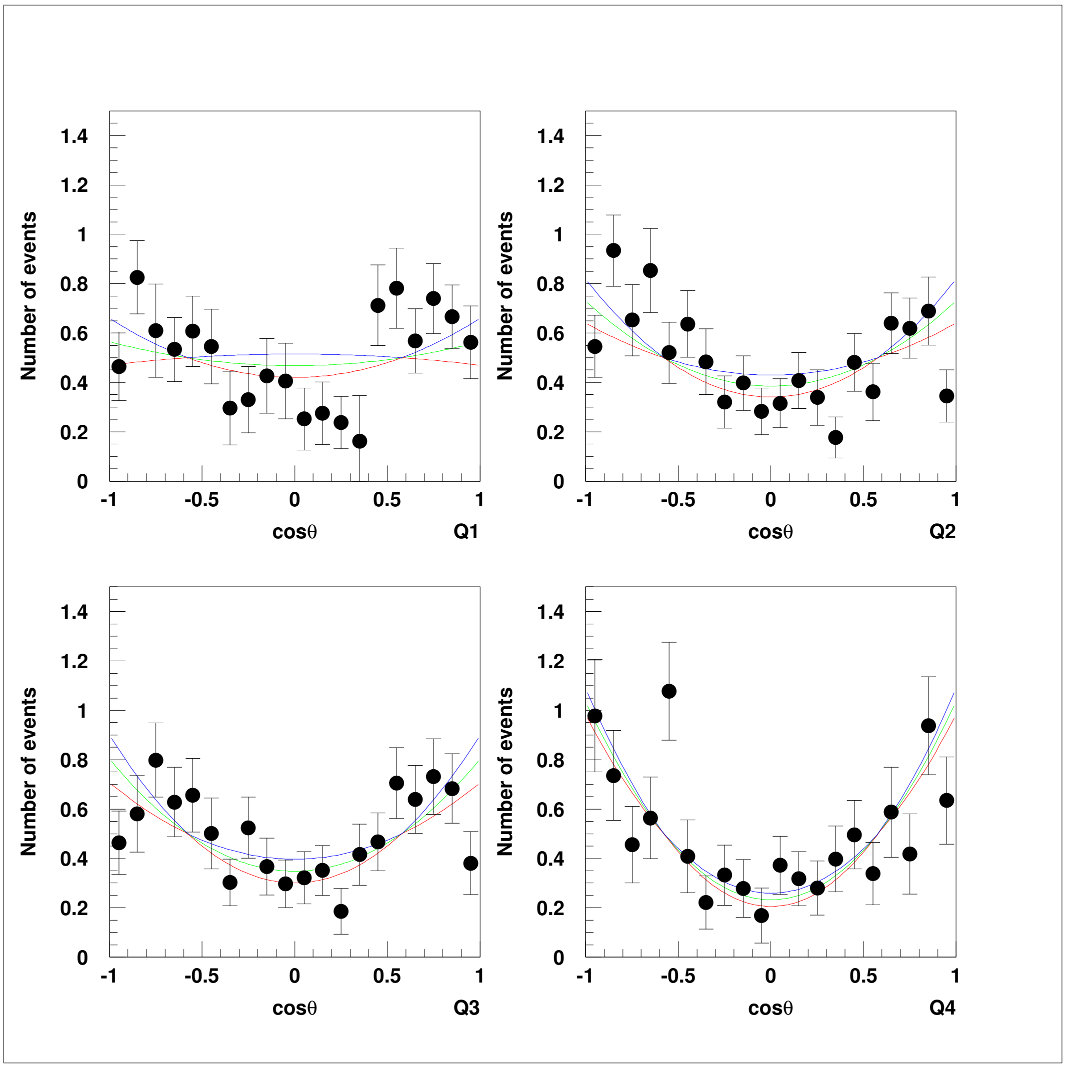

Figure 5.12: Acceptance-corrected $\cos\theta$ distributions for polarised 1997 data. The three curves represent $W(\cos\theta) - \delta W(\cos\theta)$, $W(\cos\theta)$ and $W(\cos\theta) + \delta W(\cos\theta)$; with $W(\cos\theta)$ given by (2.66).

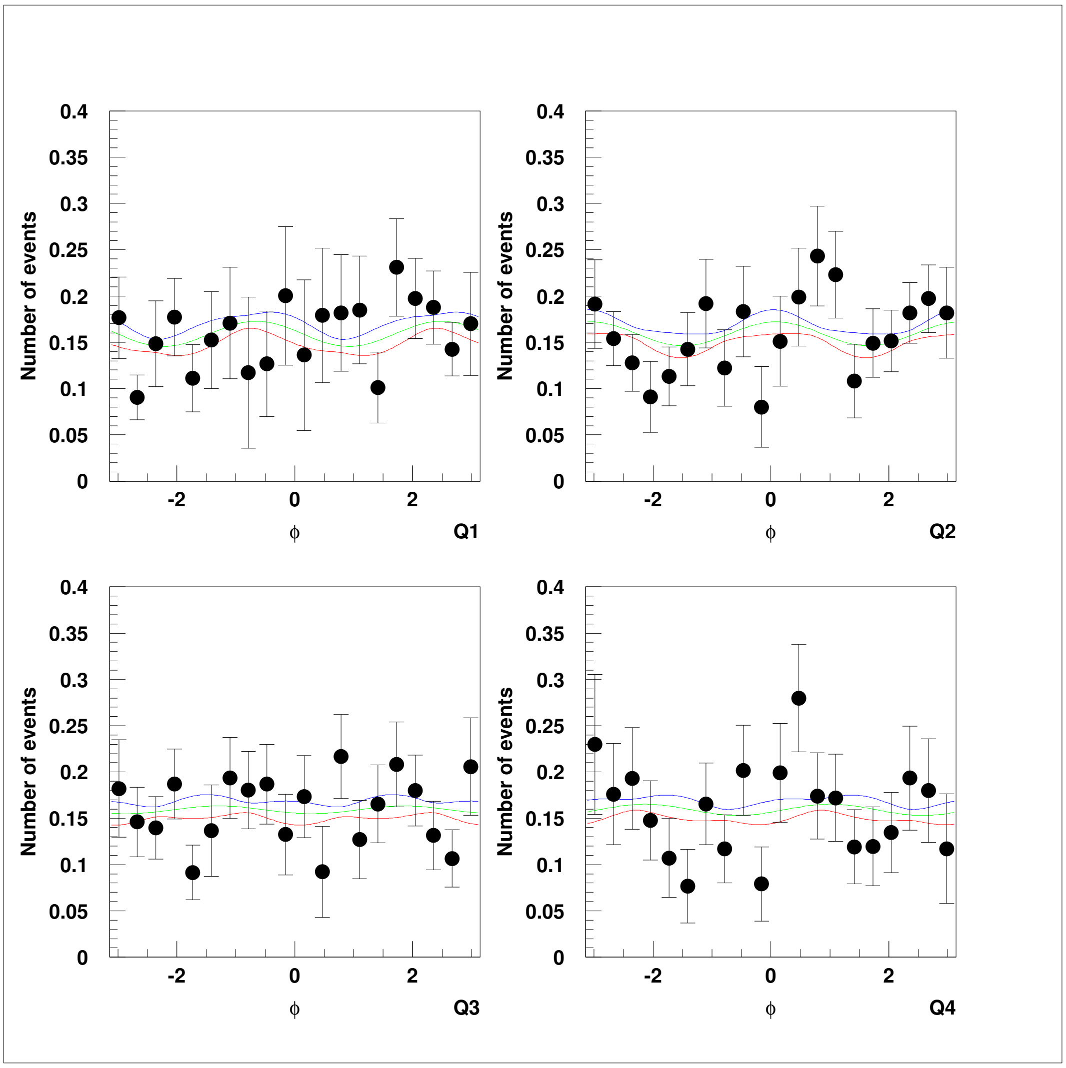

Figure 5.13: Acceptance-corrected ϕ distributions for polarised 1997 data. The three curves represent $W(\phi) - \delta W(\phi)$, $W(\phi)$ and $W(\phi) + \delta W(\phi)$; with $W(\phi)$ given by (2.67). SCHC predicts that $W(\phi) = 0.159$.

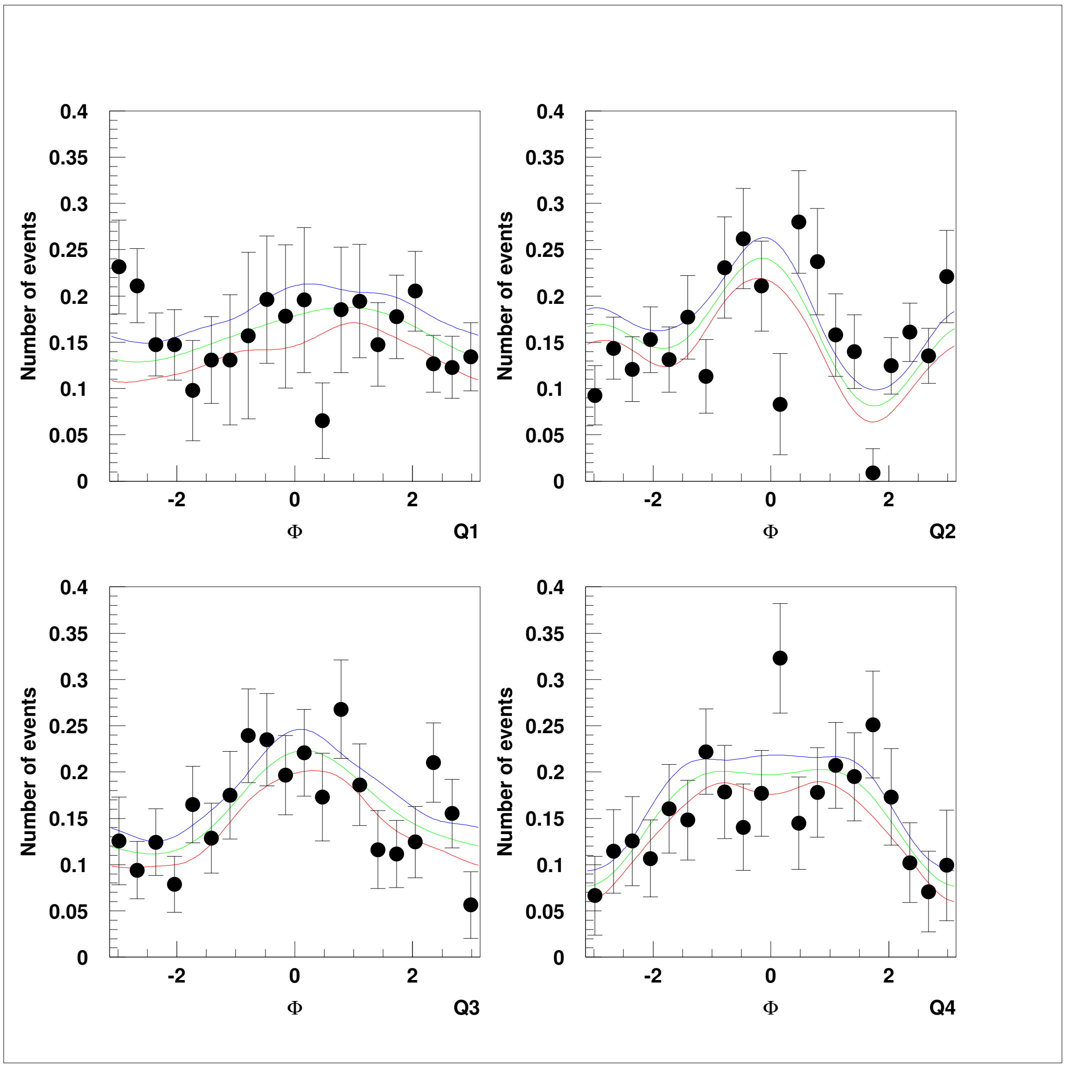

Figure 5.14: Acceptance-corrected Φ distributions for polarised 1997 data. The three curves represent $W(\Phi) - \delta W(\Phi)$, $W(\Phi)$ and $W(\Phi) + \delta W(\Phi)$; with $W(\Phi)$ given by (2.68). SCHC predicts that $W(\Phi) = 0.159$.

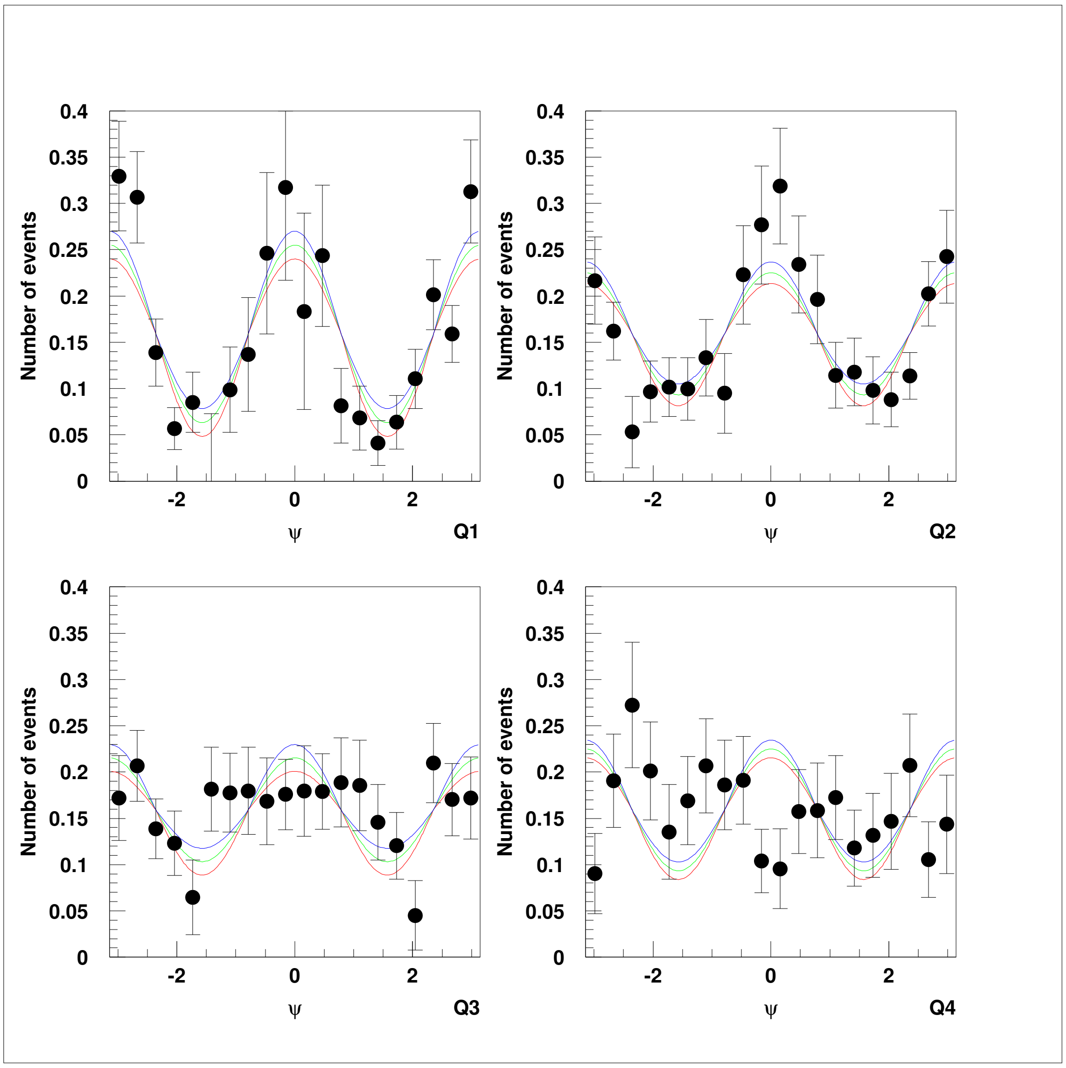

Figure 5.15: Acceptance-corrected ψ distributions for polarised 1997 data. The three curves represent $W(\psi) - \delta W(\psi)$, $W(\psi)$ and $W(\psi) + \delta W(\psi)$; with $W(\psi)$ given by (2.69). Note that (2.69) is based on the assumption of SCHC.

Chapter 6

Conclusion

In this study of diffractive ρ^0 meson leptoproduction, the relationship between helicities of the virtual photon and the ρ^0 was investigated by determining the Spin Density Matrix Elements. Specifically, the analysis focused on testing S-Channel Helicity Conservation and Natural Parity Exchange. The study was performed on the 1996 and 1997 HERMES data, obtained from collisions of the 27.5 GeV positron beam with a fixed ^{1}H target, by analysing the angular distribution of decay products of the ρ^0 . The analysis spanned a kinematic range of 0.50 GeV$^2 \leq Q^2 \leq$ 4.00 GeV^2 and 3.8 GeV $\leq W \leq$ 6.5 GeV.

By partially assuming SCHC, values of the matrix elements r^{04}_{00}, r^{1}_{1-1}, r^{04}_{1-1}, $\mathrm{Im}(r^3_{1-1})$, $\mathrm{Tr}(r^1)$, $\mathrm{Tr}(r^5)$, and $\mathrm{Tr}(r^8)$ were determined. The results for $\mathrm{Im}(r^3_{1-1})$, $\mathrm{Tr}(r^1)$ and $\mathrm{Tr}(r^8)$ agree with SCHC. The agreement of r^{04}_{1-1} with SCHC can only be established after a systematic uncertainty study. The generally positive behaviour of $\mathrm{Tr}(r^5)$ indicates a degree of violation of SCHC. In most instances, the agreement of the SDMEs with the world data for hydrogen in the kinematic range of interest is good, provided enough world data are available. However, values of r^1_{1-1} are higher than expected, but are consistent with earlier HERMES results for the ^{3}He target published in [42]. Disagreement is observed between the values r_{00}^{04} extracted in this study and those published in [42]; the presence of coherent effects in the ^{3}He nucleus may be a possible, yet not certain, explanation. Eqn. (5.29), based on the assumption of both SCHC and NPE, is obeyed in two Q^2 bins out of four. Since there are indications of the SCHC violation, it is impossible to attribute the disagreement from (5.29) to either the violation of SCHC, or the violation of NPE, or both.

A careful evaluation of all possible sources of systematic uncertainty is nessessary to assess the validity of the presented method of the SDME extraction.

Appendix A

The Dirac Matrices

Dirac matrices are 4×4 matrices defined as

$$\gamma^0 = \begin{pmatrix} \mathbb{1} & \mathbb{O} \\ \mathbb{O} & -\mathbb{1} \end{pmatrix} , \quad \gamma^i = \begin{pmatrix} \mathbb{O} & \sigma^i \\ -\sigma^i & \mathbb{O} \end{pmatrix} , \quad i = 1, 2, 3 \; , \tag{A.1}$$

where $\mathbb{1}$ is a 2×2 identity matrix, $\mathbb{O}$ is a 2×2 null matrix, and σ^i are the 2×2 Pauli spin matrices:

$$\sigma^1 = \begin{pmatrix} 0 & 1 \\ 1 & 0 \end{pmatrix} , \quad \sigma^2 = \begin{pmatrix} 0 & -i \\ i & 0 \end{pmatrix} , \quad \sigma^3 = \begin{pmatrix} 1 & 0 \\ 0 & -1 \end{pmatrix} \; . \tag{A.2}$$

Appendix B

Decomposition of γ^* spin density matrix

In equation 2.50, the Σ matrices are given by

$$\Sigma^0 = \begin{pmatrix} 1 & 0 & 0 \\ 0 & 0 & 0 \\ 0 & 0 & 1 \end{pmatrix} \quad \Sigma^1 = \begin{pmatrix} 0 & 0 & 1 \\ 0 & 0 & 0 \\ 1 & 0 & 0 \end{pmatrix} \quad \Sigma^2 = \begin{pmatrix} 0 & 0 & -i \\ 0 & 0 & 0 \\ i & 0 & 0 \end{pmatrix}$$
$$\Sigma^3 = \begin{pmatrix} 1 & 0 & 0 \\ 0 & 0 & 0 \\ 0 & 0 & -1 \end{pmatrix} \quad \Sigma^4 = \begin{pmatrix} 0 & 0 & 0 \\ 0 & 2 & 0 \\ 0 & 0 & 0 \end{pmatrix} \quad \Sigma^5 = \frac{1}{\sqrt{2}} \begin{pmatrix} 0 & 1 & 0 \\ 1 & 0 & -1 \\ 0 & -1 & 0 \end{pmatrix}$$
$$\Sigma^6 = \frac{1}{\sqrt{2}} \begin{pmatrix} 0 & -i & 0 \\ i & 0 & i \\ 0 & -i & 0 \end{pmatrix} \quad \Sigma^7 = \tfrac{1}{\sqrt{2}} \begin{pmatrix} 0 & 1 & 0 \\ 1 & 0 & 1 \\ 0 & 1 & 0 \end{pmatrix} \quad \Sigma^8 = \frac{1}{\sqrt{2}} \begin{pmatrix} 0 & -i & 0 \\ i & 0 & -i \\ 0 & i & 0 \end{pmatrix} \tag{B.1}$$

with the vector $\tilde{\Pi}$ given by

$$\tilde{\Pi} = \begin{pmatrix} 1 \\ -\epsilon\cos 2\Phi \\ -\epsilon\sin 2\Phi \\ \frac{2m}{Q}(1-\epsilon)P_0 \\ \epsilon \\ \sqrt{2\epsilon(1+\epsilon)}\cos\Phi \\ \sqrt{2\epsilon(1+\epsilon)}\sin\Phi \\ \frac{2m}{Q}(1-\epsilon)(P_1\cos\Phi + P_2\sin\Phi) \\ \frac{2m}{Q}(1-\epsilon)(P_1\sin\Phi - P_2\cos\Phi) \end{pmatrix}, \; M_e \ll E_e. \tag{B.2}$$

Appendix C

Decomposition of ρ^0 Spin Density Matrix

Defining $R = \frac{\sigma_L}{\sigma_T}$ is the ratio of longitudinal to transverse components of the total cross section, it is now possible to write out vector Π in eqn. 2.53, which is similar, although not the same, as vector $\tilde{\Pi}$:

$$\Pi = \frac{1}{1+(\epsilon)R} \begin{pmatrix} 1 \\ -\epsilon\cos 2\Phi \\ -\epsilon\sin 2\Phi \\ \frac{2m}{Q}(1-\epsilon)P_0 \\ \epsilon R \\ \sqrt{2\epsilon R(1+\epsilon)}\cos\Phi \\ \sqrt{2\epsilon R(1+\epsilon)}\sin\Phi \\ \frac{2m}{Q}(1-\epsilon)\sqrt{R}(P_1\cos\Phi + P_2\sin\Phi) \\ \frac{2m}{Q}(1-\epsilon)\sqrt{R}(P_1\sin\Phi - P_2\cos\Phi) \end{pmatrix}, \ M_e \ll E_e. \qquad \text{(C.1)}$$

Appendix D

Fit Quality Plots

Angular distributions of the experimental data and the optimised Monte Carlo model are compared in Figs. D.1—D.16. The optimised Monte Carlo datapoints are obtained by inserting the respective measured values of the spin density matrix elements into $W(\cos\theta,\ \phi,\ \Phi)$ described by Eqn. (5.19). Only statistical uncertainties are displayed. The plots thereby illustrate the fit quality case-by-case.

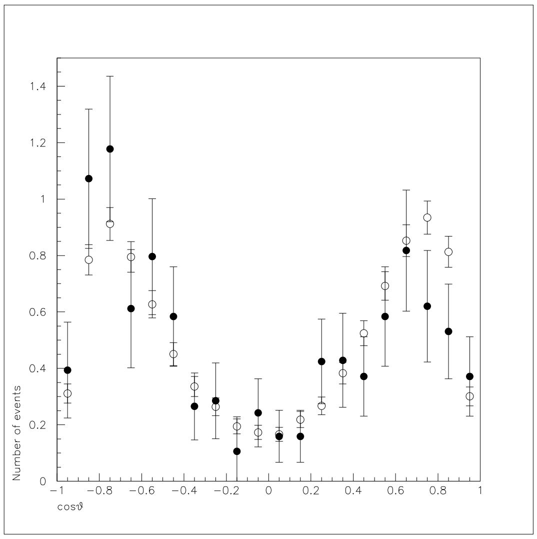

(a) Unpolarised 1996

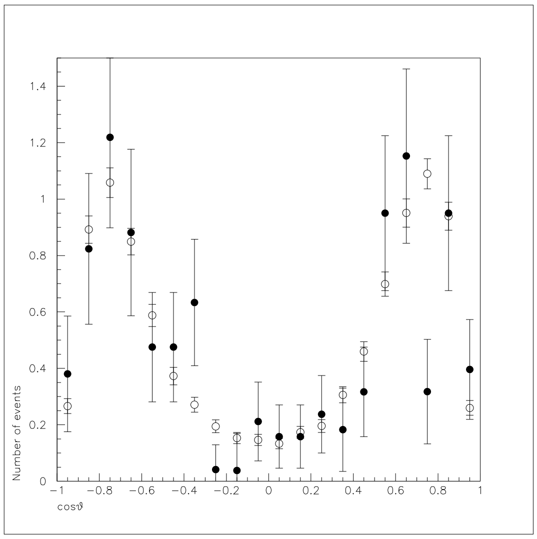

(b) Polarised 1996

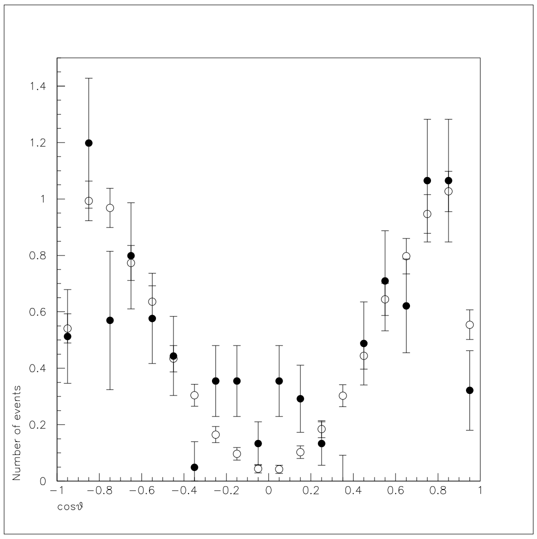

(c) Unpolarised 1997

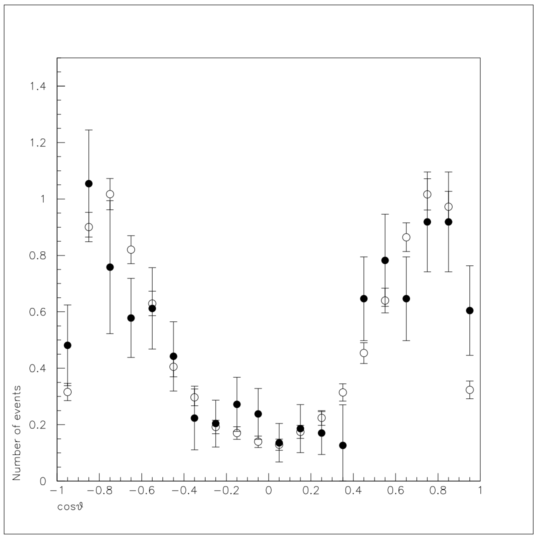

(d) Polarised 1997

Figure D.1: Comparison of the experimental distributions in $\cos\theta$ to the optimised Monte Carlo model for bin Q1. Filled and empty circles represent the data and the optimised Monte Carlo model, respectively.

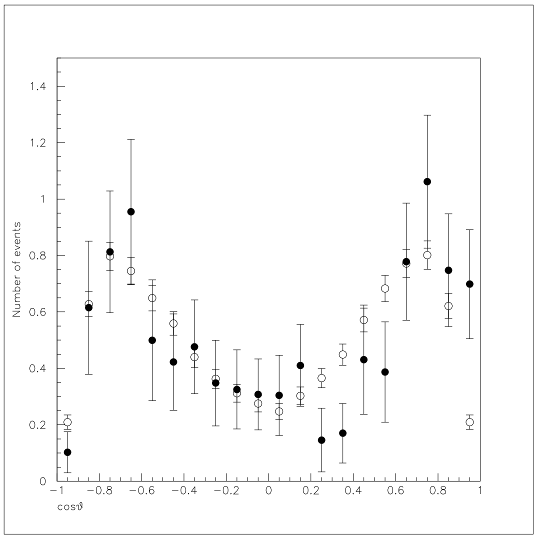

(a) Unpolarised 1996

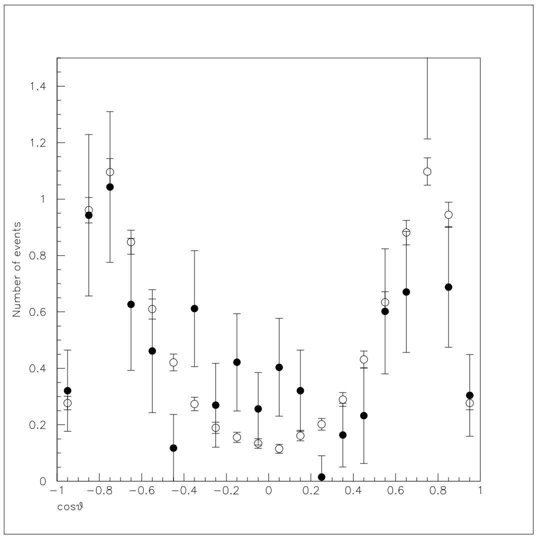

(b) Polarised 1996

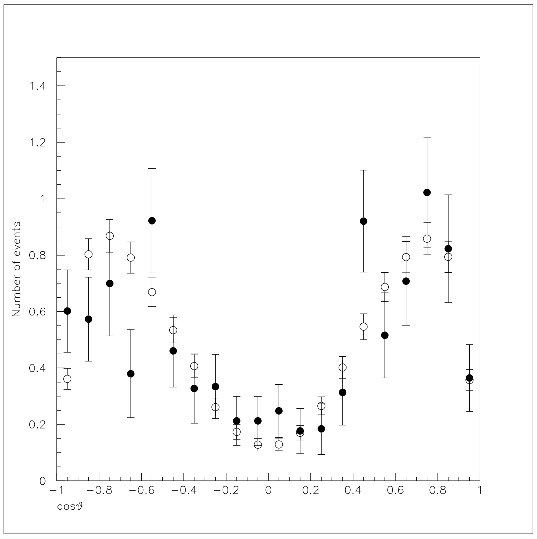

(c) Unpolarised 1997

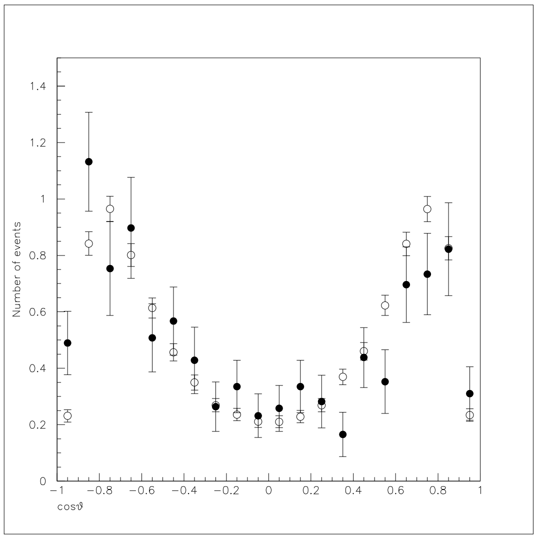

(d) Polarised 1997

Figure D.2: Comparison of the experimental distributions in $\cos\theta$ to the optimised Monte Carlo model for bin Q2. Filled and empty circles represent the data and the optimised Monte Carlo model, respectively.

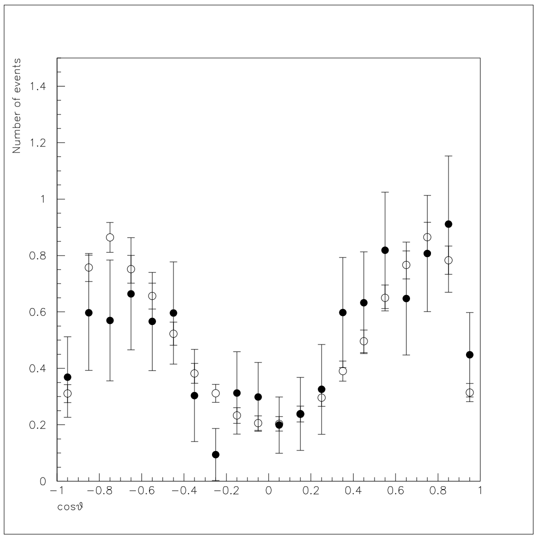

(a) Unpolarised 1996

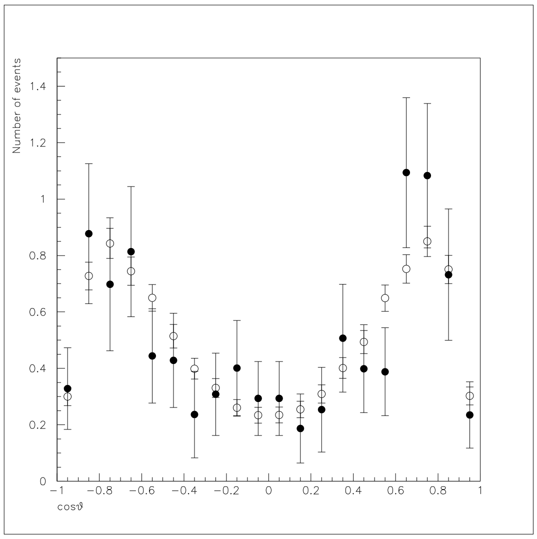

(b) Polarised 1996

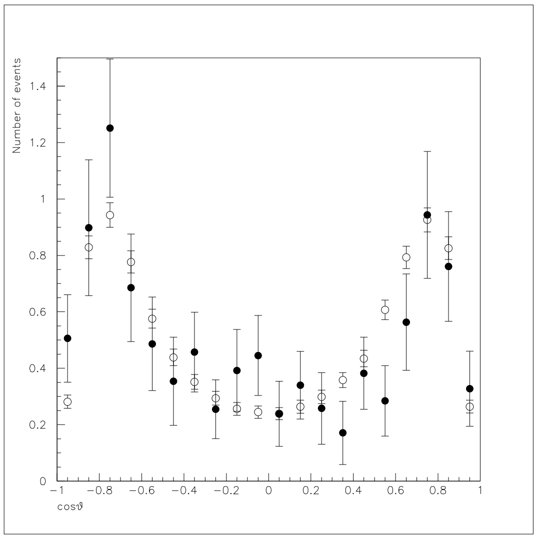

(c) Unpolarised 1997

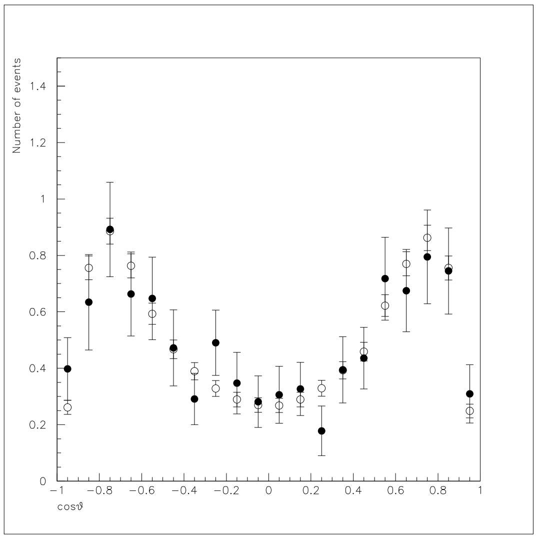

(d) Polarised 1997

Figure D.3: Comparison of the experimental distributions in $\cos\theta$ to the optimised Monte Carlo model for bin Q3. Filled and empty circles represent the data and the optimised Monte Carlo model, respectively.

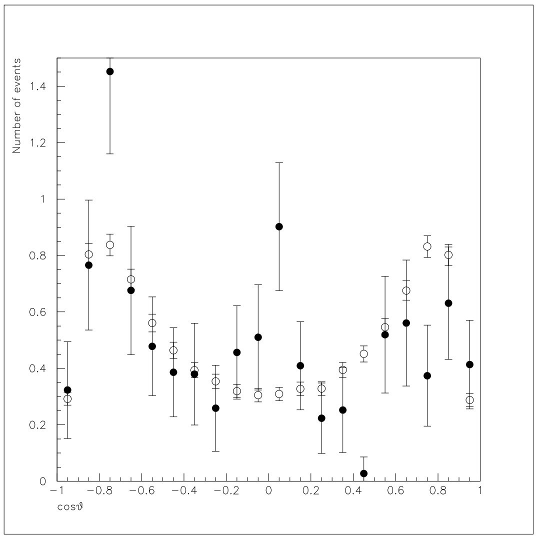

(a) Unpolarised 1996

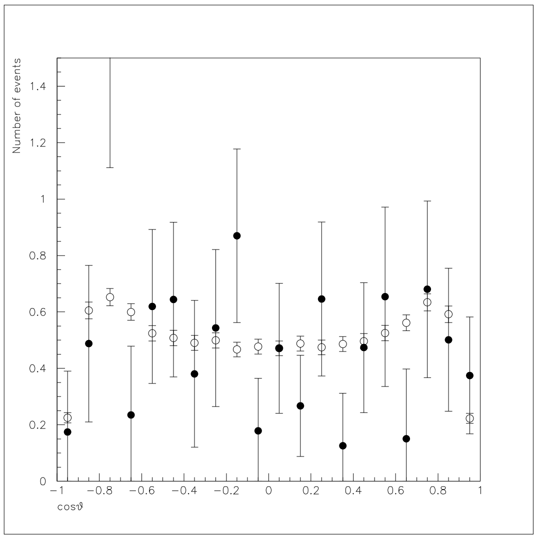

(b) Polarised 1996

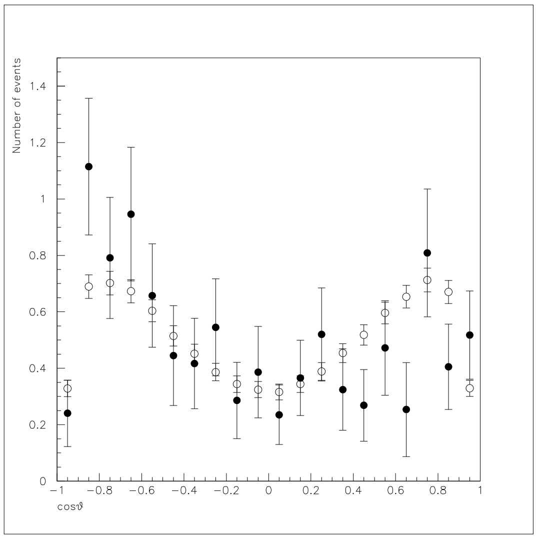

(c) Unpolarised 1997

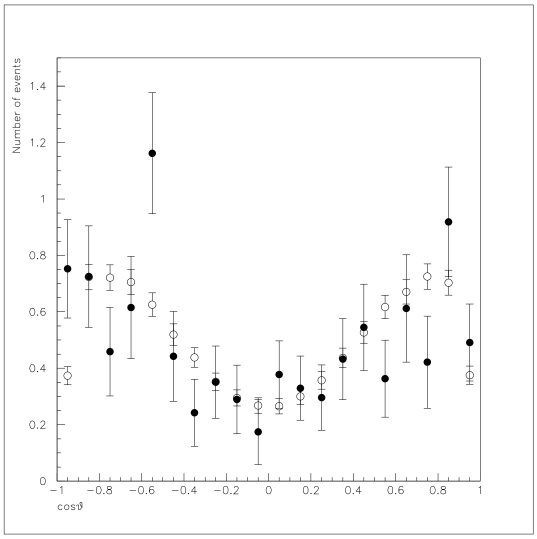

(d) Polarised 1997

Figure D.4: Comparison of the experimental distributions in $\cos\theta$ to the optimised Monte Carlo model for bin Q4. Filled and empty circles represent the data and the optimised Monte Carlo model, respectively.

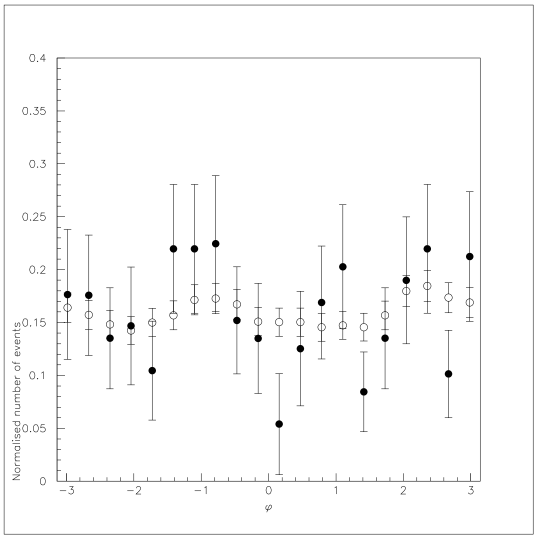

(a) Unpolarised 1996

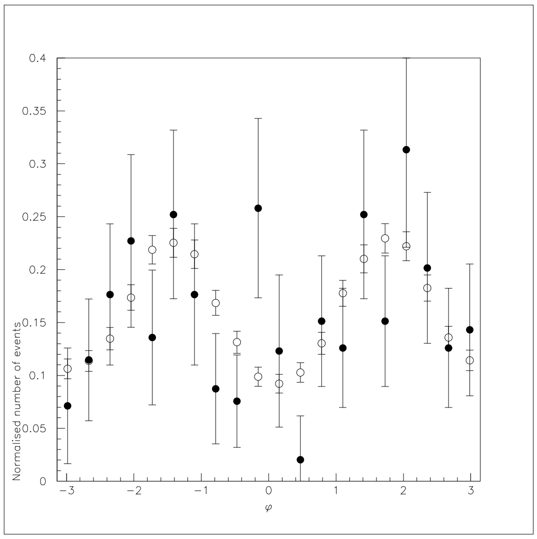

(b) Polarised 1996

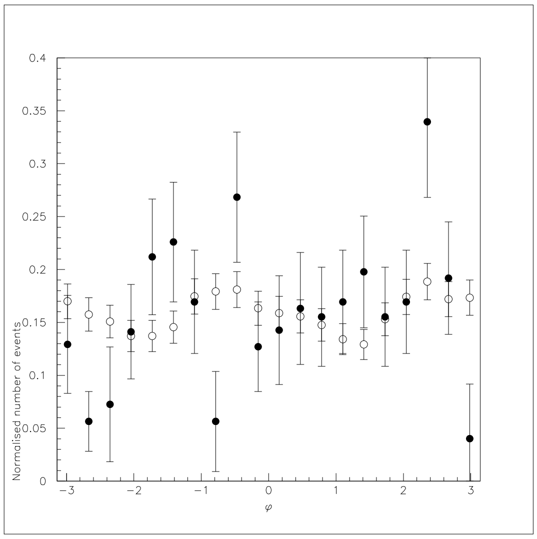

(c) Unpolarised 1997

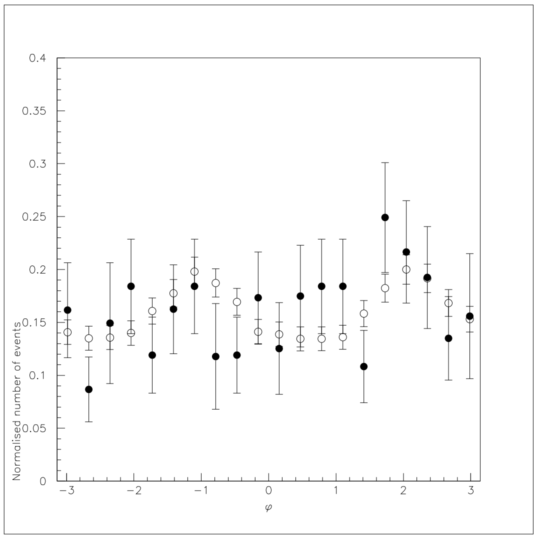

(d) Polarised 1997

Figure D.5: Comparison of the experimental distributions in ϕ to the optimised Monte Carlo model for bin Q1. Filled and empty circles represent the data and the optimised Monte Carlo model, respectively.

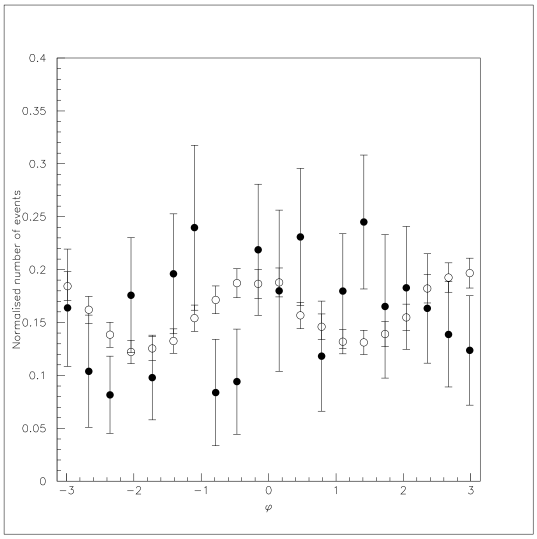

(a) Unpolarised 1996

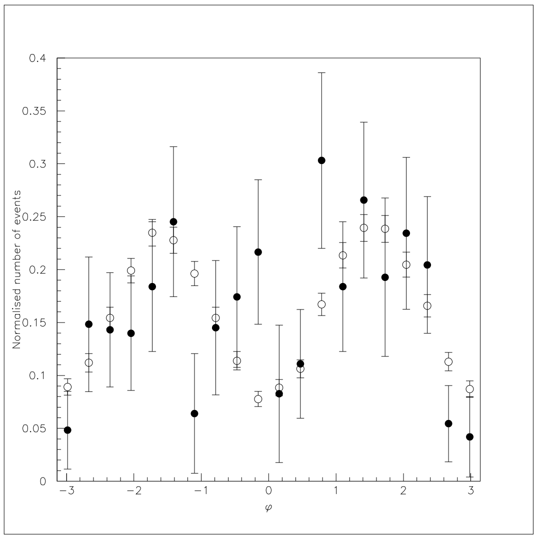

(b) Polarised 1996

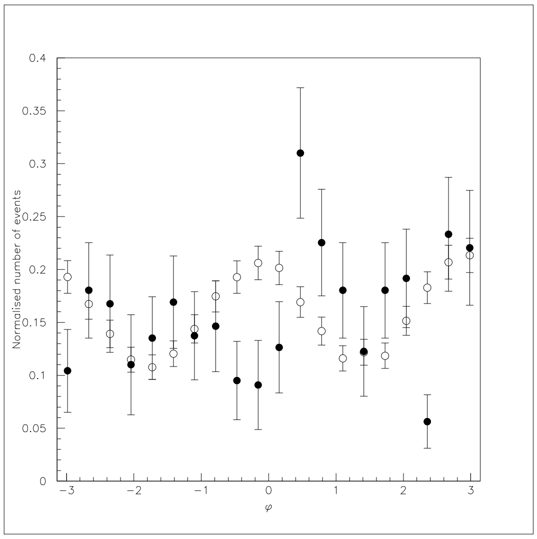

(c) Unpolarised 1997

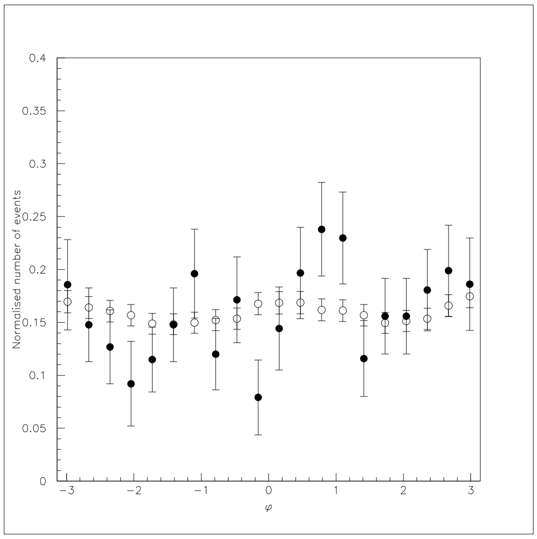

(d) Polarised 1997

Figure D.6: Comparison of the experimental distributions in ϕ to the optimised Monte Carlo model for bin Q2. Filled and empty circles represent the data and the optimised Monte Carlo model, respectively.

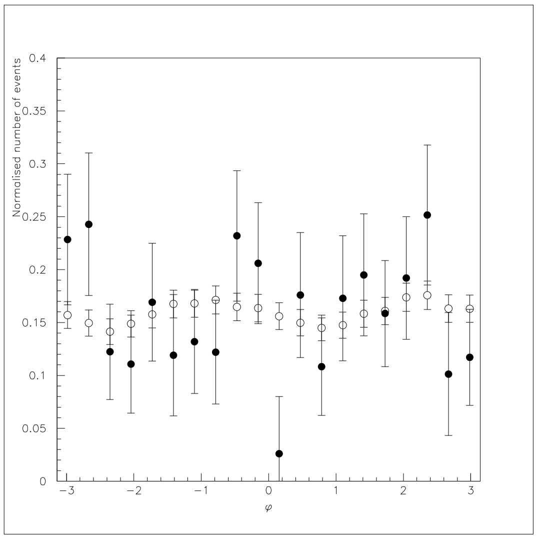

(a) Unpolarised 1996

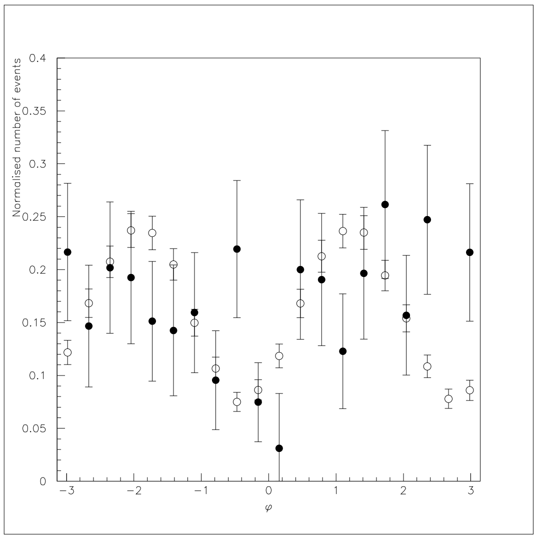

(b) Polarised 1996

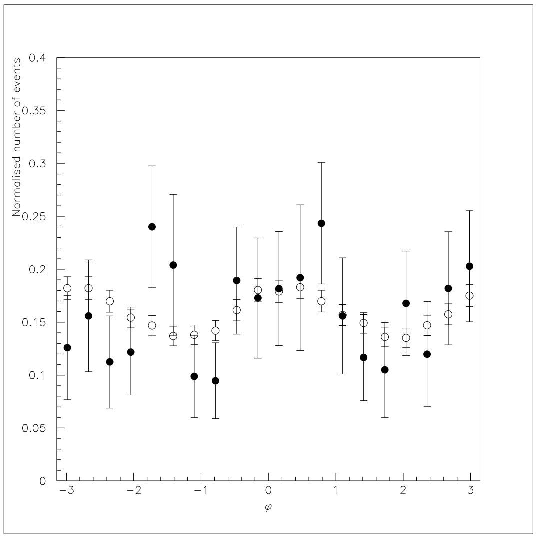

(c) Unpolarised 1997

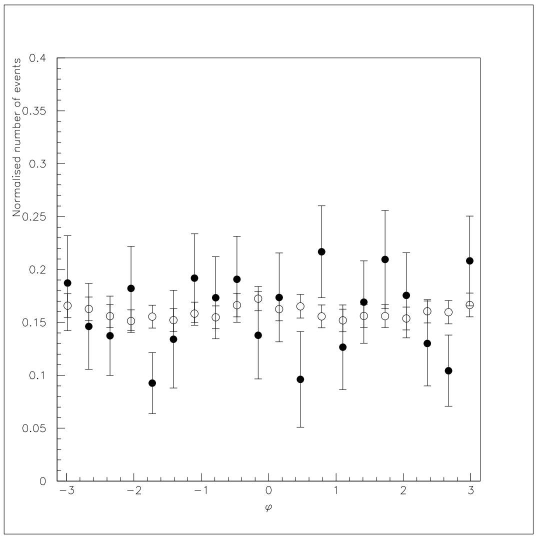

(d) Polarised 1997

Figure D.7: Comparison of the experimental distributions in ϕ to the optimised Monte Carlo model for bin Q3. Filled and empty circles represent the data and the optimised Monte Carlo model, respectively.

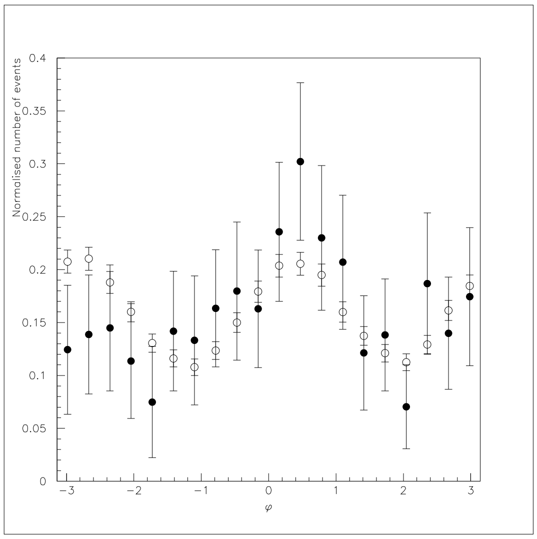

(a) Unpolarised 1996

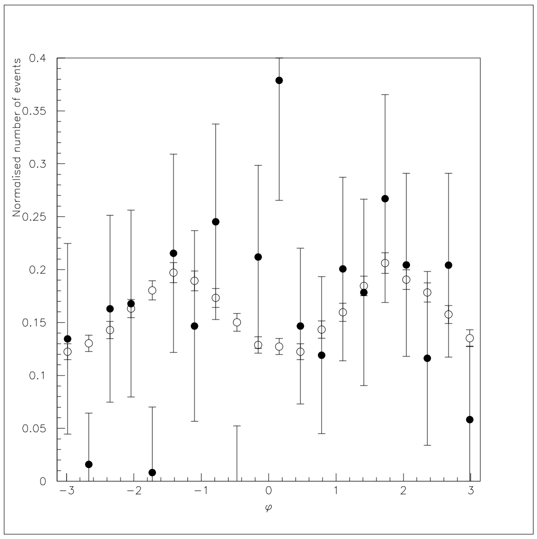

(b) Polarised 1996

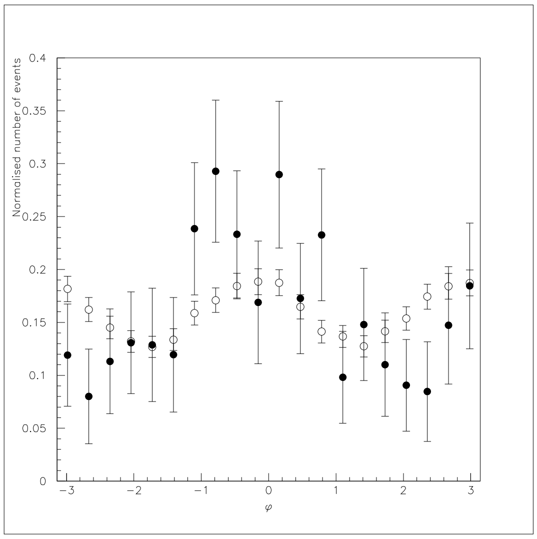

(c) Unpolarised 1997

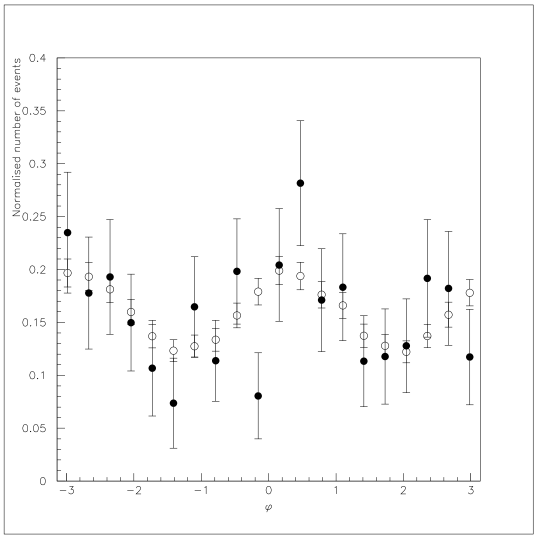

(d) Polarised 1997

Figure D.8: Comparison of the experimental distributions in ϕ to the optimised Monte Carlo model for bin Q4. Filled and empty circles represent the data and the optimised Monte Carlo model, respectively.

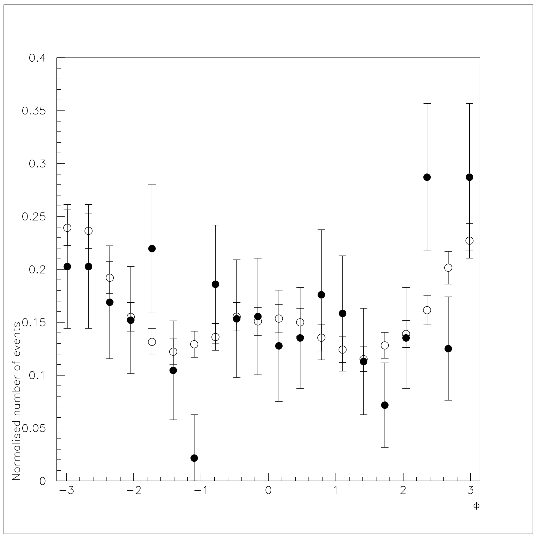

(a) Unpolarised 1996

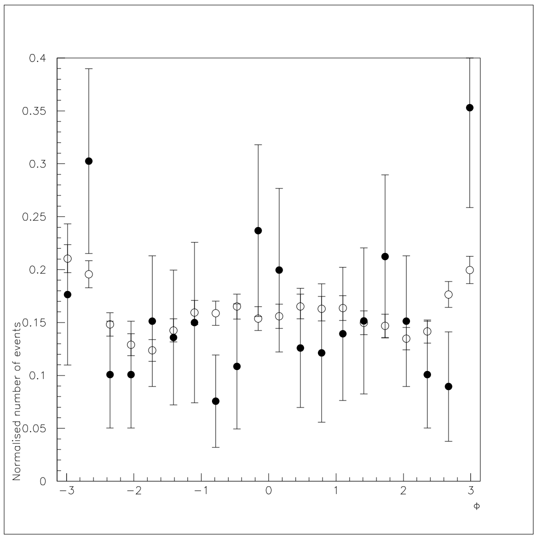

(b) Polarised 1996

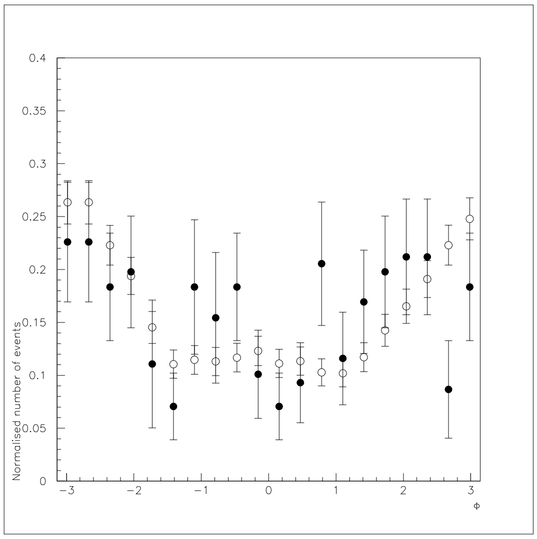

(c) Unpolarised 1997

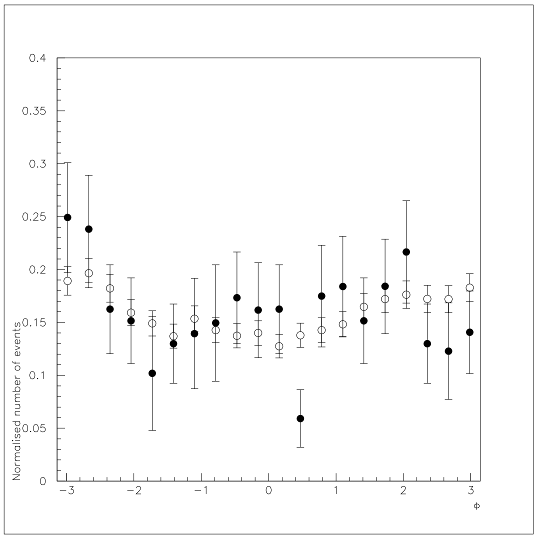

(d) Polarised 1997

Figure D.9: Comparison of the experimental distributions in Φ to the optimised Monte Carlo model for bin Q1. Filled and empty circles represent the data and the optimised Monte Carlo model, respectively.

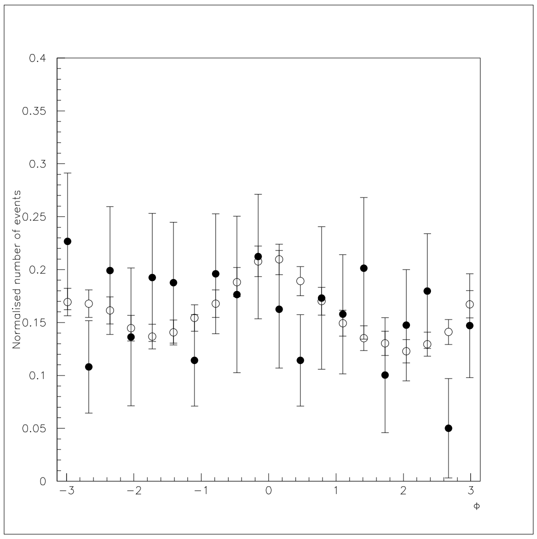

(a) Unpolarised 1996

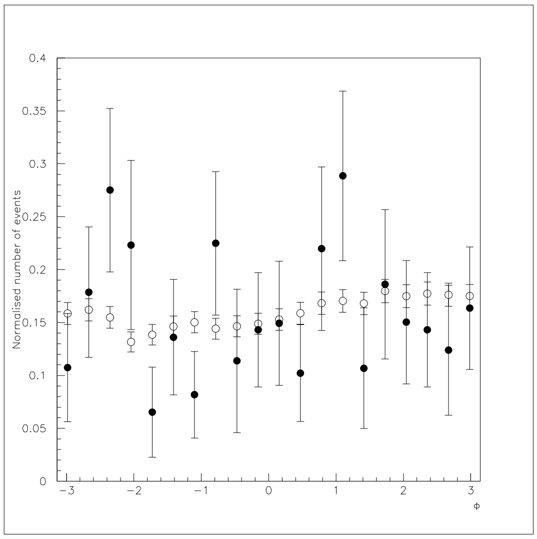

(b) Polarised 1996

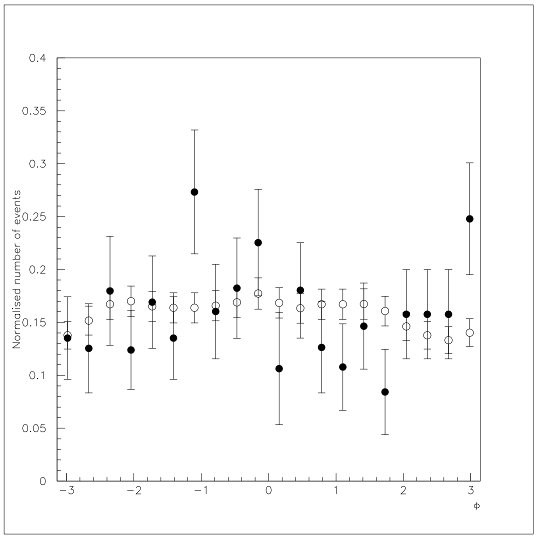

(c) Unpolarised 1997

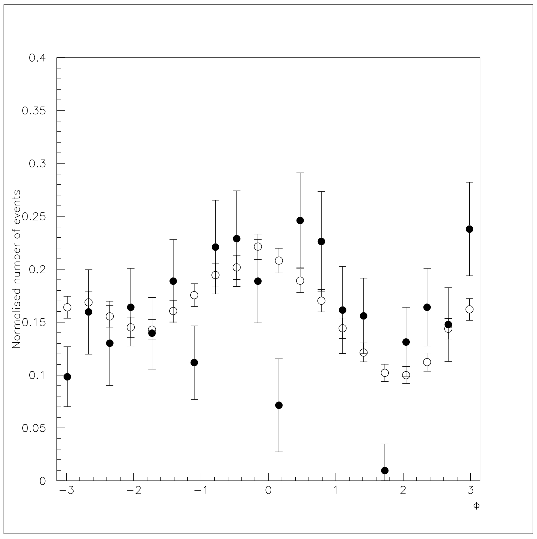

(d) Polarised 1997

Figure D.10: Comparison of the experimental distributions in Φ to the optimised Monte Carlo model for bin Q2. Filled and empty circles represent the data and the optimised Monte Carlo model, respectively.

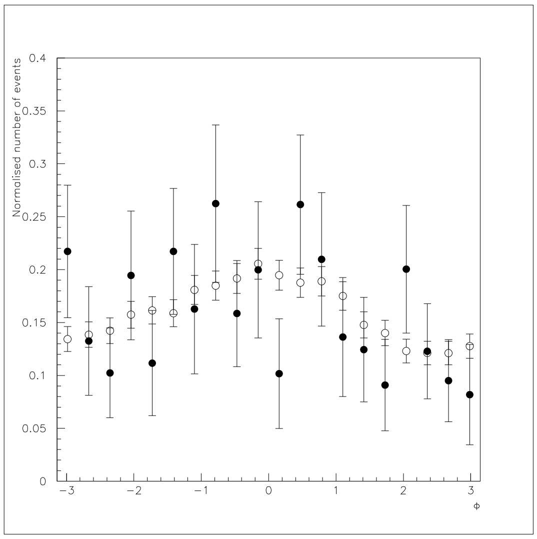

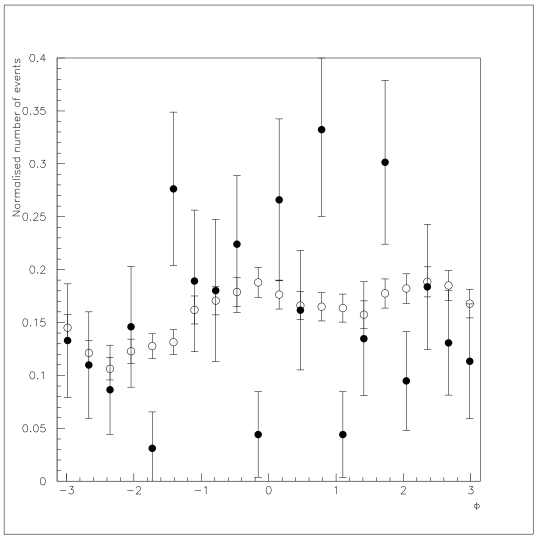

(a) Unpolarised 1996

(b) Polarised 1996

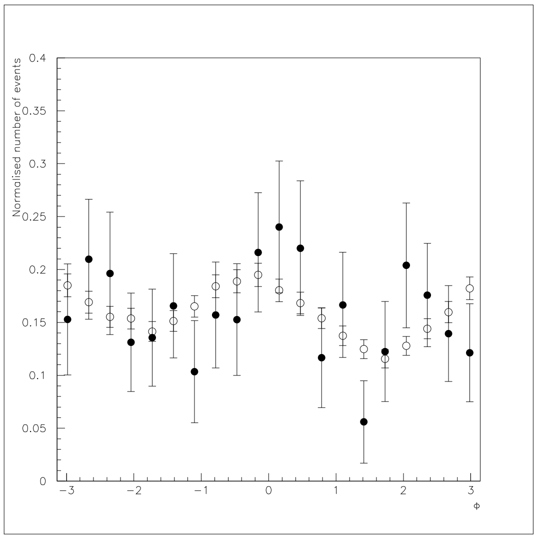

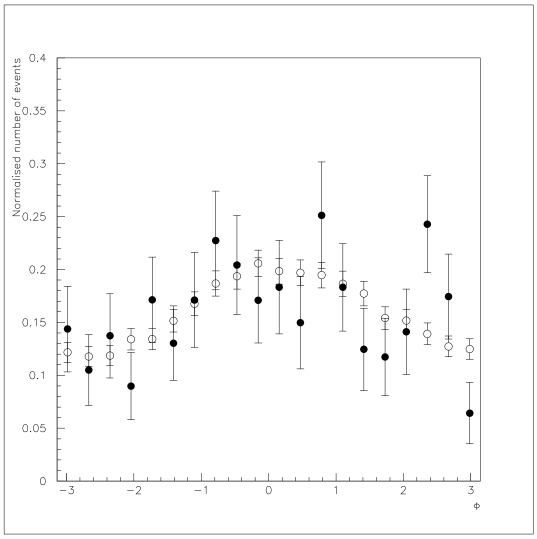

(c) Unpolarised 1997

(d) Polarised 1997

Figure D.11: Comparison of the experimental distributions in Φ to the optimised Monte Carlo model for bin Q3. Filled and empty circles represent the data and the optimised Monte Carlo model, respectively.

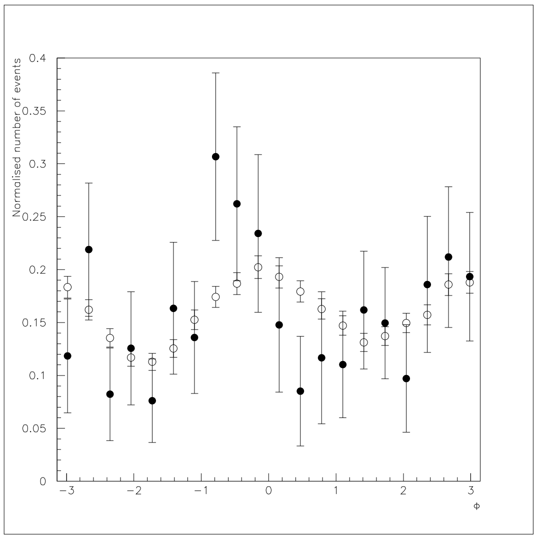

(a) Unpolarised 1996

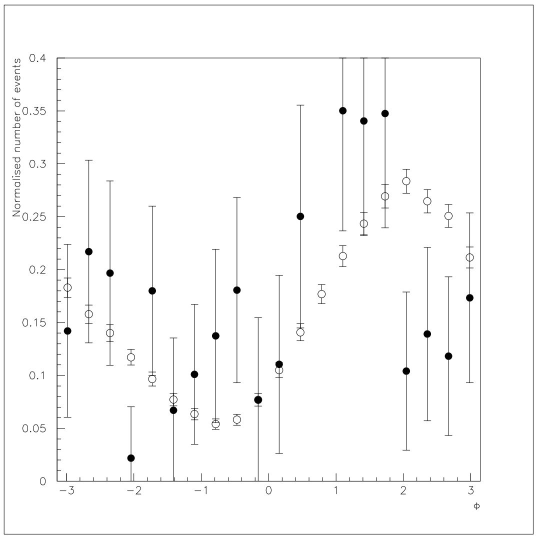

(b) Polarised 1996

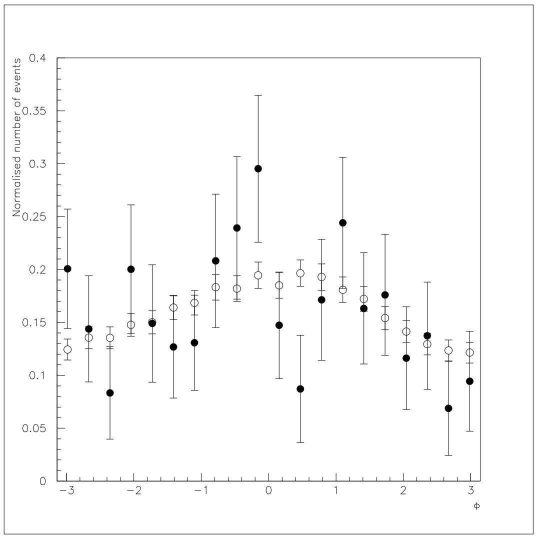

(c) Unpolarised 1997

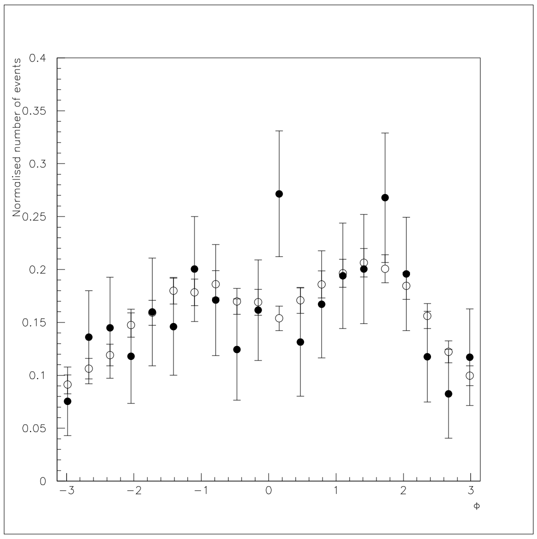

(d) Polarised 1997

Figure D.12: Comparison of the experimental distributions in Φ to the optimised Monte Carlo model for bin Q4. Filled and empty circles represent the data and the optimised Monte Carlo model, respectively.

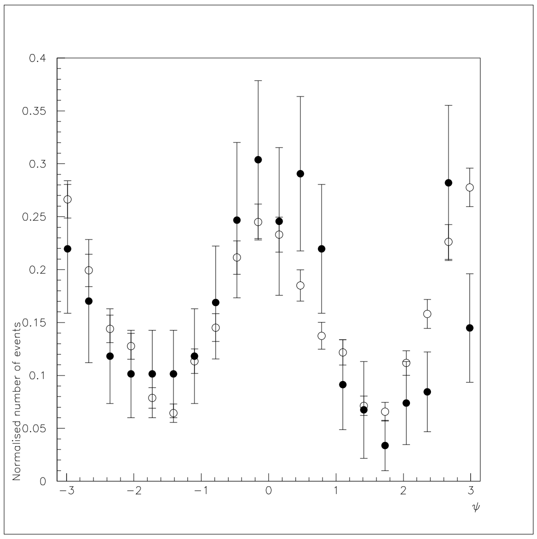

(a) Unpolarised 1996

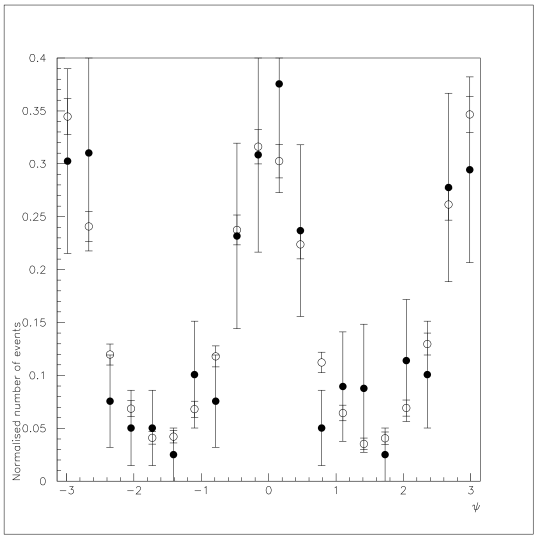

(b) Polarised 1996

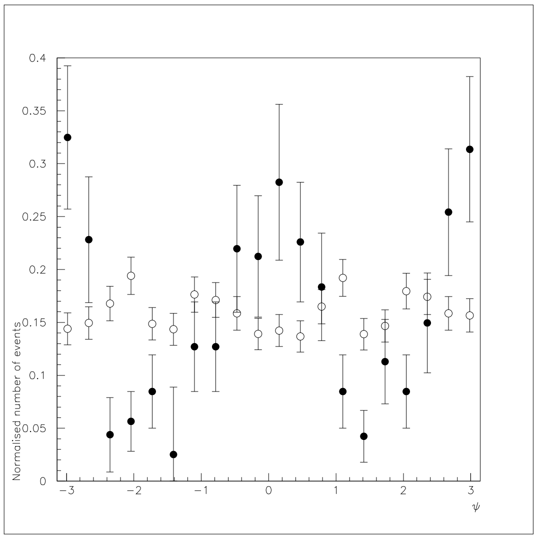

(c) Unpolarised 1997

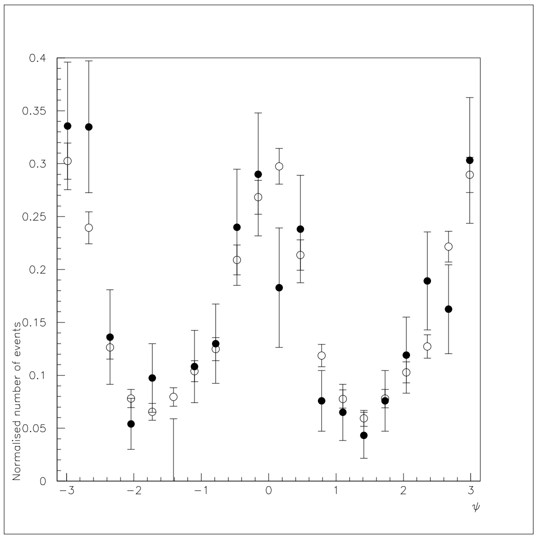

(d) Polarised 1997

Figure D.13: Comparison of the experimental distributions in ψ to the optimised Monte Carlo model for bin Q1. Filled and empty circles represent the data and the optimised Monte Carlo model, respectively.

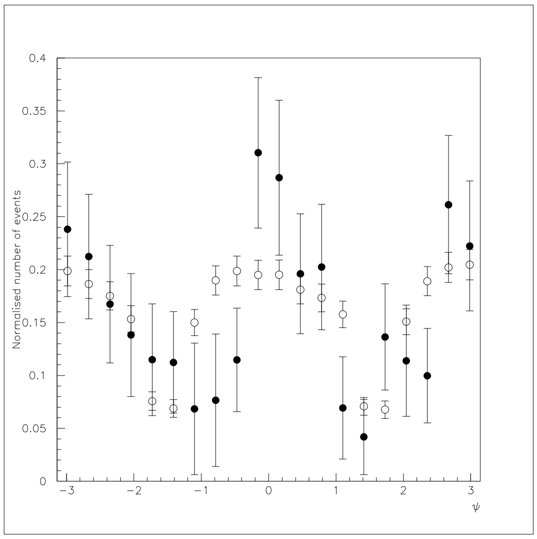

(a) Unpolarised 1996

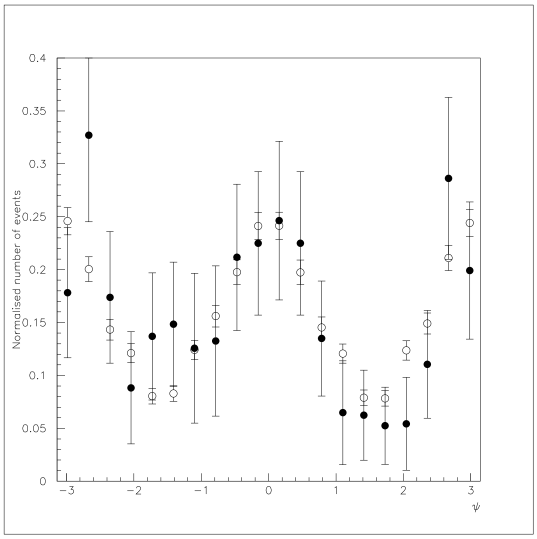

(b) Polarised 1996

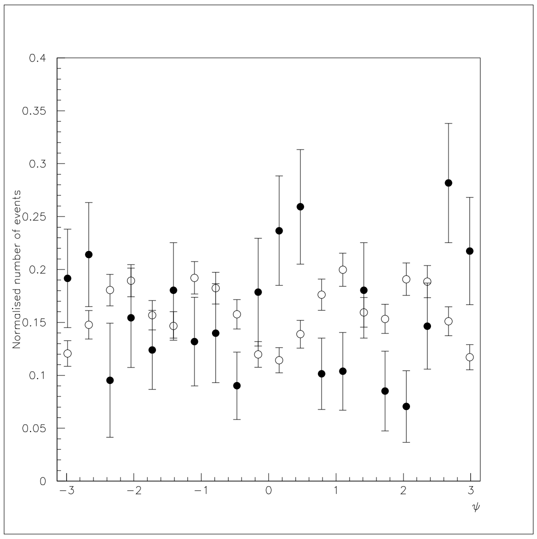

(c) Unpolarised 1997

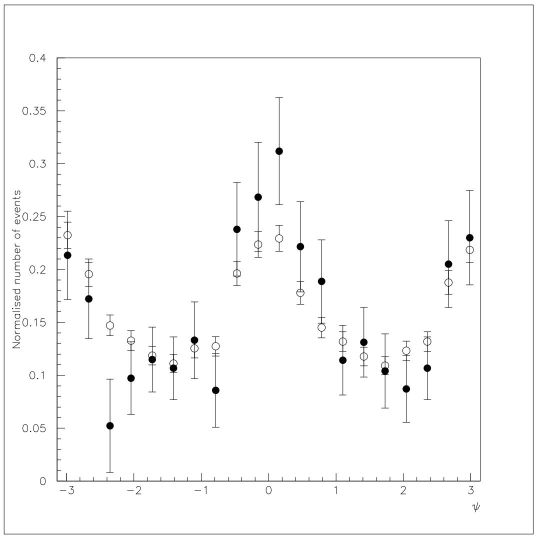

(d) Polarised 1997

Figure D.14: Comparison of the experimental distributions in ψ to the optimised Monte Carlo model for bin Q2. Filled and empty circles represent the data and the optimised Monte Carlo model, respectively.

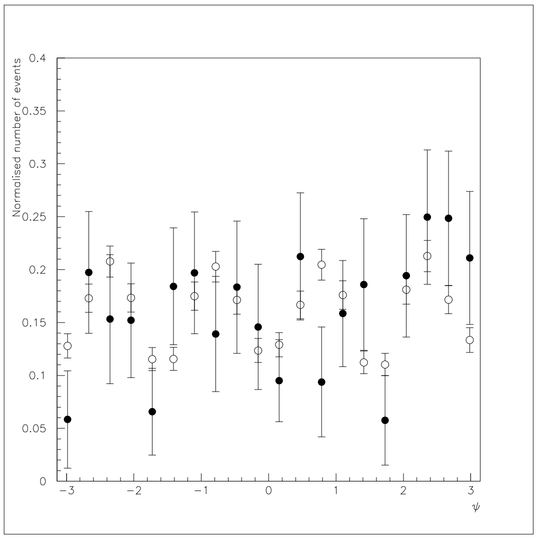

(a) Unpolarised 1996

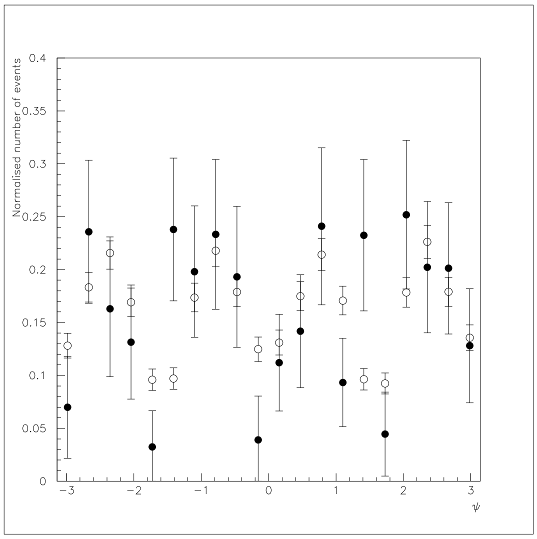

(b) Polarised 1996

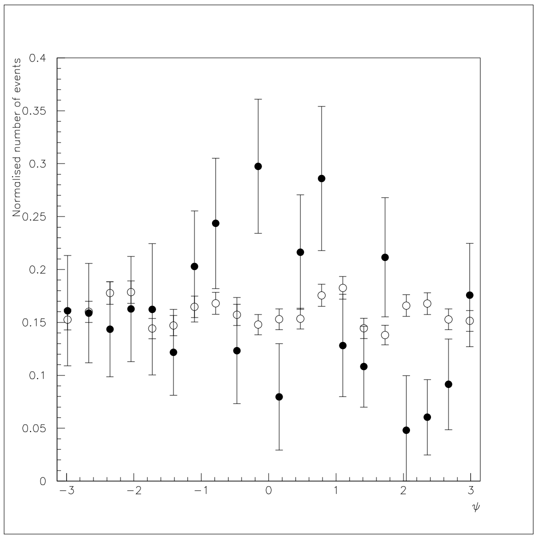

(c) Unpolarised 1997

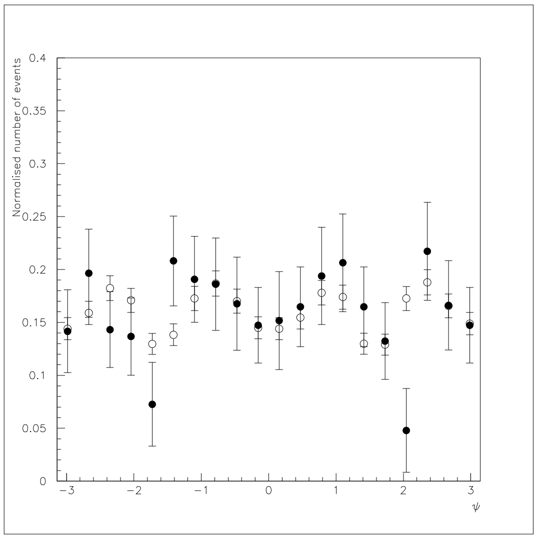

(d) Polarised 1997

Figure D.15: Comparison of the experimental distributions in ψ to the optimised Monte Carlo model for bin Q3. Filled and empty circles represent the data and the optimised Monte Carlo model, respectively.

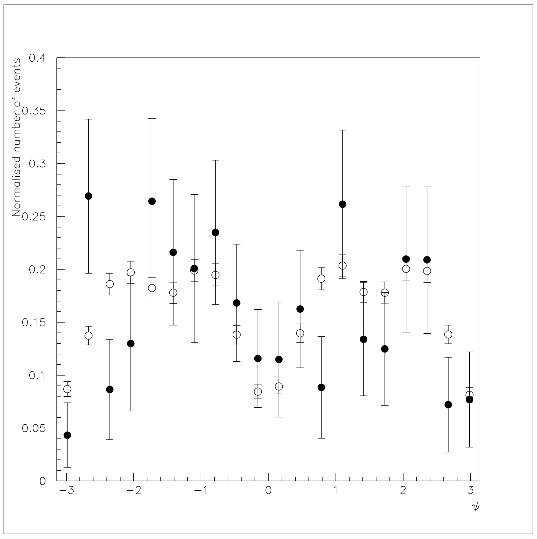

(a) Unpolarised 1996

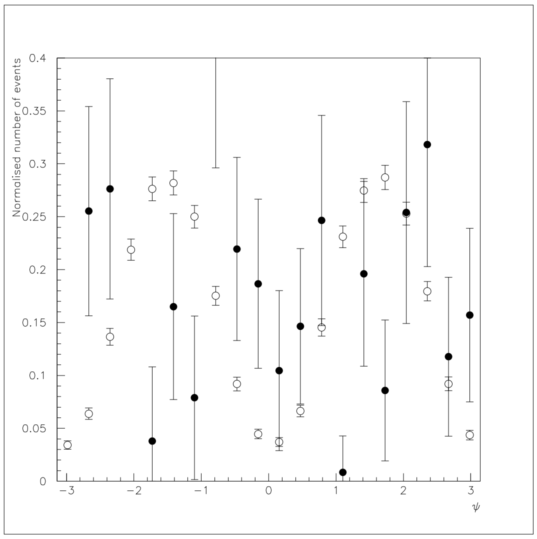

(b) Polarised 1996

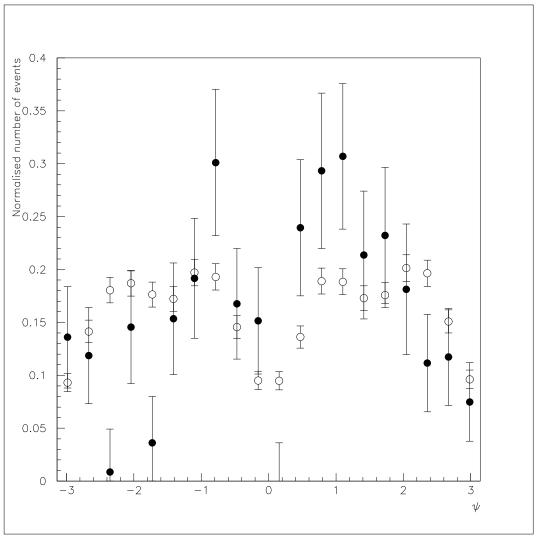

(c) Unpolarised 1997

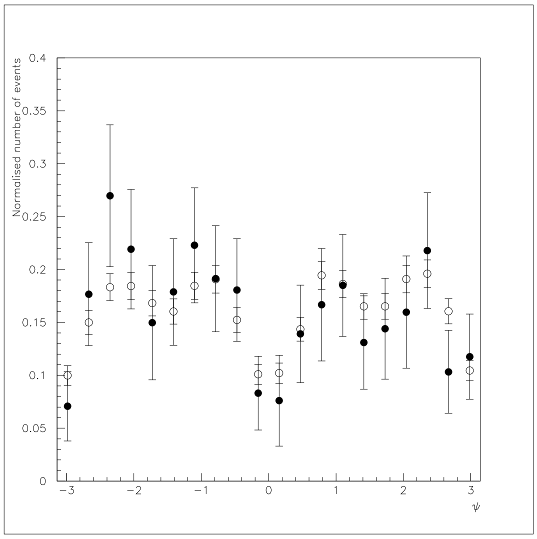

(d) Polarised 1997

Figure D.16: Comparison of the experimental distributions in ψ to the optimised Monte Carlo model for bin Q4. Filled and empty circles represent the data and the optimised Monte Carlo model, respectively.

Appendix E

Correlation Coefficients

A quantity Z calculated in terms of any two correlated parameters X and Y, with a correlation coefficient r_{XY}, has uncertainty computed according to [43]

$$\delta Z = \sqrt{\left(\frac{\partial Z}{\partial X}\delta X\right)^2 + \left(\frac{\partial Z}{\partial Y}\delta Y\right)^2 + 2r_{XY}\frac{\partial Z}{\partial X}\frac{\partial Z}{\partial Y}\delta X \delta Y}\ , \tag{E.1}$$

where δX and δY are uncertainties in X and Y, respectively. In performing the eight-parameter fit of the experimental diffractive ρ^0 angular distributions, MINUIT provides information about the correlation coefficients for any two pairs of matrix elements. Tables E.1 – E.16 contain the correlation coefficients for each case.

SDME	r^{04}_{00}	r^{04}_{1-1}	r^{1}_{1-1}	$\mathrm{Im}(r^{3}_{1-1})$	$\mathrm{Tr}(r^{1})$	$\mathrm{Tr}(r^{5})$	$\mathrm{Tr}(r^{8})$	δ
r^{04}_{00}	1.000	0.308	−0.729	0.169	−0.151	0.661	−0.095	0.491
r^{04}_{1-1}	0.308	1.000	−0.276	0.258	0.267	0.564	−0.079	0.534
r^{1}_{1-1}	−0.729	−0.276	1.000	−0.114	0.244	−0.852	0.045	−0.320
$\mathrm{Im}(r^{3}_{1-1})$	0.169	0.258	−0.114	1.000	0.125	0.228	−0.559	0.385
$\mathrm{Tr}(r^{1})$	−0.151	0.267	0.244	0.125	1.000	−0.173	−0.117	0.335
$\mathrm{Tr}(r^{5})$	0.661	0.564	−0.852	0.228	−0.173	1.000	−0.052	0.608
$\mathrm{Tr}(r^{8})$	−0.095	−0.079	0.045	−0.559	−0.117	−0.052	1.000	−0.113
δ	0.491	0.534	−0.320	0.385	0.335	0.608	−0.113	1.000

Table E.1: Correlation coefficients for the fit of the SDME to the unpolarised 1996 data, bin Q1

SDME	r^{04}_{00}	r^{04}_{1-1}	r^{1}_{1-1}	$\mathrm{Im}(r^{3}_{1-1})$	$\mathrm{Tr}(r^{1})$	$\mathrm{Tr}(r^{5})$	$\mathrm{Tr}(r^{8})$	δ
r^{04}_{00}	1.000	−0.164	−0.712	−0.017	−0.171	0.057	−0.023	−0.056
r^{04}_{1-1}	−0.164	1.000	−0.050	−0.088	0.567	0.345	0.051	−0.004
r^{1}_{1-1}	−0.712	−0.050	1.000	0.027	0.203	−0.499	0.010	0.002
$\mathrm{Im}(r^{3}_{1-1})$	−0.017	−0.088	0.027	1.000	−0.042	−0.024	−0.592	0.000
$\mathrm{Tr}(r^{1})$	−0.171	0.567	0.203	−0.042	1.000	−0.161	0.014	0.019
$\mathrm{Tr}(r^{5})$	0.057	0.345	−0.499	−0.024	−0.161	1.000	0.043	−0.074
$\mathrm{Tr}(r^{8})$	−0.023	0.051	0.010	−0.592	0.014	0.043	1.000	0.010
δ	−0.056	−0.004	0.002	0.000	0.019	−0.074	0.010	1.000

Table E.2: Correlation coefficients for the fit of the SDME to the unpolarised 1996 data, bin Q2

SDME	r^{04}_{00}	r^{04}_{1-1}	r^{1}_{1-1}	$\mathrm{Im}(r^{3}_{1-1})$	$\mathrm{Tr}(r^1)$	$\mathrm{Tr}(r^5)$	$\mathrm{Tr}(r^8)$	δ
r^{04}_{00}	1.000	−0.121	−0.563	0.027	−0.143	0.274	−0.010	0.423
r^{04}_{1-1}	−0.121	1.000	0.005	0.004	0.565	0.233	0.010	0.00
$6\ r^{1}_{1-1}$	−0.563	0.005	1.000	0.029	0.110	−0.194	0.027	0.233
$\mathrm{Im}(r^{3}_{1-1})$	0.027	0.004	0.029	1.000	0.025	0.044	−0.491	0.081
$\mathrm{Tr}(r^1)$	−0.143	0.565	0.110	0.025	1.000	−0.141	−0.038	−0.083
$\mathrm{Tr}(r^5)$	0.274	0.233	−0.194	0.044	−0.141	1.000	0.033	0.462
$\mathrm{Tr}(r^8)$	−0.010	0.010	0.027	−0.491	−0.038	0.033	1.000	0.017
δ	0.423	0.006	0.233	0.081	−0.083	0.462	0.017	1.000

Table E.3: Correlation coefficients for the fit of the SDME to the unpolarised 1996 data, bin Q3

SDME	r^{04}_{00}	r^{04}_{1-1}	r^{1}_{1-1}	$\mathrm{Im}(r^{3}_{1-1})$	$\mathrm{Tr}(r^1)$	$\mathrm{Tr}(r^5)$	$\mathrm{Tr}(r^8)$	δ
r^{04}_{00}	1.000	−0.036	−0.565	−0.009	−0.090	−0.044	−0.010	0.027
r^{04}_{1-1}	−0.036	1.000	0.064	0.016	0.554	0.211	0.019	0.012
r^{1}_{1-1}	−0.565	0.064	1.000	−0.054	0.152	−0.036	0.015	0.020
$\mathrm{Im}(r^{3}_{1-1})$	−0.009	0.016	−0.054	1.000	−0.022	0.021	−0.312	0.006
$\mathrm{Tr}(r^1)$	−0.090	0.554	0.152	−0.022	1.000	0.016	0.071	0.012
$\mathrm{Tr}(r^5)$	−0.044	0.211	−0.036	0.021	0.016	1.000	−0.109	0.029
$\mathrm{Tr}(r^8)$	−0.010	0.019	0.015	−0.312	0.071	−0.109	1.000	−0.028
δ	0.027	0.012	0.020	0.006	0.012	0.029	−0.028	1.000

Table E.4: Correlation coefficients for the fit of the SDME to the unpolarised 1996 data, bin Q4

SDME	r^{04}_{00}	r^{04}_{1-1}	r^{1}_{1-1}	$\mathrm{Im}(r^{3}_{1-1})$	$\mathrm{Tr}(r^1)$	$\mathrm{Tr}(r^5)$	$\mathrm{Tr}(r^8)$	δ
r^{04}_{00}	1.000	−0.039	−0.630	−0.004	−0.170	0.449	0.027	0.524
r^{04}_{1-1}	−0.039	1.000	−0.142	0.000	0.320	0.260	0.009	−0.079
r^{1}_{1-1}	−0.630	−0.142	1.000	−0.063	0.264	−0.880	0.019	−0.349
$\mathrm{Im}(r^{3}_{1-1})$	−0.004	0.000	−0.063	1.000	−0.049	0.052	−0.672	−0.027
$\mathrm{Tr}(r^1)$	−0.170	0.320	0.264	−0.049	1.000	−0.256	0.117	0.171
$\mathrm{Tr}(r^5)$	0.449	0.260	−0.880	0.052	−0.256	1.000	0.015	0.473
$\mathrm{Tr}(r^8)$	0.027	0.009	0.019	−0.672	0.117	0.015	1.000	0.119
δ	0.524	−0.079	−0.349	−0.027	0.171	0.473	0.119	1.000

Table E.5: Correlation coefficients for the fit of the SDME to the polarised 1996 data, bin Q1

SDME	r^{04}_{00}	r^{04}_{1-1}	r^{1}_{1-1}	$\mathrm{Im}(r^{3}_{1-1})$	$\mathrm{Tr}(r^1)$	$\mathrm{Tr}(r^5)$	$\mathrm{Tr}(r^8)$	δ
r^{04}_{00}	1.000	−0.115	−0.763	0.014	−0.180	0.157	0.021	−0.015
r^{04}_{1-1}	−0.115	1.000	−0.131	−0.084	0.535	0.356	0.069	0.028
r^{1}_{1-1}	−0.763	−0.131	1.000	−0.004	0.177	−0.533	−0.037	−0.006
$\mathrm{Im}(r^{3}_{1-1})$	0.014	−0.084	−0.004	1.000	−0.090	−0.014	−0.550	−0.005
$\mathrm{Tr}(r^1)$	−0.180	0.535	0.177	−0.090	1.000	−0.138	0.107	0.022
$\mathrm{Tr}(r^5)$	0.157	0.356	−0.533	−0.014	−0.138	1.000	0.061	−0.057
$\mathrm{Tr}(r^8)$	0.021	0.069	−0.037	−0.550	0.107	0.061	1.000	0.033
δ	−0.015	0.028	−0.006	−0.005	0.022	−0.057	0.033	1.000

Table E.6: Correlation coefficients for the fit of the SDME to the polarised 1996 data, bin Q2

SDME	r^{04}_{00}	r^{04}_{1-1}	r^{1}_{1-1}	$\mathrm{Im}(r^{3}_{1-1})$	$\mathrm{Tr}(r^1)$	$\mathrm{Tr}(r^5)$	$\mathrm{Tr}(r^8)$	δ
r^{04}_{00}	1.000	−0.282	−0.558	−0.158	−0.184	0.304	−0.041	0.472
r^{04}_{1-1}	−0.282	1.000	−0.122	0.038	0.608	0.002	0.100	−0.398
r^{1}_{1-1}	−0.558	−0.122	1.000	−0.131	0.043	−0.184	−0.024	0.155
$\mathrm{Im}(r^{3}_{1-1})$	−0.158	0.038	−0.131	1.000	0.043	−0.224	−0.392	−0.397
$\mathrm{Tr}(r^1)$	−0.184	0.608	0.043	0.043	1.000	−0.178	0.116	−0.245
$\mathrm{Tr}(r^5)$	0.304	0.002	−0.184	−0.224	−0.178	1.000	−0.114	0.541
$\mathrm{Tr}(r^8)$	−0.041	0.100	−0.024	−0.392	0.116	−0.114	1.000	−0.106
δ	0.472	−0.398	0.155	−0.397	−0.245	0.541	−0.106	1.000

Table E.7: Correlation coefficients for the fit of the SDME to the polarised 1996 data, bin Q3

SDME	r^{04}_{00}	r^{04}_{1-1}	r^{1}_{1-1}	$\mathrm{Im}(r^{3}_{1-1})$	$\mathrm{Tr}(r^1)$	$\mathrm{Tr}(r^5)$	$\mathrm{Tr}(r^8)$	δ
r^{04}_{00}	1.000	−0.155	−0.295	0.039	−0.042	−0.231	0.024	0.141
r^{04}_{1-1}	−0.155	1.000	−0.013	−0.032	0.583	0.235	0.074	−0.101
r^{1}_{1-1}	−0.295	−0.013	1.000	−0.035	0.028	0.145	−0.028	0.341
$\mathrm{Im}(r^{3}_{1-1})$	0.039	−0.032	−0.035	1.000	−0.044	0.012	−0.265	0.078
$\mathrm{Tr}(r^1)$	−0.042	0.583	0.028	−0.044	1.000	0.046	0.231	−0.094
$\mathrm{Tr}(r^5)$	−0.231	0.235	0.145	0.012	0.046	1.000	−0.104	0.198
$\mathrm{Tr}(r^8)$	0.024	0.074	−0.028	−0.265	0.231	−0.104	1.000	−0.203
δ	0.141	−0.101	0.341	0.078	−0.094	0.198	−0.203	1.000

Table E.8: Correlation coefficients for the fit of the SDME to the polarised 1996 data, bin Q4

SDME	r^{04}_{00}	r^{04}_{1-1}	r^{1}_{1-1}	$\mathrm{Im}(r^{3}_{1-1})$	$\mathrm{Tr}(r^1)$	$\mathrm{Tr}(r^5)$	$\mathrm{Tr}(r^8)$	δ
r^{04}_{00}	1.000	0.136	−0.735	−0.174	−0.281	0.514	0.127	0.368
r^{04}_{1-1}	0.136	1.000	−0.248	−0.210	0.212	0.455	0.116	0.253
r^{1}_{1-1}	−0.735	−0.248	1.000	0.122	0.364	−0.770	−0.078	−0.249
$\mathrm{Im}(r^{3}_{1-1})$	−0.174	−0.210	0.122	1.000	0.035	−0.394	−0.706	−0.559
$\mathrm{Tr}(r^1)$	−0.281	0.212	0.364	0.035	1.000	−0.395	−0.070	−0.071
$\mathrm{Tr}(r^5)$	0.514	0.455	−0.770	−0.394	−0.395	1.000	0.273	0.639
$\mathrm{Tr}(r^8)$	0.127	0.116	−0.078	−0.706	−0.070	0.273	1.000	0.392
δ	0.368	0.253	−0.249	−0.559	−0.071	0.639	0.392	1.000

Table E.9: Correlation coefficients for the fit of the SDME to the unpolarised 1997 data, bin Q1

SDME	r^{04}_{00}	r^{04}_{1-1}	r^{1}_{1-1}	$\mathrm{Im}(r^{3}_{1-1})$	$\mathrm{Tr}(r^1)$	$\mathrm{Tr}(r^5)$	$\mathrm{Tr}(r^8)$	δ
r^{04}_{00}	1.000	−0.051	−0.602	0.033	−0.194	0.247	0.013	0.164
r^{04}_{1-1}	−0.051	1.000	0.086	0.151	0.567	0.450	−0.076	0.303
r^{1}_{1-1}	−0.602	0.086	1.000	0.271	0.326	−0.078	−0.174	0.472
$\mathrm{Im}(r^{3}_{1-1})$	0.033	0.151	0.271	1.000	0.102	0.262	−0.604	0.440
$\mathrm{Tr}(r^1)$	−0.194	0.567	0.326	0.102	1.000	0.002	−0.047	0.215
$\mathrm{Tr}(r^5)$	0.247	0.450	−0.078	0.262	0.002	1.000	−0.122	0.619
$\mathrm{Tr}(r^8)$	0.013	−0.076	−0.174	−0.604	−0.047	−0.122	1.000	−0.236
δ	0.164	0.303	0.472	0.440	0.215	0.619	−0.236	1.000

Table E.10: Correlation coefficients for the fit of the SDME to the unpolarised 1997 data, bin Q2

SDME	r^{04}_{00}	r^{04}_{1-1}	r^{1}_{1-1}	$\mathrm{Im}(r^{3}_{1-1})$	$\mathrm{Tr}(r^{1})$	$\mathrm{Tr}(r^{5})$	$\mathrm{Tr}(r^{8})$	δ
r^{04}_{00}	1.000	−0.079	−0.708	0.021	−0.153	0.054	0.009	0.048
r^{04}_{1-1}	−0.079	1.000	0.011	−0.007	0.564	0.269	−0.013	0.054
r^{1}_{1-1}	−0.708	0.011	1.000	0.005	0.195	−0.266	−0.027	0.079
$\mathrm{Im}(r^{3}_{1-1})$	0.021	−0.007	0.005	1.000	−0.030	−0.004	−0.418	0.042
$\mathrm{Tr}(r^{1})$	−0.153	0.564	0.195	−0.030	1.000	−0.121	0.009	0.023
$\mathrm{Tr}(r^{5})$	0.054	0.269	−0.266	−0.004	−0.121	1.000	−0.025	0.111
$\mathrm{Tr}(r^{8})$	0.009	−0.013	−0.027	−0.418	0.009	−0.025	1.000	−0.025
δ	0.048	0.054	0.079	0.042	0.023	0.111	−0.025	1.000

Table E.11: Correlation coefficients for the fit of the SDME to the unpolarised 1997 data, bin Q3

SDME	r^{04}_{00}	r^{04}_{1-1}	r^{1}_{1-1}	$\mathrm{Im}(r^{3}_{1-1})$	$\mathrm{Tr}(r^{1})$	$\mathrm{Tr}(r^{5})$	$\mathrm{Tr}(r^{8})$	δ
r^{04}_{00}	1.000	0.017	−0.220	−0.037	−0.097	0.192	−0.010	−0.565
r^{04}_{1-1}	0.017	1.000	0.101	−0.036	0.523	0.197	0.007	−0.131
r^{1}_{1-1}	−0.220	0.101	1.000	−0.059	−0.008	0.067	0.012	−0.412
$\mathrm{Im}(r^{3}_{1-1})$	−0.037	−0.036	−0.059	1.000	0.026	−0.047	−0.302	0.085
$\mathrm{Tr}(r^{1})$	−0.097	0.523	−0.008	0.026	1.000	−0.104	−0.034	0.123
$\mathrm{Tr}(r^{5})$	0.192	0.197	0.067	−0.047	−0.104	1.000	−0.009	−0.359
$\mathrm{Tr}(r^{8})$	−0.010	0.007	0.012	−0.302	−0.034	−0.009	1.000	0.007
δ	−0.565	−0.131	−0.412	0.085	0.123	−0.359	0.007	1.000

Table E.12: Correlation coefficients for the fit of the SDME to the unpolarised 1997 data, bin Q4

SDME	r^{04}_{00}	r^{04}_{1-1}	r^{1}_{1-1}	$\mathrm{Im}(r^{3}_{1-1})$	$\mathrm{Tr}(r^{1})$	$\mathrm{Tr}(r^{5})$	$\mathrm{Tr}(r^{8})$	δ
r^{04}_{00}	1.000	0.156	−0.699	−0.093	−0.247	0.536	0.058	0.378
r^{04}_{1-1}	0.156	1.000	−0.211	−0.085	0.279	0.502	0.037	0.391
r^{1}_{1-1}	−0.699	−0.211	1.000	0.039	0.369	−0.771	−0.024	−0.135
$\mathrm{Im}(r^{3}_{1-1})$	−0.093	−0.085	0.039	1.000	−0.022	−0.174	−0.661	−0.255
$\mathrm{Tr}(r^{1})$	−0.247	0.279	0.369	−0.022	1.000	−0.340	−0.017	0.094
$\mathrm{Tr}(r^{5})$	0.536	0.502	−0.771	−0.174	−0.340	1.000	0.092	0.552
$\mathrm{Tr}(r^{8})$	0.058	0.037	−0.024	−0.661	−0.017	0.092	1.000	0.115
δ	0.378	0.391	−0.135	−0.255	0.094	0.552	0.115	1.000

Table E.13: Correlation coefficients for the fit of the SDME to the polarised 1997 data, bin Q1

SDME	r^{04}_{00}	r^{04}_{1-1}	r^{1}_{1-1}	$\mathrm{Im}(r^{3}_{1-1})$	$\mathrm{Tr}(r^{1})$	$\mathrm{Tr}(r^{5})$	$\mathrm{Tr}(r^{8})$	δ
r^{04}_{00}	1.000	−0.121	−0.750	−0.001	−0.267	0.157	0.044	−0.010
r^{04}_{1-1}	−0.121	1.000	−0.061	−0.002	0.549	0.347	−0.003	−0.017
r^{1}_{1-1}	−0.750	−0.061	1.000	0.005	0.304	−0.551	−0.033	−0.014
$\mathrm{Im}(r^{3}_{1-1})$	−0.001	−0.002	0.005	1.000	−0.033	0.027	−0.582	−0.009
$\mathrm{Tr}(r^{1})$	−0.267	0.549	0.304	−0.033	1.000	−0.200	0.091	−0.011
$\mathrm{Tr}(r^{5})$	0.157	0.347	−0.551	0.027	−0.200	1.000	−0.055	−0.022
$\mathrm{Tr}(r^{8})$	0.044	−0.003	−0.033	−0.582	0.091	−0.055	1.000	0.029
δ	−0.010	−0.017	−0.014	−0.009	−0.011	−0.022	0.029	1.000

Table E.14: Correlation coefficients for the fit of the SDME to the polarised 1997 data, bin Q2

SDME	r_{00}^{04}	r_{1-1}^{04}	r_{1-1}^{1}	$\mathrm{Im}(r_{1-1}^{3})$	$\mathrm{Tr}(r^1)$	$\mathrm{Tr}(r^5)$	$\mathrm{Tr}(r^8)$	δ
r_{00}^{04}	1.000	−0.041	−0.250	−0.040	−0.155	0.382	0.069	−0.569
r_{1-1}^{04}	−0.041	1.000	0.052	0.049	0.547	0.249	−0.011	−0.092
r_{1-1}^{1}	−0.250	0.052	1.000	−0.050	0.054	0.009	0.068	−0.486
$\mathrm{Im}(r_{1-1}^{3})$	−0.040	0.049	−0.050	1.000	0.021	−0.035	−0.468	0.077
$\mathrm{Tr}(r^1)$	−0.155	0.547	0.054	0.021	1.000	−0.207	−0.057	0.126
$\mathrm{Tr}(r^5)$	0.382	0.249	0.009	−0.035	−0.207	1.000	0.101	−0.548
$\mathrm{Tr}(r^8)$	0.069	−0.011	0.068	−0.468	−0.057	0.101	1.000	−0.131
δ	−0.569	−0.092	−0.486	0.077	0.126	−0.548	−0.131	1.000

Table E.15: Correlation coefficients for the fit of the SDME to the polarised 1997 data, bin Q3

SDME	r_{00}^{04}	r_{1-1}^{04}	r_{1-1}^{1}	$\mathrm{Im}(r_{1-1}^{3})$	$\mathrm{Tr}(r^1)$	$\mathrm{Tr}(r^5)$	$\mathrm{Tr}(r^8)$	δ
r_{00}^{04}	1.000	−0.081	−0.636	−0.010	0.018	−0.025	−0.021	0.010
r_{1-1}^{04}	−0.081	1.000	0.051	0.023	0.523	0.142	0.006	−0.013
r_{1-1}^{1}	−0.636	0.051	1.000	0.043	−0.022	−0.088	0.039	−0.004
$\mathrm{Im}(r_{1-1}^{3})$	−0.010	0.023	0.043	1.000	0.001	0.015	−0.297	−0.021
$\mathrm{Tr}(r^1)$	0.018	0.523	−0.022	0.001	1.000	−0.144	−0.022	0.008
$\mathrm{Tr}(r^5)$	−0.025	0.142	−0.088	0.015	−0.144	1.000	0.011	0.016
$\mathrm{Tr}(r^8)$	−0.021	0.006	0.039	−0.297	−0.022	0.011	1.000	0.031
δ	0.010	−0.013	−0.004	−0.021	0.008	0.016	0.031	1.000

Table E.16: Correlation coefficients for the fit of the SDME to the polarised 1997 data, bin Q4

Bibliography

[1] S.L. Glashow, *Partial Symmetries of Weak Interactions*. Nucl. Phys. **22**: 579 (1961)

[2] S. Weinberg, *A Model of Leptons*. Phys. Rev. Lett. **19**: 1264 (1967)

[3] A. Salam, in *Elementary Particle Theory*, N. Svartholm, ed. Almquist and Wiksell (1968)

[4] T.H.Bauer, R.D.Spital, and D. R. Yennie, *The hadronic properties of the photon in high-energy interactions*. Rev. Mod. Phys. **50**: 261-436 (1978)

[5] G.F. Chew, S.C. Frautschi, *Principle of Equivalence for All Strongly Interacting Particles Within the S Matrix Framework*. Phys. Rev. Letters, **7**: 394 (1961)

[6] A. Donnachie, P.V. Landshoff, *Total Cross Sections*. Phys. Lett. **B296**: 227-232 (1992)

[7] P.D.B. Collins, *An introduction to Regge theory and high energy physics*. Cambridge University Press (1977)

[8] M. Vanderhaeghen, P.A.M. Guichon and M. Guidal, Hard Electroproduction of Photons and Mesons on the Nucleon. Phys. Rev. Lett. **80**: 5064 (1998)

[9] K. Schilling, G. Wolf, *How to Analyse Vector-Meson Production in Inelastic Lepton Scattering.* Nucl. Phys.. **B61**: 381-413 (1973)

[10] M. Kolstein, *Exclusive ρ^0 Meson Leptoproduction at HERMES.* PhD thesis, Vrije Universiteit Amsterdam (1998)

[11] E. Belz, *Rho Polarization in Exclusive* $\mathrm{A}(\mathrm{e}, \mathrm{e}', \rho^0)$. HERMES internal note 96-052

[12] K. Schilling, P. Seyboth, G. Wolf, *On the Analysis of Vector-Meson Production by Polarized Photons.* Nucl. Phys. **B15**: 397-412 (1970)

[13] W. Lorenzon, *Beam Polarimetry at HERA.* 7th International Workshop on Polarized Gas Targets and Polarized Beams, Urbana-Champaign (1997)

[14] U. Stösslein, *Measurement of the Polarized Neutron Structure Function g_1^n at HERA.* 5th International Workshop on Deep Inelastic Scattering and QCD (DIS 97), Chicago, USA (1997)

[15] D.P. Barber *et al.*, *The First Achievement of Longitudinal Spin Polarization in a High Energy Electron Storage Ring.* Phys. Lett. **B 343**: 436-443 (1995)

[16] B.S. Bains, *A Measurement of Nucleon Quark Spin Distributions at HERMES.* PhD thesis, University of Illinois at Urbana-Champaign (2000)

[17] B.H. Bransden and C.J. Joachain, *Quantum Mechanics.* Longman Scientific & Technical (1989)

[18] D. Reggiani, *Studio ed applicazione di un bersaglio transversalmente polarizzato per l'esperimento HERMES a HERA.* Diploma thesis, Università degli Studi di Ferrara (1999)

[19] M. Beckmann *et al.*, *The Longitudinal Polarimeter at HERA.* Submitted to Nucl. Instrum. Meth. **A** (2000)

[20] A.V. Antipov *et al.*, *Investigation of New Inorganic Materials for Homogeneous Electromagnetic Calorimeters.* Nucl. Instrum. Meth. **A 327**: 346-353 (1993)

[21] D.P. Barber *et al.*, *The HERA Polarimeter and the First Observation of Electron Spin Polarization at HERA.* Nucl. Instrum. Meth. **A 329**: 79-111 (1993)

[22] H. Kolster, *Beam-Induced Resonant Depolarization Effects in a Polarized Atomic Hydrogen Gas Target at HERA.* 7th International Workshop on Polarized Gas Targets and Polarized Beams, Urbana-Champaign (1997)

[23] C. Baumgarten, *Studies of Spin Relaxation and Recombination at the HERMES Hydrogen/Deuterium Gas Target.* PhD thesis, Ludwig-Maximilians Universität München (2000)

[24] W.R. Leo, *Techniques for Nuclear and Particle Physics Experiments*, 2nd ed. Springer-Verlag (1994)

[25] The HERMES Collaboration. *Technical Design Report.* (1993)

[26] D. De Schepper *et al.*, *The HERMES Cerenkov Detector.* HERMES internal note 00-021

[27] R. Kaiser, *Particle Identification at HERMES.* HERMES internal note 97-025

[28] X. Artru, G.B. Yodh, and G. Mennessier, *Practical Theory of the Multi-Layered Transition Radiation Detector.* Phys. Rev. **D 12**: 1289 (1975)

[29] A. Fantoni, *Construzione del calorimetro a contatori di vetro al piombo dell'esperimento HERMES per la misura delle funzioni di struttura di spin dei nucleoni.* PhD thesis. Università degli Studi della Calabria (1996)

[30] J. Wendland, *Improved Particle Identification at HERMES and Polarised Valence Quark Distributions in the Proton.* MSc thesis. Simon Fraser University (1999)

[31] T. Benisch, *Polarisierte Bhabha-Streuung und Luminositätsmessung im HERMES-Experiment.* PhD thesis. Friedrich-Alexander-Universität Erlangen-Nürnberg (1998)

[32] F.K. Martens, *Elastic Production and Decay of Rho Mesons at HERMES.* MSc thesis. University of Alberta (1998)

[33] H. Gould, J. Tobochnik, *An Introduction to Computer Simulation Methods.* Addison-Wesley. **2nd ed.**: 190 (1996)

[34] *GEANT: Detector Description and Simulation Tool.* CERN Program Library. Available at http://consult.cern.ch/writeup/geant/

[35] M. Maul *et al.*, *PEPSI 4.21, a Monte Carlo Generator for polarised leptoproduction.* DESY. Available at http://hermes.desy.de/~ihssen/pepsi.html

[36] G. Ingelman, A. Edin, J. Rathsman, *LEPTO 6.5 — A Monte Carlo Generator for Deep Inelastic Lepton-Nucleon Scattering.* DESY Note 96-057

[37] B. Andersson *et al.*, *Parton Fragmentation and String Dynamics.* Phys.Rept. **97**: 31 (1983)

[38] J.D. Jackson, *Remarks on the Phenomenological Analysis of Resonances* Nuovo Cim. **34**: 1644 (1964)

[39] W.D. Shambroom *et al.*, *Diffractive production of vector mesons in muon-proton scattering.* Phys. Rev. **D 26**: 1-22 (1982)

[40] M. Tytgat, *Studies of the ρ^0 and ω Invariant Mass Distributions.* HERMES internal note 00-019

[41] F. James, *MUNUIT: Function Minimization and Error Analysis. Reference Manual.* CERN Program Library Long Writeup D506. Available at http://consult.cern.ch/writeup/minuit/

[42] HERMES Collab., K. Ackerstaff *et al.*, *Measurement of Angular Distribution and $R = \frac{\sigma_L}{\sigma_T}$ in Diffractive Electroproduction of ρ^0 Mesons.* Eur. Phys. J. **C** (2000)

[43] J. R. Taylor, *An Introduction to Error Analysis.* University Science Books (1982)

[44] P. Joos *et al.*, *Rho Production by Virtual Photons.* Nucl. Phys. **B113**: 53 (1976)

[45] EMC Collab., J.J. Aubert *et al.*, *Exclusive ρ^0 Production in Deep Inelastic Muon Proton Scattering.* Phys. Lett. **B161**: 203 (1985)

[46] NMC Collab., M. Arneodo *et al.*, *Exclusive ρ^0 and ϕ Muoproduction at Large Q^2.* Nucl. Phys. **B429**: 503 (1994)

[47] E665 Collab., M.R. Adams *et al.*, *Diffractive production of ρ^0 (770) mesons in muon-proton interactions at 470 GeV.* Z. Phys. **C74**: 237 (1997)

[48] ZEUS Collab., M. Derrick *et al.*, *Exclusive ρ^0 production in deep inelastic electron-proton scattering at HERA.* Z. Phys. **C69**: 39 (1995)

[49] ZEUS Collab., M. Derrick *et al.*, *Measurement of Elastic ρ^0 Photoproduction at HERA.* Phys. Lett. **B356**: 601 (1995)

[50] ZEUS Collab., J. Breitweg *et al.*, *Measurement of the Spin-Density Matrix Elements in Exclusive Electroproduction of ρ^0 Mesons at HERA.* Eur. Phys. J. **C12**: 393 (2000)

[51] H1 Collab., S. Aid *et al.*, *Elastic Electroproduction of* ρ^0 *and* J/ψ *Mesons at Large* Q^2 *at HERA*. Nucl. Phys. **C468**: 3 (1996)

[52] T.G. O'Neill, *Observation of a Coherence Length Effect in Exclusive* ρ^0 *Electroproduction*. th International Conference on the Structure of Baryons (BARYONS 98), Bonn, Germany, (1998)

[53] D.G. Cassel *et al.*, *Exclusive* ρ^0 *,* ω *and* Φ^0 *electroproduction*. Phys. Rev. **D24**: 2787 (1981)